ENERGY-INFORMED STRATEGIES FOR LOW-THRUST TRAJECTORY DESIGN IN CISLUNAR SPACE

by

Bonnie Jessenia Prado Pino

A Dissertation

Submitted to the Faculty of Purdue University

In Partial Fulfillment of the Requirements for the degree of

Doctor of Philosophy

Aeronautics and Astronautics

West Lafayette, Indiana

December 2020

THE PURDUE UNIVERSITY GRADUATE SCHOOL
STATEMENT OF COMMITTEE APPROVAL

Dr. Kathleen C. Howell, Chair

School of Aeronautics and Astronautics

Dr. James Longuski

School of Aeronautics and Astronautics

Dr. Inseok Hwang

School of Aeronautics and Astronautics

Dr. Belinda Marchand

Progalaxia LLC, Austin TX

Approved by:

Dr. Gregory Blaisdell

Para Don Ramiro, la tia Mary, Oscar y Gloria.

ACKNOWLEDGMENTS

First, I would like to thank God for all the blessings he continues to grant upon me. Every new day is a new opportunity to continue dreaming and to continue thriving to reach my best potential and achieve my goals. Some of those goals I have had since I was a just a little girl growing up in one of the most rural areas of Colombia, my hometown Chocó. My fascination for space started early on in my life, and little did I know that I would end up becoming an aerospace engineer, and, that I would be contributing to the international space field as an astrodynamicist. Only to God be the glory.

To my family, both immediate and extended, I have no words to express how blessed I am to have you in my life. Mom, dad, Gloria and Oscar, you guys are the pillar of my life, and everything I have ever accomplished would had never been possible without your support. Support that has lifted me when I fell into my lowest emotional points, support that has laughed with me in the good moments, and in the bad ones too. Your support has guide me through life as I admire every single one of you. You are the kindest and smartest of all people, and everyone around you is nothing but lucky to have you.

Professor Howell, you have been much more than a mentor and an advisor to me, it is impossible not to cry when typing these words, as you took me into your research group without me really knowing much about astrodynamics, and turned me into a very capable and competent researcher, ready to face the challenges of real-life mission design and all aspects of trajectory design. Words are not enough to express my gratitude for your support throughout these years at Purdue. You have not only supported me academically, but have been there for me every step of the way holding my back every time a new challenged deviated me from my path. You have gone far out of your way to be there for me every single time I needed you, and I want you to know that I will never forget what you have done for me. I will forever be grateful to you.

Dr. Marchand, you also hold a very special place in my heart. I learned a lot from being your student during my time as a Master student at the University of Texas at Austin; and you are the reason why I came to pursue my PhD at Purdue University in the first place.

You have trusted that I would one day be a doctor in aerospace engineering, and here I am, very close to accomplishing that dream. Thank you very much.

I have had many mentors throughout my academic career, people from whom I have learned most of the things that I know about aerospace engineering. I would like to give special thanks to Professor Longuski and Professor Hwang for being part of my committee and at the same time, making sure that I stay true to my goals. A very special thank you goes to Dr. Cesar Ocampo as well, as you have not only advised me during my time in Austin, but have been there for me ever since. Mr. Dan Dumbacher and Dr. Darryl Dickerson, thank you for always believing in me, and helping me grow professionally, by offering me opportunities outside of academia that helped me developed stronger leadership and organizational skills.

To the Minority Engineering Program (MEP) family. You have literally provided a home away from home for me. Your support not only financial but emotional has been crucial in the accomplishment of my PhD goals, and I am sure that the path would have been much more rougher had I not gotten involved with your office. Special thanks to Mr. and Mrs. Womack, Mrs. Mary Kenner, Mr. Derrick Williams and Dr. Carol Stwalley. I truly appreciate your friendship, and I have enjoyed very much working with you in so many projects to increase the STEM representation for minority groups in the United States.

Guillermo Caballero, you have been more than just a friend to me, you are my family. I thank God for bringing you into my life, and I only hope that I can somehow repay you for everything that you have done for me. You truly have a blessed heart, and I wish nothing but the best in all of your endeavours. Of course, I will be there for you anytime, anyplace.

Jhony Torrens, you came into my life when I needed you the most. You have brought nothing but joy and happiness to my life, and I thank God for making sure that our paths crossed. I would also like to thank all the members of the Purdue Multibody Dynamics research group, both current and past. I have learned a great deal from all of you. Listening to your research presentations have made me smarter, and more equipped to continue my professional path. Thank you for all the feedback that you offered, and thank you for being friends more than just colleagues. Very special thanks to Vivek, Rohan, Lucia, Maskai, Davide, Robert, Chris, Emily, Ted, Kenza and David for the countless time you have been there for me.

Last, but not least, I would like to thank all of my friends that have undoubtedly become my extended family here in the United States, Zrinka Puljiz, Sahil Jain, Ana Guerrero, Hector Escobar, Jorge Alvarez, Natalia Gomez, Sonia Hernandez, Ricardo Restrepo, Michele Saad, Cinnamon and Jimmy Wright, Divya Thakur and many more. Your friendship and support has held me through all of these years of very hard work. Thank you for being there for me. The list is long, as I have met many wonderful people during my time as a graduate student in the United States, all of which have helped me grow and become the woman I am today. My only hope is that I am able to make all of you proud.

TABLE OF CONTENTS

LIST OF TABLES

LIST OF FIGURES

LIST OF SYMBOLS

$\mathcal{N}$	number of bodies
$\mathbf{I}$	inertial frame
$\mathbf{R}$	rotating frame
$\mathbf{R_{inst}}$	instantaneous rotating frame
$\bar{r}$	position vector in rotating coordinates
$\bar{v}$	velocity vector in rotating coordinates
$\tilde{t}$	dimensional time
$\bar{R}$	position vector in J2000 inertial coordinates
$\bar{V}$	velocity vector in J2000 inertial coordinates
$\bar{R}_{inst}$	position vector in instantaneous rotating frame
$\bar{V}_{inst}$	velocity vector in instantaneous rotating frame
$\hat{X}$	x-axis in inertial frame
$\hat{Y}$	y-axis in inertial frame
$\hat{Z}$	z-axis in inertial frame
$\hat{x}$	x-axis in rotating frame
$\hat{y}$	y-axis in rotating frame
$\hat{z}$	z-axis in rotating frame
$\hat{x}_{inst}$	x-axis in instantaneous rotating frame
$\hat{y}_{inst}$	y-axis in instantaneous rotating frame
$\hat{z}_{inst}$	z-axis in instantaneous rotating frame
h	angular momentum in rotating frame
h_{inst}	angular momentum in instantaneous rotating frame
θ	rotation angle from inertial to rotating frame
θ_{inst}	rotation angle from inertial to instantaneous rotating frame
$\dot{\theta}$	dimensional mean motion
$\dot{\tilde{\theta}}$	non dimensional mean motion
$\tilde{G}$	dimensional universal gravitational constant
g_0	dimensional reference gravitational constant for system of interest

l^*	characteristic length
m^*	characteristic mass
t^*	characteristic time
t	non dimensional time
P_{i}	ith primary body
M_{i}	dimensional mass of ith body
C_{i}	numerical value of the Jacobi constant for a periodic orbit
n	number of patch-points
N	number of intermediate orbits
T	non dimensional thrust magnitude
$\tilde{T}$	dimensional thrust magnitude
I_{sp}	low-thrust engine specific impulse
α	in-plane thrust orientation angle
β	out-of-plane thrust orientation angle
$\mathcal{P}$	low-thrust engine power
$\bar{\mathcal{X}}$	vector of design —control— variables
$\mathbb{F}$	vector of constraints
$D\mathbb{F}$	matrix of partial derivatives
$\delta\mathcal{X}$	variations in the vector of control variables
ϵ	numerical methods tolerance
x	non-dimensional $x-$component of the spacecraft's position vector in rotating coordinates
y	non-dimensional $y-$component of the spacecraft's position vector in rotating coordinates
z	non-dimensional $z-$component of the spacecraft's position vector in rotating coordinates
$\dot{x}$	non-dimensional $x-$component of the spacecraft's velocity vector in rotating coordinates
$\dot{y}$	non-dimensional $y-$component of the spacecraft's velocity vector in rotating coordinates

$\dot{z}$	non-dimensional $z-$component of the spacecraft's velocity vector in rotating coordinates
L_{i}	ith Libration —Lagrangian— point
U^*	pseudo-potential function
U^*_{LT}	low-thrust augmented pseudo-potential function
μ	mass-ratio parameter
$\bar{a}_T$	thrust acceleration vector
$\hat{a}_T$	thrust acceleration unit vector
$\mathbf{G}$	augmented vector of constraints
$\mathcal{S}$	step size for pseudo-arc length continuation
$\sqcap$	null vector for a matrix
S	arbitrary cost function
q	arbitrary state variable
$\mathcal{L}$	arbitrary energy function
$\mathcal{H}$	arbitrary Hamiltonian function
$\mathcal{J}$	arbitrary objective function
$\mathcal{J}_a$	arbitrary augmented cost function
p	arbitrary optimization parameter
u	arbitrary control parameter
f	nonlinear function
$\bar{u}$	vector of control variables
$\bar{\lambda}$	vector of Lagrange multipliers
J	cost/objective function
L	Lagrangian function
H	Hamiltonian function
H_L	Hessian matrix
E	cost function for direct optimization
$\bar{c}$	vector of path constraints for direct optimization
$\bar{c}_l$	lower-bound on the path constraints
$\bar{c}_u$	upper-bound on the path constraints

$\bar{x}_l$	lower-bound on the state constraints
$\bar{x}_u$	upper-bound on the state constraints
$\bar{g}$	gradient of the performance function
$\mathbb{G}$	Jacobian matrix of equality constraint vector
$\mathcal{V}$	value function
Σ^+	surface of section —hyperplane—
ρ	mapping function

ABBREVIATIONS

LIC	Lunar IceCube
$\mathcal{N}BP$	$\mathcal{N}$-Body Problem
2BP	Two-Body Problem
CR3BP	Circular Restricted Three-Body Problem
EM	Earth-Moon
SEM	Sun-Earth-Moon
BKE	Basic Kinematic Equation
DCM	Direction Cosine Matrix
ET	Ephemeris Time
EOMs	Equations of Motion
nd	Non Dimensional
LT	Low-Thrust
CR3BP-LT	Low-Thrust Augmented Circular Restricted Three-Body Problem
VSI	Variable Specific Impulse
CSI	Constant Specific Impulse
AI	Artificial Intelligence
ANN	Artificial Neural Network
LPO	Libration Point Orbits
K	Constant of Integration
JC	Jacobi Constant
DRO	Distant Retrograde Orbits
NRHO	Near Rectilinear Halo Orbits
LLO	Low Lunar Orbits
SPO	Short Period Orbits
ToF	Time of Flight
TPBVP	Two-Point Boundary Value Problem
NLP	Non-linear Programming
CoV	Calculus of Variations

DP	Dynamic Programming
DDP	Differential Dynamic Programming
SQP	Sequential Quadratic Programming
RL	Reinforcement Learning
KKT	Kraush-Kuhn-Tucker
ELT	Euler-Lagrange Theory
PoO	Principle of Optimality
HJB	Hamilton-Jacobi-Bellman
H.O.T	Higher-order Terms
SoS	Surface of Section
RP	Roughness Parameter
RPM	Roughness Parameter Map
RMS	Root Mean Squares
SS	Single Shooter
MS	Multiple Shooter
ES	Energy Surface
TRS	Thrust Range Surface

ABSTRACT

As cislunar and outer space exploration regains worldwide popularity, the low-thrust spacecraft technology, whether in the form of solar sails, electric propulsion or nuclear propulsion, has seen a major increase in the last two decades, as new technologies arise that not only seek for a reduction of the size of the spacecraft —and/or the payloads— but also to minimize the cost of spaceflights, while trying to approach further destinations in our solar system. Mission designers are being challenged with the need to develop new strategies to generate rapid and informed initial guesses for low-thrust spacecraft trajectory design, that are easily converged into fully continuous solutions in position, velocity and mass states, in a high-fidelity dynamical model that incorporates the true ephemerides and perturbations of the gravitational attracting bodies acting on the spacecraft as it navigates through space.

In an effort to explore further mission options for spacecraft traveling in the lunar vicinity, new interest arises into the problem of constructing a general framework for the initial guess generation of low-thrust trajectories in cislunar space, that is independent of the force models in which the orbits of interest are defined. Given the efficiency of the low-thrust engines, most vehicles are equipped to perform further exploration of the cislunar space after completion of their primary science and technology demonstrations in orbits around the Moon. In this investigation, a generalized strategy for constructing initial guesses for low-thrust spacecraft traveling between lunar orbits that exist within the context of multiple dynamical models is presented. These trajectories are converged as mass-optimal solutions in lower fidelity model, that are easily transitioned and validated in the higher-fidelity ephemeris model, and, achieve large orbital plane changes while evolving entirely within the cislunar region.

The robustness of the initial guess generation of the spacecraft's path, depends highly on the fidelity of the dynamical model utilized to construct such trajectories, as well as on the numerical techniques employed to converge and propagate them into continuous solutions. Other researchers have extensively investigated novel techniques for the generation of initial guesses for the low-thrust spacecraft trajectory design problem including, but not limited to, patched conics strategies, methodologies for the transformation of impulsive burns into finite burns, the orbit chaining framework and, more recently, artificial intelligence schemes. This

investigation develops an adaptive orbit chaining type approach that relies on the energy parametrization of periodic orbits that exist within the context of the circular restricted three-body problem, to construct informed initial guess for the low-thrust spacecraft trajectory.

A variety of multiple transfer applications for vehicles traveling between orbits in the cislunar region is explored for a wide range of low-thrust spacecraft with varying thrust acceleration magnitude. The examples presented in this investigation are consistent with the low-thrust parameters of previously flown missions that utilized the same propulsion capabilities, such as, the DAWN mission and the Japanese Hayabusa missions 1 and 2. The trajectories presented in this work are optimized for either propellant consumption or time-of-flight in the lower-fidelity model, and later transitioned into a higher-fidelity ephemeris model that includes the gravitational attraction of the Sun, the Earth and the Moon.

Two strategies are explored for the transition of trajectories from a lower-fidelity model to the higher-fidelity ephemeris model, both of which are successful in retaining the transfer geometry. The framework presented in this investigation is further applied to the upcoming NASA Lunar IceCube (LIC) mission to explore possible extended mission options once its primary science and technology demonstration objectives are achieved. It is demonstrated in this investigation that the strategies developed and presented in this work are not only applicable to the specific low-thrust vehicles explored, but it is applicable to any spacecraft with any type of propulsion technology. Furthermore, the energy-informed adaptive algorithm is easily transition to generate trajectories in a range of varying dynamical models.

1. INTRODUCTION

While it is known that there exists no closed-form solution to solve the problem of a spacecraft moving under the perturbation of $\mathcal{N}$ gravitational attracting bodies ($\mathcal{N}$ primary bodies) —the $\mathcal{N}$-body problem— Diacu [1], numerical methods offer valuable techniques for describing and understanding this motion. The study of numerical methods dates back to Lorenz [2], Hénon and Heiles [3], whose insight into solving astrodynamics problems is still used today's applications. The application of numerical techniques into solving trajectory design problems, offers an infinite number of solutions, which motivates current researchers and mission designers to explore and develop novel strategies that help uncover some of the yet undiscovered motion of spacecraft in specific regions of space.

Some of the most popular strategies for solving an astrodynamics problem in which a spacecraft moves under the perturbation of more than two primary bodies via numerical methods, is the application of the commonly known shooting methods. Shooting techniques explicitly integrate the equations of motion that govern the path of a spacecraft to determine the numerical value of the control variables that meet a set of constraint equations. The simplest form of a shooting algorithm is the single shooting approach. Increasing the complexity of the single shooting follows the definition of the multiple shooting scheme, that discretizes the trajectory into patch-points and segments, such that, each individual arc is treated as a single shooting event. Moreover, the multiple shooting approach can be analyzed as a series of concatenated single shooting arcs linked together, as developed by Keller [4] and Stoer and Burlisch [5]. In the mission design applications, Gómez [6] is one of the pioneers of utilizing multiple shooting strategies to solve the trajectory design problem, followed by Mondelo [7], Howell et al.[8], and Pavlak [9]. Shooting algorithms are iterative methods that require an initial condition to be initialized.

The process of designing trajectories for spacecraft in cislunar orbits is similar whether the vehicle is propelled by a chemical engine or within a low-thrust regime; it starts with the construction of an initial guess for the spacecraft's path. As numerical methods are iterative by nature, the algorithms are initialized with a user supplied initial condition; successive updates are made that drive the initial estimate to meet all the problem constraints until a converged solution is found. The initial guess of the trajectory not only drives the geometry of the converged path, but also determines the successful performance of the algorithm, as poor initial guesses might cause a corrections process or an optimizer to diverge. The construction of an informed initial guess for a numerical method is then a important area of research that is currently still under development.

Vehicles propelled within the low-thrust engine regime encompass a variety of different propulsion technologies from ion engines to solar sails, and typically exchange thrust force for engine efficiency. These concepts were introduced in the early 20th century [10]; design and technology demonstrations of low-thrust engines have been laid in since the 1950s [11], but it was not until recent decades that the first low-thrust spacecraft missions were flown. Some of this missions include Deep Space 1 [12], Dawn [13], and Hayabusa 1 and 2 [14]. However, the low-thrust trajectory design problem still poses challenges when analyzed as an optimal control problem, since the determination of the control variables that optimize an objective function —typically propellant consumption or time-of-flight— is a non trivial process.

There exist multiple techniques to address the initial guess generations of low-thrust spacecraft trajectories, one of which is the orbit chain approach. This strategy offers a flexible methodology for connecting dynamical structures —periodic orbits or manifold arcs— to construct the initial guess for the numerical algorithms to converged into a continuous solution. In the low-thrust trajectory design framework for specified departure and arrival orbits, the basic approach of the orbit chaining strategy is to leverage the natural dynamics that exists within any dynamical model, to patch together intermediate arcs to aid in the construction of an informed initial guess for the low-thrust transfer. Typically, these intermediate arcs consist of either periodic orbits that exist within the context of lower fidelity force models, or, natural structures, such as manifold arcs, that traverse the region of interest in space. To select an appropriate set of intermediate arcs, the utilization of an energy parametrization of the space to generate fully continuous paths in position, velocity and mass states, and, to deliver mass-optimal solutions is developed in this investigation. The strategy presented in this work is utilized to construct initial guesses for CubeSat-type spacecraft transfers, under the assumptions of the Two-Body Problem (TBP) and the Circular

Restricted Three-Body Problem (CRTBP) lower-fidelity models, that are later transitioned into a higher fidelity ephemeris model. Low-thrust trajectories for spacecraft traveling in cislunar space are generated via a modified version of the traditional orbit chaining framework. This strategy is employed regardless of the force model in which the departure and arrival orbits exits, and, a step-by-step approach is provided for the construction of informed initial guesses for the trajectory design problem.

Furthermore, a natural parameter continuation method is successfully introduced into the implementation of a generalized modified orbit chaining technique, that leverages an energy-informed adaptive sliding algorithm to navigate the cislunar space in the creation of informed initial guesses, and delivers optimal trajectories for low-thrust spacecraft moving in the vicinity of the Moon.

1.1 State of the Art

Many authors have contributed throughout the years to the development of generalized methods for the low-thrust spacecraft trajectory design problem, specially the field of initial guess generation. Whether the solutions are presented in lower-fidelity models such as, the two-body and three-body problems, or in a higher-fidelity ephemeris model, all techniques are met with benefits and drawbacks that present itself more or less challenging depending on the type of spacecraft being considered, as well as the number and nature of the perturbations introduced in the equations of motion.

1.1.1 A Summary of the Development of the Orbit Chaining Framework

Howell, Barden, and Lo [15] demonstrated the orbit chaining strategy by link manifold arcs to transfer between periodic orbits within the context of the circular restricted three-body problem (CRTBP). Their explorations and investigations in the trajectory design problem, led the path for the NASA Genesis mission [16]. Later, Koon et al. [17] presented their work on "dynamical chains" in which heteroclinic and homoclinic connections are linked to uncover three-dimensional natural flow to and from periodic orbits in the CRTBP, including the Jupiter system, for which tours of the Jovian moons were explored

[18]. Ross and Lo [19] describe an "Interplanetary Superhighway" that expands across the solar system, as a series of manifold tubes linked together. These manifolds are also derived within the context of the three-body problem dynamical model.

Lo and Parker [20], and Parker et al. [21], continue the exploration of orbit chaining by developing a generalized scheme to transfer between periodic orbits in the vicinity of the libration points. Vaquero and Howell [22] explored resonant orbits within the context of the CRTBP, as possible arcs to utilize in the construction of initial guesses using the orbit chaining approach. Haapala and Howell [23] created a catalog of heteroclinic and homoclinic connections for transfers between libration point orbits (LPOs) within the context of the three-body force model, by utilizing invariant manifolds.

More recently, Restrepo and Russell [24] developed the "Patched Periodic Orbits" strategy for the fast design of low-thrust trajectories in the CRTBP, in which successive periodic orbits are patched together. Das-Stuart [25] develops a framework that combines dynamical systems theory with artificial intelligence and machine learning techniques to aid in the rapid generation of initial guesses. Pritchett [26] combines together periodic orbit chains in various dynamical structures that helps with the construction of the initial guess for the low-thrust spacecraft trajectory design.

Most of these authors rely on numerical techniques —mainly multiple shooting and optimizations methods — to transition the initial guess of the trajectory generated via the orbit chaining framework into a fully continuous solution between two orbits. Some of the benefits of the multiple shooting techniques include, but are not limited to, the sensitivity of the initial guess being distributed across multiple patch-points; the geometry of the initial guess being retained; a wider convergence radius since the error is distributed across the entire trajectory. As the focus of this investigation is to develop alternate strategies for the initial guess generation of low-thrust spacecraft trajectories within the context of the circular restricted three-body problem, some of the contributions within this regime are presented in the following section.

1.1.2 Advances in the Circular Restricted Three-Body Problem

The study of the circular restricted three-body problem dates back to Newton in 1687 [27], when the exploration of the interaction between multiple gravitational celestial bodies was introduced. In 1772, Lagrange determined the existence of five equilibrium points in the three-body problem, that are also known as Lagrangian or libration points. Poincaré explored the existence of periodic motion around these Lagrangian points [28], and opened the space to an infinite number of possibilities for spacecraft motion under this regime. In 1920, Moulton [29] published the book Periodic Orbits, in which analytical methods for approximating periodic orbits in the vicinity of the Lagrangian points is explored.

In 1965, Hénon [30] published on stability and bifurcations of periodic solutions, while Goodrich [31] explored orbits in the vicinity of the non-collinear libration points in the Earth-Moon system. At around the same time period, Szebehely [32] published his book ”Theory of Orbits: The Restricted Problem of Three Bodies”, and, in 1968 Broucke [33] completed an analysis of planar motion and bifurcations in the RTBP. Breakwell and Brown [34] explored the existence of halo orbits in the Earth-Moon system while Zagouras and Kazantzis [35] in 1979, explored the existence of halo, axial, and vertical families of orbits in the Sun-Jupiter RTBP system. Howell [36] completed an extensive investigation of the halo family of orbits. Furthermore, In 1999, Howell and Campbell [37] performed an extensive investigation of periodic family of orbits and their stability in the Sun-Earth/Moon system.

More recently, Grebow [38] computed many periodic orbits within the context of the Earth-Moon CRTBP. Anderson and Lo [39] exploited the use of Poincaré maps and invariant manifolds to study motion in the Jupiter- Europa R3BP system, and explored the low-thrust trajectory design problem within this regime. Cox [40] created a catalog of dynamical structures from the CRTBP that includes both, gravitational dynamics and the low-thrust force.

Dynamical structures that exist within the context of the CRTBP are nowadays a fundamental part of the work performed by mission designers. Some of the more recent mission examples that will enable low-thrust spacecraft trajectory design in the Earth-Moon CRTBP system are the Lunar IceCube [41] mission, as well as the NASA’s Artemis-1 mission [42].

Furthermore, many other authors and researchers have contributed to the development of the theory behind the circular restricted three-body problem regime, as new periodic motion in the vicinity of the Lagrangian points continues to be unveiled.

1.1.3 Low-thrust Enabled Trajectory Design

The low-thrust enabled trajectories in the CRTBP are often referred to as low-energy transfers. These transfer have been computed by many authors using different techniques, some of which include the addition of natural or ballistic arcs in the construction of the initial estimate for the trajectory. Two types of low-thrust propulsion are considered in this investigation: one whose engine efficiency possesses a Constant Specific Impulse (CSI), as well as the VASIMIR engine [43] that operates on a Variable Specific Impulse (VSI) regime.

Parker and Anderson [44], as well as Mingotti and Topputo [45] explored a variety of low-thrust trajectories in the Earth-Moon CRTBP system and their applications. Furthermore, the successfully flown SMART-1 mission employed an electric propulsion type of engine to transfer from the Earth to the vicinity of the Moon [46]. Grebow et al. [47], [48] studied long-duration coverage of pole-sitter orbits with a low-thrust spacecraft with electric propulsion. Betts [24] solved the continuous problem of obtaining time-history for the thrust control orientation vector despite computational difficulties. Radice and Olmo [49], Ceriotti and Vasile [50], Stuart and Howell [51], as well as Furfaro and Linares [52], among others, offer solutions of the low-thrust problem via optimization techniques and the convergence of locally optimal solutions. Witsberger and Longuski [53] and De Smet et al. [54] utilized Artificial Neural Networks (ANNs) to construct solutions for interplanetary transfers. Miller and Linares [55], as well as Das-Stuart et al. [56] leverage Reinforcement Learning (RL) techniques into the a low-thrust spacecraft trajectory design.

Some examples of previuosly flown low-thrust missions include the Deep Space 1 mission to the McAuliffe asteroid and the West-Kohoutek-Ikemura comet [57], the Dawn mission to the dwarf planets Vesta and Ceres [58], and the Hayabusa 1 and 2 missions to the Itokawa and Ryugu asteroids [14], [59]. Some examples of future low-thrust missions include the Lunar IceCube spacecraft [41], and NASA's Gateway mission [42]. As low-thrust technologies continue to be developed and tested, the number of low-thrust-enabled missions within the context of the circular restricted three-body problem will increase, and more strategies will need to be designed and validated.

1.2 Thesis Overview

Even though the advantages of low-thrust propulsion for spacecraft were analyzed long before the technology was ready for implementation in an actual mission, much analysis continues on the topics of spacecraft trajectory optimization and low-thrust transfer design in the cislunar vicinity; such trajectories minimize parameters such as the propellant consumption or time-of-flight. When direct and indirect optimization strategies are incorporated into the low-thrust transfer design process, it enables the identification of locally optimal solutions that extremize the control parameters [60], [61].

It is then the goal of this investigation to explore the time-of-flight and propellant usage trade-offs in the design of low-cost low-thrust transfers in cislunar space, by leveraging an energy-informed control and optimization strategy. This analysis seeks to address this goal by exploring the answers to the following fundamental questions:

1. Can an automated algorithm be developed to further exploit orbit chaining with natural arcs for initial guess generation of low-thrust transfers in the lunar vicinity?

2. Do transfer geometries that escape the system always provide a better propellant consumption performance?

3. What is the impact of the thrust acceleration level in the geometry of a low-thrust transfer within the context of the CR3BP?

Each of the previous queries introduces a new challenge into the low-thrust transfer design, possibly in the form of additional constraints, or by developing suitable and rapid strategies to generate feasible and informed initial conditions for the numerical corrections process. Furthermore, these strategies should produce robust low-cost optimal solutions that are easily translated to a higher fidelity ephemeris model.

This work is organized in the following manner:

- **Chapter 2. Low-thrust Spacecraft Dynamical Models.**

  Within the context of trajectory design for vehicles powered by low-thrust engines in the vicinity of the Moon, a first step in the analysis is the development of a dynamical model that describes the motion of the spacecraft in a multi-body environment, while incorporating the additional acceleration term provided by the thrust force. The complexity of this design will be addressed first, by understanding the dynamics of the low-thrust spacecraft in an environment where only the gravitational acceleration of the Earth and the Moon are incorporated, without any additional perturbations, and later expanding this dynamical fidelity to a model that includes the gravitational attraction of the Sun as a third body perturbation.

- **Chapter 3. Low-thrust Spacecraft Optimization Techniques.**

  With the thrust acceleration of the spacecraft being the main control variable for a low-thrust vehicle in the CRTBP-LT regime, an informed guess for the control history becomes crucial to determining a continuous solution to the equations of motion. Furthermore, this solution is expected to satisfy certain constraints along the path, while minimizing a predetermined performance function that supports the mission application requirements. To identify a suitable control history for the thrust acceleration terms, optimal control theory is employed, and both direct and indirect methods are explored to minimize the propellant consumption of the spacecraft, along with the time-of-flight of the trajectories.

- **Chapter 4. Cislunar Trajectory Design Framework.**

  An automated algorithm that generates sliding-type geometry initial guesses, and locally optimal converged solutions, is developed in trying to answer the first fundamental question. This algorithm exploits natural arcs within the orbit chaining framework, to construct trajectories for low-thrust spacecraft between libration point orbits in the vicinity of the Moon. The sliding-type algorithm consists of constructing the initial guess based on the selection of a set of intermediate orbits patched together from the departure to the arrival orbits. These orbits can belong to either of the families, that is, the departure or destination orbits, or could belong to a completely different family of periodic orbits that lie in the vicinity of the orbits of interest. Furthermore, this algorithm offers the capability to identify interior transfer geometries when manifolds arcs are not available, e.g., when transferring between stable periodic orbits.

- **Chapter 5. Applications.**

  Results for the performances obtained with the energy-informed adaptive sliding algorithm are demonstrated in a variety of applications for a low-thrust spacecraft with a VSI engine model, travelling between orbits in the vicinity of the Moon. A special application is examined in an effort to explore further extended mission options for the secondary payload riding along the NASA Artemis-1 spacecraft [62], the Lunar IceCube (LIC) satellite. New interest arises into the problem of constructing a general framework for the initial guess generation of low-thrust trajectories in cislunar space, that is independent of the force models in which the orbits of interest are defined. Given the efficiency of the LIC low-thrust engine [63], after completion of its primary science and technology demonstrations in an orbit around the Moon, the spacecraft could perform further exploration of the cislunar space. These trajectories are converged as mass-optimal solutions in lower fidelity model, that are easily transitioned and validated in the higher fidelity ephemeris model, and, achieve large orbital plane changes while evolving entirely within the cislunar region.

- **Chapter 6. Concluding Remarks.**

  A summary of the trajectory design framework developed in this investigation is summarized in this chapter, along with the conclusions drawn from the results of the sample applications. Potential recommendations for future work are also offered.

2. LOW-THRUST SPACECRAFT DYNAMICAL MODELS

When exploring strategies for designing trajectories for vehicles moving in outer space, the very first step consists of understanding the environment in which these vessels will be navigating. Questions arise concerning the effects of the perturbations that the spacecraft will undergo, such as, but not limited to, the number of gravitational forces acting on the body, parameter that determines the dynamical sensitivity of a particular region in space. While it is impossible to accurately and precisely model every individual celestial body that resides in the outer space, scientists and researchers throughout history have tried to understand and approximate the motion of the celestial bodies, providing sufficient information that enables the capability to produce high fidelity dynamical models that describe the path of a natural satellite moving in a particular region of space.

One example of such data, for a high fidelity model of the motion of natural satellites is found in the ephemeris files provided by the Solar Systems Dynamics Group of the NASA Jet Propulsion Laboratory (JPL) in Pasadena, California; This data is obtained either via the JPL Horizons online system, or, via the ephemeris files in SPK format from the JPL's NAIF website. The ephemeris data is utilized to approximate the true path of the celestial bodies as seen by an observer fixed in an inertial reference frame. Furthermore, the number of celestial bodies incorporated in a dynamical model to approximate the motion of an artificial spacecraft moving in space, determines the fidelity of such force model approximation. If the spacecraft undergoes the gravitational perturbation of $\mathcal{N}$ attracting bodies, this force model is referred to as the $\mathcal{N}$-Body Problem ($\mathcal{N}$BP). The larger the number of celestial bodies included in the model —the numerical value of $\mathcal{N}$— the higher the fidelity of the dynamical model approximating the perturbations acting on the motion of the spacecraft.

Although there exist a variety of mathematical formulations to describe the path of a spacecraft under the perturbation of $\mathcal{N}$ attracting bodies, there exists however not known analytical solution to describe the motion of a vehicle moving under the perturbation of more than two gravitational accelerations. This problem is the well known Two-Body Problem (2BP), for which Kepler found a closed-form solution in the form of conics —circles, ellipses, hyperbolas and parabolas—. The 2BP is the dynamical model with the lowest fidelity of perturbations, in which the gravitational attraction of only one attracting body is utilized to model the forces under which a spacecraft is navigating in space. For instance, the Sun-Mars system, Earth-Moon system, or Earth-Spacecraft system, are all examples of models in which only one perturbing body is included to understand the motion of a satellite traveling in its proximity.

When the effects of a second gravitational attraction is included in the model, this dynamical environment is now considered the three-body problem. Furthermore, if the two primaries are orbiting in circular motion around their common barycenter, this is called the Circular Restricted Three-Body Problem (CR3BP). This model is of particular interest since, even though there exist no analytical, or closed-form solution, to describe the motion of the spacecraft in this regime, numerical methods and computational propagation are leveraged to generate closed trajectories for vehicles. Moreover, some of these paths are periodic in configuration space, resulting in the generation of periodic orbits.

2.1 Coordinate Frames

To represent a vector quantity —magnitude and direction— in a three-dimensional space, a set of three infinite axes perpendicular to each other is utilized. The direction of each axis is represented by a unit vector, such that, the set of the three unit vectors perpendicular to each other is referred to as a coordinate frame. Moreover, even though the axes of a coordinate frame are infinite, an origin or base-point is identified, that locates any vector quantity in space with respect to the particular coordinate frame.

Coordinate frames can be inertially fixed in space —inertial frames—, or can rotate about its origin at a specified angular rate —rotating frames—. Furthermore, as illustrated in Figure 2.1, multiple frames can share the same origin or based-point, regardless of whether the set of axes are inertial or rotating. Figure 2.1 is a generic representation of an arbitrary inertial frame, **I**, with coordinates $\{\hat{X}, \hat{Y}, \hat{Z}\}$ and an arbitrary rotating frame, **R**, with coordinates $\{\hat{x}, \hat{y}, \hat{z}\}$, that rotate about their common based-point at an angular rate $\dot{\theta}$.

In the process to develop the equations of motion of a spacecraft moving under the perturbation of multiple gravitational accelerations, using either a Newtonian or a Hamiltonian formulation, the first step is to identify its position and velocity vectors with respect to an

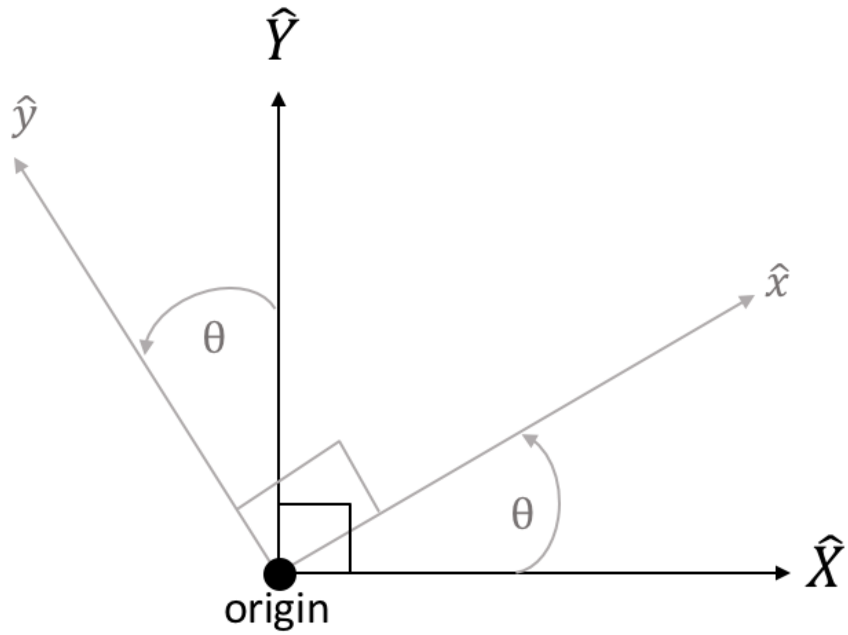

Figure 2.1. Generic representation of an arbitrary inertial and rotational coordinate frames with the same base-point origin

inertial coordinate frame. Depending on the dynamical model being utilized, the inertial frame however, is not always the better choice to observe and understand the path of a space vehicle. Therefore, a transformation from an inertial to a rotational frame is often times necessary.

2.1.1 Transformation Between Rotating and Inertial Coordinate Frames

To illustrate the process to transform a vector from an arbitrary inertial reference frame to a rotational reference frame and vice versa, consider the position and velocity vectors for a spacecraft expressed in terms of the rotating coordinates in Figure 2.1:

$$\bar{r} = \begin{bmatrix} x & y & z \end{bmatrix} \tag{2.1}$$

$$\bar{v} = \frac{{}^{R}d\bar{r}}{dt} = \begin{bmatrix} \dot{x} & \dot{y} & \dot{z} \end{bmatrix} \tag{2.2}$$

By applying the basic kinematic equation (BKE), an expression for the velocity vector in inertial coordinates is found as follows:

$$\frac{{}^{\mathbf{I}}d\bar{r}}{dt} = \frac{{}^{\mathbf{R}}d\bar{r}}{dt} + {}^{\mathbf{I}}\bar{\omega}^{\mathbf{R}} \times \bar{r} \tag{2.3}$$

where ${}^{\mathbf{I}}\bar{\omega}^{\mathbf{R}} = \dot{\theta}\hat{z}$ represents the angular velocity of the rotating frame with respect to the inertial frame. $\frac{{}^{\mathbf{I}}d\bar{r}}{dt}$ corresponds to the derivative of the position vector with respect to time as seen by an inertial observer, and $\frac{{}^{\mathbf{R}}d\bar{r}}{dt}$ corresponds to the time rate of change of the position vector with respect to an observer fixed in the rotating frame:

$$\begin{aligned} \frac{{}^{\mathbf{I}}d\bar{r}}{dt} &= \bar{v} + \dot{\theta}\hat{z} \times \bar{r} \\ &= \begin{bmatrix} \dot{x} & \dot{y} & \dot{z} \end{bmatrix} + \dot{\theta}\hat{z} \times \begin{bmatrix} x & y & z \end{bmatrix} \\ &= \left(\dot{x} - \dot{\theta}y\right)\hat{x} + \left(\dot{y} + \dot{\theta}x\right)\hat{y} + \dot{z}\hat{z} \end{aligned} \tag{2.4}$$

If both reference frames are assumed to be initially aligned, i.e., at time $t = 0$, the angle $\theta = 0$ deg, such that:

$$\begin{aligned} \hat{x}(t = 0) &= \hat{X}(t = 0) \\ \hat{y}(t = 0) &= \hat{Y}(t = 0) \\ \hat{z}(t = 0) &= \hat{Z}(t = 0) \end{aligned}$$

then, the Direction Cosine Matrix (DCM) that relates the two coordinate frames is obtained by a simple rotation of θ degrees about the $\hat{z}-$ axis (that is equivalent to the inertial $\hat{Z}-$ axis for all times) as follows:

$${}^{\mathbf{I}}C^{\mathbf{R}} = \begin{bmatrix} cos(\theta) & -sin(\theta) & 0 \\ sin(\theta) & cos(\theta) & 0 \\ 0 & 0 & 1 \end{bmatrix} \tag{2.5}$$

Thus, to transform the position vector from rotational to inertial coordinates, the following matrix operation is performed:

$$
\begin{bmatrix} X \\ Y \\ Z \end{bmatrix} = \begin{bmatrix} cos(\theta) & -sin(\theta) & 0 \\ sin(\theta) & cos(\theta) & 0 \\ 0 & 0 & 1 \end{bmatrix} \begin{bmatrix} x \\ y \\ z \end{bmatrix} \tag{2.6}
$$

or, in a more compact form:

$$
\begin{bmatrix} X \\ Y \\ Z \end{bmatrix} = {}^{\mathbf{I}}C^{\mathbf{R}} \begin{bmatrix} x \\ y \\ z \end{bmatrix} \tag{2.7}
$$

Likewise, to transform the velocity vector from rotating to inertial coordinates, apply the chain rule of derivatives to Equation 2.7, such that, the time derivative of the DCM is employed to compute the inertial velocity as follows:

$$
\begin{bmatrix} \dot{X} \\ \dot{Y} \\ \dot{Z} \end{bmatrix} = {}^{\mathbf{I}}C^{\mathbf{R}} \begin{bmatrix} \dot{x} \\ \dot{y} \\ \dot{z} \end{bmatrix} + {}^{\mathbf{I}}\dot{C}^{\mathbf{R}} \begin{bmatrix} x \\ y \\ z \end{bmatrix} \tag{2.8}
$$

Combining the results from Equations 2.7 and 2.8, delivers the transformation equation for the position and velocity vectors of a spacecraft from rotating to inertial coordinates:

$$
\begin{bmatrix} X \\ Y \\ Z \\ \dot{X} \\ \dot{Y} \\ \dot{Z} \end{bmatrix} = \begin{bmatrix} {}^{\mathbf{I}}C^{\mathbf{R}} & 0_{3\times 3} \\ {}^{\mathbf{I}}\dot{C}^{\mathbf{R}} & {}^{\mathbf{I}}C^{\mathbf{R}} \end{bmatrix} \begin{bmatrix} x \\ y \\ z \\ \dot{x} \\ \dot{y} \\ \dot{z} \end{bmatrix} \tag{2.9}
$$

One of the properties of transformation matrices —direction cosine matrices— is that their inverse is equal to their transpose:

$$
\left[{}^{\mathbf{I}}C^{\mathbf{R}}\right]^{-1} = \left[{}^{\mathbf{I}}C^{\mathbf{R}}\right]^{T} = {}^{\mathbf{R}}C^{\mathbf{I}}
$$

therefore, if the inverse process is required, in which it is desired to transition a position and velocity vectors from inertial to rotating coordinates, Equation 2.9 is modified as follows:

$$\begin{bmatrix} x \\ y \\ z \\ \dot{x} \\ \dot{y} \\ \dot{z} \end{bmatrix} = \begin{bmatrix} {}^{\mathbf{R}}C^{\mathbf{I}} & 0_{3\times3} \\ {}^{\mathbf{R}}\dot{C}^{\mathbf{I}} & {}^{\mathbf{R}}C^{\mathbf{I}} \end{bmatrix} \begin{bmatrix} X \\ Y \\ Z \\ \dot{X} \\ \dot{Y} \\ \dot{Z} \end{bmatrix} \tag{2.10}$$

where the rotation matrix from inertial to rotating coordinates is given by:

$${}^{\mathbf{R}}C^{\mathbf{I}} = \begin{bmatrix} cos(\theta) & sin(\theta) & 0 \\ -sin(\theta) & cos(\theta) & 0 \\ 0 & 0 & 1 \end{bmatrix} \tag{2.11}$$

The process described for transforming a position and velocity vector from inertial to rotating coordinates and vice versa, is applicable for any three-dimensional vector representing any quantity and its rate of change with respect to time.

2.1.2 Transformation Between Rotating and J2000 Inertial Reference Frame

The J2000 reference frame is an inertial coordinate frame whose origin —base point— is the Earth, and for which all directions are recorded on January 1^{st}, 2000 at 12:00:00 Ephemeris Time (ET). This is the most popular reference frame to utilize when modeling the motion of a spacecraft in a high fidelity ephemeris model, under the gravitational attraction of multiple celestial bodies, as all ephemeris in this frame are recorded as days past J2000.

Let $\bar{R}$ and $\bar{V}$ represent the inertial position and velocity vectors of a spacecraft with respect to an observer fixed in the Earth. Utilizing the ephemeris data, an instantaneous Earth-centered rotating frame $\mathbf{R}_{inst}$ is constructed as follows:

$$\hat{x}_{\text{inst}} = \frac{\bar{R}}{||R||} \tag{2.12}$$

$$\hat{z}_{\text{inst}} = \frac{\bar{R} \times \bar{V}}{||\bar{R} \times \bar{V}||} \tag{2.13}$$

$$\hat{y}_{\text{inst}} = \hat{z}_{inst} \times \hat{x}_{inst} \tag{2.14}$$

where $\{\hat{x}_{inst}, \hat{y}_{inst}, \hat{z}_{inst}\}$ are the individual components of the instantaneous rotating frame. In the J2000 coordinate frame, the angular velocity is no longer constant —as it is in the case of an arbitrary inertial frame— such that, this quantity must also be computed instantaneously:

$$\dot{\theta}_{inst} = \frac{h_{inst}}{R^2} = \frac{\bar{R} \times \bar{V}}{R^2} \tag{2.15}$$

In Equation 2.15, h_{inst} represents the instantaneous angular momentum derived from a two-body definition. Utilizing this definition for the angular rate, if the instantaneous rotational position is given by:

$$\bar{r}_{inst} = \begin{bmatrix} x_{inst} & y_{inst} & z_{inst} \end{bmatrix} \tag{2.16}$$

then, the instantaneous rotational velocity is obtained by applying the BKE as follows:

$$\frac{{}^{\mathbf{I}}d\bar{r}_{inst}}{d\tilde{t}} = \frac{{}^{\mathbf{R}_{inst}}d\bar{r}_{inst}}{d\tilde{t}} + {}^{\mathbf{I}}\bar{\omega}^{\mathbf{R}_{inst}} \times \bar{r_{inst}} \tag{2.17}$$

where ${}^{\mathbf{I}}\bar{\omega}^{\mathbf{R}_{inst}} = \dot{\theta}_{inst}\hat{z}_{inst}$ represents the angular velocity of the instantaneous rotating frame with respect to the J2000 inertial reference frame. $\frac{{}^{\mathbf{I}}d\bar{r}_{inst}}{d\tilde{t}}$ corresponds to the derivative of the position vector with respect to time as seen by an inertial observer fixed in the Earth, and $\frac{{}^{\tilde{\mathbf{R}}}d\bar{r}_{inst}}{d\tilde{t}}$ corresponds to the time rate of change of the position vector with respect to an observer fixed in the instantaneous rotating frame:

$$
\begin{aligned}
\frac{{}^{\mathbf{I}}d\bar{r}_{inst}}{d\tilde{t}} &= \bar{v}_{inst} + \dot{\theta}_{inst}\hat{z}_{inst} \times \bar{r}_{inst} \\
&= \begin{bmatrix} \dot{x}_{inst} & \dot{y}_{inst} & \dot{z}_{inst} \end{bmatrix} + \dot{\theta}_{inst}\hat{z}_{inst} \times \begin{bmatrix} x_{inst} & y_{inst} & z_{inst} \end{bmatrix} \\
&= \left(\dot{x}_{inst} - \dot{\theta}_{inst}y_{inst}\right)\hat{x}_{inst} + \left(\dot{y}_{inst} + \dot{\theta}_{inst}x_{inst}\right)\hat{y}_{inst} + \dot{z}_{inst}\hat{z}_{inst} \qquad (2.18)
\end{aligned}
$$

Following the same procedure to transform rotating coordinates to an arbitrary inertial frame, a transformation matrix —direction cosine matrix—- is required to transform rotating coordinates into a J2000 inertial reference frame. In this case, the rotation matrix is instantaneous, and it is constructed via the instantaneous rotating axes as follows:

$$
{}^{\mathbf{I}}C^{\mathbf{R}_{inst}} = \begin{bmatrix} \hat{x}_{inst} & \hat{y}_{inst} & \hat{z}_{inst} \end{bmatrix} = \begin{bmatrix} C_{11} & C_{12} & C_{13} \\ C_{21} & C_{22} & C_{23} \\ C_{31} & C_{32} & C_{33} \end{bmatrix} \qquad (2.19)
$$

such that, the instantaneous rotational position vector transformed into the J2000 inertial coordinates is given by:

$$
\begin{bmatrix} X \\ Y \\ Z \end{bmatrix} = \begin{bmatrix} C_{11} & C_{12} & C_{13} \\ C_{21} & C_{22} & C_{23} \\ C_{31} & C_{32} & C_{33} \end{bmatrix} \begin{bmatrix} x_{inst} \\ y_{inst} \\ z_{inst} \end{bmatrix} \qquad (2.20)
$$

or, simply written:

$$
\begin{bmatrix} X \\ Y \\ Z \end{bmatrix} = {}^{\mathbf{I}}C^{\mathbf{R}_{inst}} \begin{bmatrix} x_{inst} \\ y_{inst} \\ z_{inst} \end{bmatrix} \qquad (2.21)
$$

Moreover, from Equation 2.18, the instantaneous rotating velocity vector written in J2000 inertial coordinates, is given by:

$$
\begin{bmatrix} \dot{X} \\ \dot{Y} \\ \dot{Z} \end{bmatrix} = \begin{bmatrix} \dot{\theta}_{inst}C_{12} & -\dot{\theta}_{inst}C_{11} & 0 & C_{11} & C_{12} & C_{13} \\ \dot{\theta}_{inst}C_{22} & -\dot{\theta}_{inst}C_{21} & 0 & C_{21} & C_{22} & C_{23} \\ \dot{\theta}_{inst}C_{32} & -\dot{\theta}_{inst}C_{31} & 0 & C_{31} & C_{32} & C_{33} \end{bmatrix} \begin{bmatrix} x_{inst} \\ y_{inst} \\ z_{inst} \\ \dot{x}_{inst} \\ \dot{y}_{inst} \\ \dot{z}_{inst} \end{bmatrix} \tag{2.22}
$$

Combining the results from Equations 2.21 and 2.23, delivers the transformation equation for the position and velocity vectors of a spacecraft from an instantaneous rotating frame to J2000 inertial coordinates:

$$
\begin{bmatrix} X \\ Y \\ Z \\ \dot{X} \\ \dot{Y} \\ \dot{Z} \end{bmatrix} = \begin{bmatrix} C_{11} & C_{12} & C_{13} & 0 & 0 & 0 \\ C_{21} & C_{22} & C_{23} & 0 & 0 & 0 \\ C_{31} & C_{32} & C_{33} & 0 & 0 & 0 \\ \dot{\theta}_{inst}C_{12} & -\dot{\theta}_{inst}C_{11} & 0 & C_{11} & C_{12} & C_{13} \\ \dot{\theta}_{inst}C_{22} & -\dot{\theta}_{inst}C_{21} & 0 & C_{21} & C_{22} & C_{23} \\ \dot{\theta}_{inst}C_{32} & -\dot{\theta}_{inst}C_{31} & 0 & C_{31} & C_{32} & C_{33} \end{bmatrix} \begin{bmatrix} x_{inst} \\ y_{inst} \\ z_{inst} \\ \dot{x}_{inst} \\ \dot{y}_{inst} \\ \dot{z}_{inst} \end{bmatrix} \tag{2.23}
$$

Although the coordinate transformation process described in this section corresponds to an Earth-centered inertial frame, the process is applicable to any primary-centered coordinate frame, whether the goal is to transformed rotating coordinates into inertial quantities or vice versa.

2.2 Numerical Methods

To accurately represent the evolution of an unknown trajectory (be it a periodic orbit, or just an arbitrary path for a spacecraft travelling within a particular system), it is assumed that a set of terminal conditions must be satisfied. This becomes then a targeting problem for which end conditions are specified to be met while varying a set of initial conditions. The term 'shooting' is utilized to describe such targeting technique. The shooting methods necessitate iterations on the initial conditions that need be updated to meet the final targeting conditions, hence, these methods are separated into three main steps:

- Step 1. Targeting the desired states
- Step 2. Correcting for deviations
- Step 3. Updating the initial states

Steps 1 through 3 are implemented iteratively, until the desired target conditions are met. One of the most popular ways to formulate the iterative process is by rearranging the system of differential equations that drive the motion of the vehicle as a set of first-order differential equations, and implementing a Newton-Raphson strategy. Furthermore, this strategy implies knowledge of the partial derivatives of the system, that is, knowledge about the sensitivity of the final states to the initial states (also known as the State Transition Matrix, STM), as well as the sensitivity of the terminal conditions —or constraints— to the initial states.

2.2.1 Newton-Raphson Method

Within the context of a Newton-Raphson technique, let $\bar{\mathcal{X}}$ be a vector of design variables —or controls— that are part of the state vector in a set of first-order differential equations of motion, and are to be modified in order to meet a set of terminal constraints on the states:

$$\bar{\mathcal{X}} = \begin{bmatrix} \mathcal{X}_1 \\ \mathcal{X}_2 \\ \mathcal{X}_3 \\ \vdots \\ \mathcal{X}_n \end{bmatrix} \tag{2.24}$$

Let the terminal constraints be the components of a vector of targeting conditions, $\mathbf{F}(\bar{\mathcal{X}})$, such that, the goal of the iterative algorithm is to find the initial value of the control variables, $\bar{\mathcal{X}}$, that drive the vector of constraints to zero, i.e., $\mathbf{F}(\bar{\mathcal{X}}) = 0$.

$$\mathbf{F}(\bar{\mathcal{X}}) = \begin{bmatrix} F_1(\bar{\mathcal{X}}) \\ F_2(\bar{\mathcal{X}}) \\ F_3(\bar{\mathcal{X}}) \\ \vdots \\ F_k(\bar{\mathcal{X}}) \end{bmatrix} = \bar{0} \tag{2.25}$$

In theory, the solution to Equation 2.25 is attained by iterating on the control variables until each individual condition is set to zero; in practice, solutions satisfying $\mathbf{F}(\bar{\mathcal{X}}) < \epsilon$ are sought instead, where ϵ is a user-defined tolerance that accommodates for numerical errors during the convergence process.

One characteristic of the numerical methods is that an initial condition for the control variables, $\bar{\mathcal{X}}_0$, is needed to initialize the iterations process. Moreover, an update equation is derived that feeds the current initial conditions and approximates the deviations on the terminal constraints. To derive the update equation, a first-order Taylor series expansion about $\bar{\mathcal{X}}_0$ is applied to $\mathbf{F}(\bar{\mathcal{X}})$, such that:

$$\mathbf{F}(\bar{\mathcal{X}} + \delta\bar{\mathcal{X}}_0) \approx \mathbf{F}(\bar{\mathcal{X}}_0) + D\mathbf{F}(\bar{\mathcal{X}}_0)(\bar{\mathcal{X}} - \bar{\mathcal{X}}_0) \tag{2.26}$$

where $D\mathbf{F}(\bar{\mathcal{X}}_0)$ is the matrix of partial derivatives of the constraints with respect to the control variables, given by:

$$D\mathbf{F}(\bar{\mathcal{X}}_0) = \frac{\partial \mathbf{F}(\bar{\mathcal{X}})_0}{\partial \bar{\mathcal{X}}_0} = \begin{bmatrix} \frac{\partial F_1}{\partial \mathcal{X}_1} & \frac{\partial F_1}{\partial \mathcal{X}_2} & \cdots & \frac{\partial F_1}{\partial \mathcal{X}_n} \\ \frac{\partial F_2}{\partial \mathcal{X}_1} & \frac{\partial F_2}{\partial \mathcal{X}_2} & \cdots & \frac{\partial F_2}{\partial \mathcal{X}_n} \\ \vdots & \vdots & \ddots & \vdots \\ \frac{\partial F_m}{\partial \mathcal{X}_1} & \frac{\partial F_m}{\partial \mathcal{X}_2} & \cdots & \frac{\partial F_m}{\partial \mathcal{X}_n} \end{bmatrix}_{t_0} \tag{2.27}$$

Let the variations of the control vector around the initial conditions be defined as $\delta\bar{\mathcal{X}} = (\bar{\mathcal{X}} - \bar{\mathcal{X}}_0)$, such that. Generalizing this realization such that $\bar{\mathcal{X}}_0)$ represents the initial conditions at any point in time t_i, Equation 2.26 can be rewritten as:

$$\mathbf{F}(\bar{\mathcal{X}}_{\mathrm{i}+1} + \delta\bar{\mathcal{X}}_\mathrm{i}) \approx \mathbf{F}(\bar{\mathcal{X}}_\mathrm{i}) + D\mathbf{F}(\bar{\mathcal{X}}_\mathrm{i})(\bar{\mathcal{X}}_{\mathrm{i}+1} - \bar{\mathcal{X}}_\mathrm{i}) = 0 \tag{2.28}$$

To solve for Equation 2.28 utilizing matrix algebra, the solution varies depending on the size of the matrix of partial differential equations, which ultimately relates to the size of the vector of control variables, n, and the size of the vector of constraints, m.

Size of the State Vector Equals Size of Vector of Constraints

The case for which $n = m$ in Equation 2.28, suggests that the number of control variables is exactly equal to the number of constraint equations, in which case, the matrix of partial derivatives $D\mathbf{F}$ is a square matrix. The iterative process consists of updating the vector of controls until the vector of constraints approaches zero. If $\bar{\mathcal{X}}_{\mathrm{i}}$ represents the initial condition for the iterations process at time t_{i}, then the updated vector of control variables at time $t_{\mathrm{i+1}}$, $\bar{\mathcal{X}}_{\mathrm{i+1}}$, is found by rearranging Equation 2.28, as follows:

$$\bar{\mathcal{X}}_{\mathrm{i+1}} = \bar{\mathcal{X}}_{\mathrm{i}} - D\mathbf{F}(\bar{\mathcal{X}}_{\mathrm{i}})^{-1}\mathbf{F}(\bar{\mathcal{X}}_{\mathrm{i}}) \tag{2.29}$$

Equation 2.29 assumes that the matrix $D\mathbf{F}$ is invertible, and that a unique solution exist. The iteration process continues until $\mathbf{F}(\bar{\mathcal{X}}_{\mathrm{i}}) < \epsilon$.

Size of the State Vector Greater than Size of Vector of Constraints

The case for which $n > m$ in Equation 2.28, suggests that the number of control variables is greater than the number of constraint equations, in which case, the matrix of partial derivatives $D\mathbf{F}$ is a rectangular matrix. In this scenario, an infinite number of solutions exist, one of which is known as the minimum-norm solution, whose goal is to identify the solution closest to the vector of control variables at time t_{i}. The minimum-norm solution is found by as follows:

$$\bar{\mathcal{X}}_{\mathrm{i+1}} = \bar{\mathcal{X}}_{\mathrm{i}} - D\mathbf{F}(\bar{\mathcal{X}}_{\mathrm{i}})^T \left[D\mathbf{F}(\bar{\mathcal{X}}_{\mathrm{i}})D\mathbf{F}(\bar{\mathcal{X}}_{\mathrm{i}})^T\right]^{-1} \mathbf{F}(\bar{\mathcal{X}}_{\mathrm{i}}) \tag{2.30}$$

Similar to the procedure in Equation 2.29, it is assumed that Equation 2.30 produces a unique solution, and the iteration process continues until $\mathbf{F}(\bar{\mathcal{X}}_{\mathrm{i}}) < \epsilon$.

2.3 Low-Thrust Circular Restricted Three-Body Problem

The Circular Restricted Three-Body Problem (CR3BP) is a time-invariant system in which two primary bodies –modeled as point masses– are assumed to be in coplanar and circular orbits relative to their common barycenter, while a third body of negligible mass moves throughout the system [64]. Some common applications of the CR3BP model are the Earth-Moon-spacecraft system —the focus of this investigation—, the Sun-Earth-spacecraft system, that was the main focus of the previously flown NASA Genesis mission, as well as some planet-moon-spacecraft systems including, but not limited to, the Jupiter-Europa-spacecraft system, and the Saturn-Enceladus-spacecraft system.

The two primaries are labeled P_1 and P_2 with corresponding masses M_1 and M_2, respectively; by convention, P_1 is assumed to be the larger body ($M_1 > M_2$), while the third-body, P_3, is assumed to be the spacecraft. The ultimate goal of utilizing the CRTBP system is to derive the Equations of Motion (EOMs) that govern the path of the spacecraft under the gravitational attraction of the two primaries —the two attracting bodies—. The mass of third-body is assumed to be much smaller than those of P_1 and P_2, such that, $M_3 \ll M_1, M_2$.

Within the context of the CR3BP, a rotating coordinate frame, $\mathbf{R}$ is defined such that, the origin is the common barycenter of the P_1-P_2 system; moreover, this barycenter is an inertially-fixed point. The x-axis of the rotating frame is directed along the line from P_1 to P_2, the z-axis is aligned with the angular momentum of the primary system, and the y-axis completes the right-handed triad. Figure 2.2 is a graphical representation of the CR3BP. The right handed triad $(\hat{x}, \hat{y}, \hat{z})$ represents the rotating coordinate system, while $(\hat{X}, \hat{Y}, \hat{Z})$ corresponds to an inertially fixed frame, centered at the system barycenter.

The two primaries are assumed to move strictly in the xy-plane, while the spacecraft, P_3 is free to move anywhere in the three-dimensional space. The position vector for each of the bodies with respect to the barycenter of the system is represented by $\bar{R}_1$, $\bar{R}_2$ and $\bar{R}_3$ for P_1, P_2 and P_3, respectively. The vector from directed from P_1 to P_3 is labeled $\bar{R}_{13}$, and the vector from directed from P_2 to P_3 is labeled $\bar{R}_{23}$; these vectors are given by:

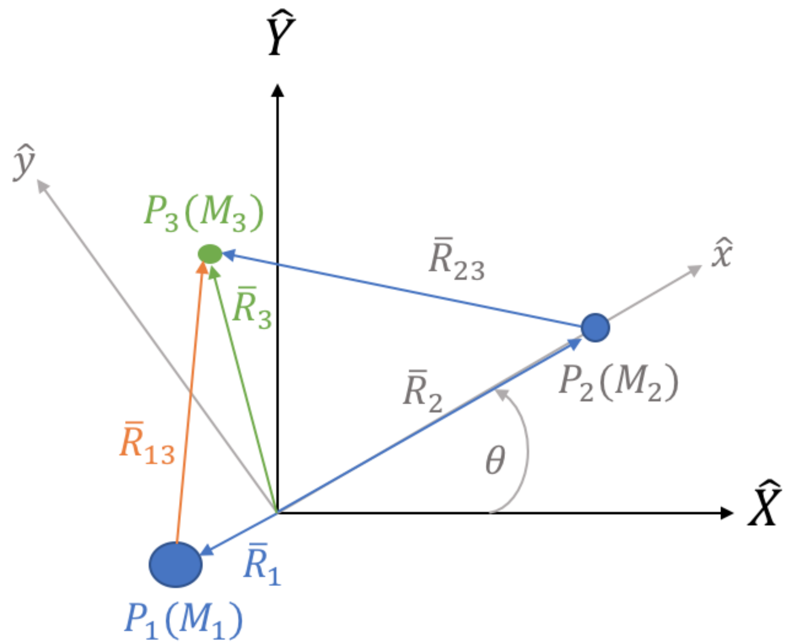

Figure 2.2. Graphical representation of the CRTBP.

$$\bar{R}_{13} = \bar{R}_1 - \bar{R}_3 \tag{2.31}$$

$$\bar{R}_{23} = \bar{R}_2 - \bar{R}_3 \tag{2.32}$$

the angle θ is directly related to the angular rate of rotation of the rotating frame, **R**, with respect to the inertial frame, **I**. Utilizing a Newtonian approach —Newton's second law— the equations of motions of the spacecraft, P_3, under this regime are determined by equating the kinematic expression of the acceleration vector as seen by an observer fixed in the inertial frame, to the net sum of gravitational forces acting on the body, such that, the equations of motion due to the gravitational attraction of the two primaries are:

$$M_3{}^{\mathbf{I}}\bar{R}_3'' = -\frac{\tilde{G}M_3M_1}{R_{13}^3}\bar{R}_{13} - \frac{\tilde{G}M_2M_1}{R_{12}^3}\bar{R}_{12} \tag{2.33}$$

where $\tilde{G}$ represents the universal gravitational constant, and the double prime upper script corresponds to the second derivative with respect to time.

To completely solve the problem in Equation 2.33, eighteen constants —integrals of motion— are necessary. However, only ten integrals of motion are known to date, suggesting that there is no analytical (or closed-form solution) to the CR3BP. The problem is then solved via numerical methods. Due to the nature of the natural motion of satellites in space, distance quantities are often times a couple of orders of magnitude larger than those related to velocity or time. When numerically solving for the motion of P_3 in Equation 2.33, the difference in the numerical values for each of the terms in the EOMs introduces numerical errors. Thus, a popular way to reduce the sensitivity of the EOMs to numerical errors is to non dimensionalize the equations of motion.

Using the standard characteristic quantities of distance, time and mass to appropriately non dimensionalize the system of equations, such that, the equations of motion are rewritten in terms of non dimensional time. Let the characteristic length, l^*, be defined as:

$$l^* = R_1 + R_2 \tag{2.34}$$

where R_1 and R_2 are the distances — magnitude of the position vector— of the two primaries from the system barycenter, respectively; moreover, all of the position vectors that appear in Figure 2.2 are non dimensionalized by the characteristic length as follows:

$$r_1 = \frac{R_1}{l^*} \tag{2.35}$$

$$r_2 = \frac{R_2}{l^*} \tag{2.36}$$

$$r_3 = \frac{R_3}{l^*} \tag{2.37}$$

$$r_{13} = \frac{R_{13}}{l^*} \tag{2.38}$$

$$r_{23} = \frac{R_{23}}{l^*} \tag{2.39}$$

Let us define as well the characteristic mass, m^*, as the sum of the masses of the two primaries:

$$m^* = M_1 + M_2 \tag{2.40}$$

The characteristic time, t^*, is constructed such that the non dimensional value of the universal gravitational constant, $\tilde{G}$, equals one:

$$t^* = \sqrt{\frac{l^{*3}}{\tilde{G}m^*}} \tag{2.41}$$

once the characteristic time is identified, the non-dimensional time is evaluated as follows:

$$t = \frac{\tilde{t}}{t^*} \tag{2.42}$$

Furthermore, recall that the rotating frame moves with respect to the inertial frame at an angular rate ${}^{\mathbf{I}}\omega^{\mathbf{R}} = \dot{\theta}\hat{z}$. One of the main assumptions of the CR3BP is that the rotating frame moves at the same angular rate at which the second primary, P_2, moves with respect to the larger primary, P_1. In the two-body problem, this rate is known as the mean motion, which is calculated as:

$$\dot{\tilde{\theta}} = \left(\frac{\tilde{G}m^*}{l^{*3}}\right) \tag{2.43}$$

Manipulating Equation 2.43, an expression for the non-dimensional mean motion of the rotating frame with respect to the inertially fixed frame is found by:

$$\dot{\theta} = \left(\frac{\tilde{G}m^*}{l^{*3}}\right)\left(\frac{l^{*3}}{\tilde{G}m^*}\right) = 1 \tag{2.44}$$

Lastly, a non dimensional mass ratio, μ, is defined, to help simplify the equations of motion in Equation 2.33 as follows:

$$\mu = \frac{M_2}{m^*} \tag{2.45}$$

The mass ratio is an important parameter of the CR3BP, and often times it is utilized to describe the sensitivity of the system. Table 2.1 presents a summary of some of the μ values encountered in the most popular CRTBP systems across our solar system.

Table 2.1. Summary of mass ratio parameters, μ, across multiple CR3BP in our solar system

CR3BP System	$\mu[nd]$
Earth-Moon	1.21×10^{-2}
Sun-Earth	3.04×10^{-6}
Sun-Jupiter	9.54×10^{-4}
Saturn-Titan	2.37×10^{-4}

The μ parameter is also utilized to redefine the non dimensional position vectors of the primary bodies and the spacecraft with respect to the system barycenter, B. The barycenter of the CR3BP system —the origin of the coordinate frame— corresponds to the location of the center of mass of the $P_1 - P_2$ system [65], such that:

$$B\hat{x} = \frac{-M_1 r_1 \hat{x} + M_2 r_2 \hat{x}}{m^*} = \bar{0} \tag{2.46}$$

from the definition of the non dimensional mass ratio, expressions for M_1 and M_2 are redefined as follows:

$$M_2 = \mu \left(M_1 + M_2\right) = \mu m^* \tag{2.47}$$

$$M_1 = \left(1 - \mu\right)\left(M_1 + M_2\right) = \left(1 - \mu\right) m^* \tag{2.48}$$

Such that, the system barycenter in terms of μ is given by

$$B\hat{x} = \left(1 - \mu\right) r_1 \hat{x} + \mu r_2 \hat{x} = 0 \tag{2.49}$$

Algebraic manipulation of Equation 2.49, yields the following expressions to represent the non dimensional position vectors of the primary bodies and the spacecraft, with respect to the system barycenter, in terms of the mass ratio parameter:

$$
\begin{aligned}
\bar{r}_1 &= -\mu\hat{x} && (2.50)\\
\bar{r}_2 &= (1-\mu)\,\hat{x} && (2.51)\\
\bar{r}_{13} &= (x+\mu)\,\hat{x} + y\hat{y} + z\hat{z} && (2.52)\\
\bar{r}_{23} &= (x-1+\mu)\,\hat{x} + y\hat{y} + z\hat{z} && (2.53)
\end{aligned}
$$

Rewriting the equations of motion of the spacecraft in Equation 2.33 in terms of the non dimensional quantities, yields the following non dimensional EOMs:

$$
{}^{\mathbf{I}}\ddot{\bar{r}}_3 = -\frac{(1-\mu)}{r_{13}^3}\bar{r}_{13} - \frac{\mu}{r_{12}^3}\bar{r}_{12} \tag{2.54}
$$

The left-hand side of Equation 2.54 is obtained by finding the kinematic expression for the non dimensional acceleration vector of the spacecraft. Let the position vector of P_3 written in terms of rotating coordinates be:

$$
\bar{r}_3 = x\hat{x} + y\hat{y} + z\hat{z} \tag{2.55}
$$

Apply the rule of the basic kinematic equation twice in Equation 2.55 to obtained the acceleration as seen by an inertial observer as follows:

$$
\begin{aligned}
{}^{\mathbf{I}}\dot{\bar{r}}_3 &= {}^{\mathbf{R}}\dot{\bar{r}}_3 + {}^{\mathbf{I}}\bar{\omega}^{\mathbf{R}} \times \bar{r}_3 && (2.56)\\
{}^{\mathbf{I}}\ddot{\bar{r}}_3 &= {}^{\mathbf{R}}\ddot{\bar{r}}_3 + 2\,{}^{\mathbf{I}}\bar{\omega}^{\mathbf{R}} \times {}^{\mathbf{R}}\dot{\bar{r}}_3 + {}^{\mathbf{I}}\bar{\omega}^{\mathbf{R}} \times {}^{\mathbf{I}}\bar{\omega}^{\mathbf{R}} \times \bar{r}_3 && (2.57)
\end{aligned}
$$

Written in terms of the components in rotating coordinates, the spacecraft kinematic acceleration vector is given by:

$$
{}^{\mathbf{I}}\ddot{\bar{r}}_3 = \left(\ddot{x} - 2\dot{\theta}\dot{y} - \dot{\theta}^2 x\right)\hat{x} + \left(\ddot{y} + 2\dot{\theta}\dot{x} - \dot{\theta}^2 y\right)\hat{y} + \ddot{z}\hat{z} \tag{2.58}
$$

Recall that the non dimensional mean motion of the system is equal to one. Thus, combining Equations 2.54 and 2.58, yields the set of non dimensional equations of motion in rotational component form given by:

$$\ddot{x} - 2\dot{y} - x = -\frac{(1-\mu)(x+\mu)}{r_{13}^3} - \frac{\mu(x-1+\mu)}{r_{23}^3} \tag{2.59}$$

$$\ddot{y} + 2\dot{x} - y = -\frac{(1-\mu)\,y}{r_{13}^3} - \frac{\mu y}{r_{23}^3} \tag{2.60}$$

$$\ddot{z} = -\frac{(1-\mu)\,z}{r_{13}^3} - \frac{\mu z}{r_{23}^3} \tag{2.61}$$

Equations 2.59-2.61 represent a system of second-order differential equations that dictate the motion of a spacecraft in any CR3BP model. To change the system, the mass parameter, μ, is modified. Table 2.2 offers a summary of the numerical values of the characteristic quantities utilized in the derivation of the Earth-Moon CR3BP system.

Table 2.2. Earth-Moon CR3BP system characteristic quantities

Quantity	**Numerical Value**
l^*	384747.99198 [km]
m^*	6.04604×10^{24} [kg]
t^*	375699.85904 [sec]
μ	0.01215 [nd]

To incorporate the low-thrust acceleration of the spacecraft into the equations of motion, three control input parameters are introduced: a scalar quantity to represent the thrust magnitude, and two angles to orient the thrust orientation vector as illustrated in Figure 2.3. The angle α orients the thrust vector in the $\hat{x}\hat{y}$-plane, while the angle β provides the out-of-plane component.

A pseudo-potential function, U_{LT}^*, in terms of the rotating non dimensional quantities is realized such that, all forces acting on the spacecraft, P_3, are derivable from such potential function as follows [12]:

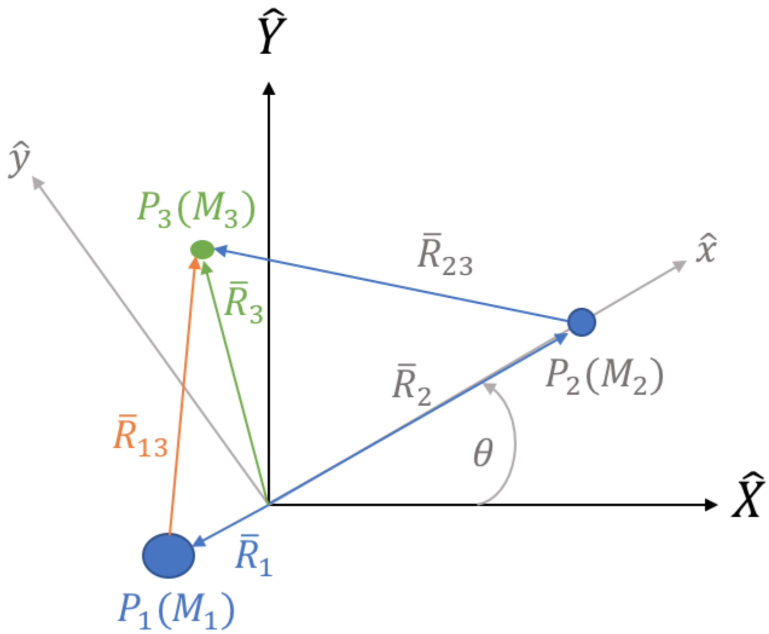

Figure 2.3. Graphical representation of the low-thrust augmented circular restricted three-body problem.

$$U_{LT}^{*} = \frac{1-\mu}{r_{13}} + \frac{\mu}{r_{23}} + \frac{1}{2}\left(x^2 + y^2\right) + \bar{r}_3 \cdot \bar{a}_T \tag{2.62}$$

where

$$\bar{a}_T = \frac{T}{m_3}\hat{a}_T \tag{2.63}$$

represents the non-dimensional thrust acceleration vector, and the unit vector $\hat{a}_T$ corresponds to the thrust direction —thrust orientation vector—. The term $\tilde{T}$ is the dimensional thrust magnitude, and the mass term, m, corresponds to the non dimensional mass of the spacecraft, that is evaluated as follows:

$$m = \frac{M_3}{M_{3,0}} \tag{2.64}$$

with $M_{3,0}$ representing the initial spacecraft mass. Utilizing the characteristic quantities of the CR3BP in Table 2.2, along with the non dimensional mass of the spacecraft, the non dimensional thrust magnitude, T, is given by:

$$T = \tilde{T}\frac{t^{*2}}{ml^{*}1000} \tag{2.65}$$

With the inclusion of the low-thrust acceleration term to the pseudo-potential function, the CR3BP model is augmented and referred to as the Low-Thrust Augmented Circular Restricted Three-Body Problem (CR3BP-LT) [66]. Furthermore, a new state variable is incorporated into the state vector of the second-order system of differential equations in Equation 2.54. This new added variable corresponds to the non dimensional mass of the spacecraft, m, and its rate of change with respect to the non dimensional time is evaluated as:

$$\dot{m} = -\frac{T^2}{2\mathcal{P}} \tag{2.66}$$

where $\mathcal{P}$ represents the engine power. Thus, the equations of motion that govern the dynamics of a low-thrust spacecraft under the circular restricted three-body problem regime are described as:

$$\ddot{x} - 2\dot{y} - x = -\frac{(1-\mu)(x+\mu)}{r_{13}^3} - \frac{\mu(x-1+\mu)}{r_{23}^3} + \frac{T}{m}\hat{a}_{T,x} \tag{2.67}$$

$$\ddot{y} + 2\dot{x} - y = -\frac{(1-\mu)\,y}{r_{13}^3} - \frac{\mu y}{r_{23}^3} + \frac{T}{m}\hat{a}_{T,y} \tag{2.68}$$

$$\ddot{z} = -\frac{(1-\mu)\,z}{r_{13}^3} - \frac{\mu z}{r_{23}^3} + \frac{T}{m}\hat{a}_{T,z} \tag{2.69}$$

where the rotating Cartesian components of the thrust acceleration unit vector, $\hat{a}_T$, in terms of the control orientation angles, α and β, are given by:

$$\hat{a}_{T,x} = \cos\alpha\cos\beta \tag{2.70}$$

$$\hat{a}_{T,y} = \sin\alpha\cos\beta \tag{2.71}$$

$$\hat{a}_{T,z} = \sin\beta \tag{2.72}$$

Since the mass of the spacecraft is not a constant numerical value —the total mass is continuously reduced monotonically when the thrusters are active—, Equations 2.67 - 2.69 can also be written in a more compact form, as a set of first-order differential equations as follows. Let $\bar{x}$ be the state vector composed of the position, $\bar{r}$, velocity, $\bar{v}$ and mass, m, state variables:

$$\bar{x} = \left\{ \begin{array}{c} \bar{r} \\ \bar{v} \\ m \end{array} \right\} \tag{2.73}$$

and let the nonlinear function $\bar{f}(\bar{r}, \bar{v})$ be:

$$\bar{f}(\bar{r}, \bar{v}, m) = \nabla U^*_{LT} - 2\hat{z} \times \bar{v} \tag{2.74}$$

such that:

$$\left\{ \begin{array}{c} \dot{\bar{r}} \\ \dot{\bar{v}} \\ \dot{m} \end{array} \right\} = \left\{ \begin{array}{c} \bar{v} \\ \bar{f}(\bar{r}, \bar{v}) \\ -\frac{T^2}{2\mathcal{P}} \end{array} \right\} \tag{2.75}$$

Moreover, if the specific impulse of the engine varies as time evolves, the mass rate of change with respect to time is denoted a Variable Specific Impulse model, or VSI. On the contrary, if the specific impulse remains fixed, the model is considered a Constant Specific Impulse engine, or CSI model. For the equations of motion described in Equations (2.75), a VSI model for the low-thrust spacecraft has been adopted for this investigation [67].

2.3.1 Libration Points

Within the context of the natural circular restricted three-body problem —without the augmented low-thrust acceleration term—, Lagrange discovered the existence of five unique equilibrium points, also called Lagrangian points or libration points. An equilibrium point, by definition, is a point in space for which all time derivatives are set to zero, i.e., points where the net sum of forces are cancelled. Therefore, to estimate the location of the five equilibrium points of the second order system of differential equations in Equations 2.59 - 2.61, with rotating coordinates $(x_{\text{eq}}, y_{\text{eq}}, z_{\text{eq}})$, set all time derivatives to zero as follows [68]:

$$0 - 2(0) - x_{\text{eq}} = -\frac{(1-\mu)(x_{\text{eq}}+\mu)}{r_{13}^3} - \frac{\mu(x_{\text{eq}}-1+\mu)}{r_{23}^3} \tag{2.76}$$

$$0 + 2(0) - y_{\text{eq}} = -\frac{(1-\mu)\,y_{\text{eq}}}{r_{13}^3} - \frac{\mu y}{r_{23}^3} \tag{2.77}$$

$$0 = -\frac{(1-\mu)\,z_{\text{eq}}}{r_{13}^3} - \frac{\mu z_{\text{eq}}}{r_{23}^3} \tag{2.78}$$

Solving Equations 2.76 - 2.78 for ($x_{\text{eq}}, y_{\text{eq}}$ and z_{eq}) in terms of μ, r_{13} and r_{23} yields the exact location of the five equilibrium points for this particular system. Note from Equation 2.78 that for the equality to be equal to zero, the out-of-plane coordinate z_{eq} must equal zero; thus, regardless of the CR3BP system being analyzed, i.e. regardless of the mass paramterer μ, all five equilibrium points exist only within the xy-plane. All five equilibrium points are planar. Furthermore, a possible solution from Equation 2.77 that makes the equality equal to zero is $y_{\text{eq}} = 0$. Thus, plugging for $y_{\text{eq}} = z_{\text{eq}} = 0$ in Equation 2.76 yields:

$$\bar{r}_{13} = (x_{\text{eq}}+\mu)\,\hat{x} + 0\hat{y} + 0\hat{z} \tag{2.79}$$

$$\bar{r}_{23} = (x_{\text{eq}}-1+\mu)\,\hat{x} + 0\hat{y} + 0\hat{z} \tag{2.80}$$

such that:

$$x_{\text{eq}} = -\frac{(1-\mu)(x_{\text{eq}}+\mu)}{(x_{\text{eq}}+\mu)^3} - \frac{\mu(x_{\text{eq}}-1+\mu)}{(x_{\text{eq}}-1+\mu)^3} \tag{2.81}$$

Equation 2.81 possesses three roots, which suggests that there exist three real equilibrium solutions that lie on the $\hat{x}$- axis. To solve for these points —also known as the collinear libration points—, a Newton's iterative method is formulated. The remaining two Lagrangian points are found by simultaneously solving for the system of equations formed by Equations 2.76 and 2.77. Table 2.3 shows the numerical value of the five equilibrium points for the Earth-Moon CR3BP dyamical model.

Table 2.3. Rotating coordinates of the five Lagrangian points in the CR3BP system

Libration Point	$x[km]$	$y[km]$
L_1	321710.2452	0
L_2	444244.1690	0
L_3	-386346.0751	0
L_4	187529.3293	332900.1652
L_5	187529.3293	-332900.1652

By convention, the three collinear libration points are termed L_1, L_2 and L_3, respectively. The two remaining libration points, those with a y-component different than zero, are referred to as the triangular points, L_4 and L_5. Figure 2.4 offers a graphical representation of the five equilibrium solutions in the Earth-Moon rotating coordinate frame.

2.3.2 Energy in the Circular Restricted Three-Body Problem

Even though there exists no closed-form solution to the circular restricted three-body problem, recall that the equations of motion that govern the dynamics of the spacecraft under this regime are derivable from a potential function, therefore, there exists one integral of the motion which is an energy-like quantity, also known as the Jacobi Constant (JC) [69]. The mathematical expression for the Jacobi constant is obtained by taking the dot product between the velocity and the acceleration vectors, and then integrating that result with respect to time, as follows :

$$^{\mathbf{R}}\ddot{\bar{r}}_3 \cdot {}^{\mathbf{R}}\dot{\bar{r}}_3 \;=\; \ddot{x}\dot{x} + \ddot{y}\dot{y} + \ddot{z}\dot{z} = \frac{1}{2}\left(\dot{x}^2 + \dot{y}^2 + \dot{z}^2\right) \tag{2.82}$$

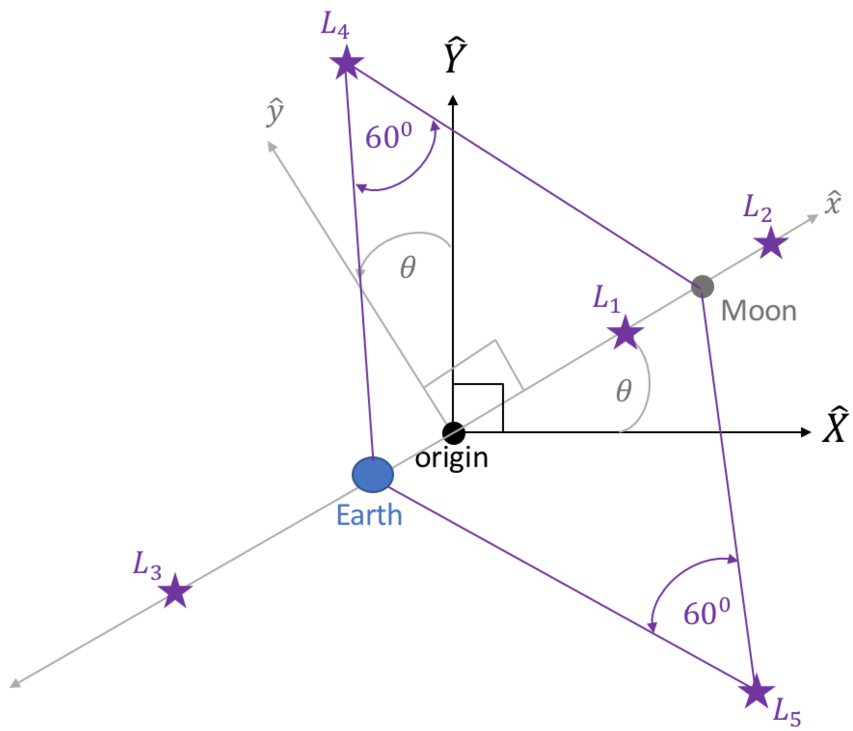

Figure 2.4. Graphical representation of the five Lagrangian points in the Earth-Moon CR3BP system

The potential pseudo-potential function for the natural circular restricted three-body problem is given by:

$$U^* = \frac{1-\mu}{r_{13}} + \frac{\mu}{r_{23}} + \frac{1}{2}\left(x^2 + y^2\right) \tag{2.83}$$

such that

$$\ddot{x} = \frac{\partial U^*}{\partial x} \tag{2.84}$$

$$\ddot{y} = \frac{\partial U^*}{\partial z} \tag{2.85}$$

$$\ddot{z} = \frac{\partial U^*}{\partial z} \tag{2.86}$$

$$\tag{2.87}$$

plugging these equalities back into Equation 2.88 yields:

$$
{}^{\mathbf{R}}\ddot{\bar{r}}_3 \cdot {}^{\mathbf{R}}\dot{\bar{r}}_3 = \ddot{x}\dot{x} + \ddot{y}\dot{y} + \ddot{z}\dot{z} = \frac{\partial U^*}{\partial x}\frac{dx}{dt} + \frac{\partial U^*}{\partial y}\frac{dy}{dt} + \frac{\partial U^*}{\partial z}\frac{dz}{dt} \tag{2.88}
$$

integrating both sides of the equation with respect to the non-dimensional time, t, produces the following equation:

$$
\begin{aligned}
\int \frac{1}{2}\left(\dot{x}^2 + \dot{y}^2 + \dot{z}^2\right) dt &= \int \left(\frac{\partial U^*}{\partial x}\frac{dx}{dt} + \frac{\partial U^*}{\partial y}\frac{dy}{dt} + \frac{\partial U^*}{\partial z}\frac{dz}{dt}\right) dt \\
\int \left(\frac{1}{2}\frac{dv}{dt}\right) dt &= \int \left(\frac{dU^*}{dt}\right) dt \\
\frac{1}{2}v^2 &= U^* + K
\end{aligned} \tag{2.89}
$$

where, v is the magnitude of the rotating velocity vector, and K is the constant of integration. Furthermore, solving for the constant K, and renaming it as the Jacobi constant of integration, JC, gives birth to this energy-like quantity that is the only known integral of motion within the context of the CR3BP:

$$
JC = 2U^* - v^2 \tag{2.90}
$$

In this investigation, the Jacobi constant is exploited as the main characteristic quantity describing ballistic arcs in the cislunar space. Every arc within the context of the CR3BP has an energy level associated with it; this energy level is described in terms of the Jacobi constant, and it is leveraged to determine the type of motion to be included within the orbit chaining framework for the construction of low-thrust spacecraft trajectory initial guesses.

In addition to spacecraft paths being associated with a particular energy level, the five equilibrium points of the system —the Lagrangian points— also have a corresponding Jacobi constant [70]. Table 2.4 shows the energy values for the five libration points within the context of the Earth-Moon CR3BP system. One of the many applications of the Jacobi constant in astrodynamics and trajectory design, is to identify regions of space in which the spacecraft is free to travel through, while obeying the laws of physics and the dynamics included in the assumptions of the derivation of the equations of motion.

Table 2.4. Energy value of the five Lagrangian points in the Earth-Moon CR3BP system

Libration Point	**Jacobi Constant**
L_1	321710.2452
L_2	444244.1690
L_3	-386346.0751
L_4	187529.3293
L_5	187529.3293

2.3.3 Continuation Strategies

Within the context of the unperturbed circular restricted three-body problem (CRTBP), if an appropriate perturbation is applied to the libration points —equilibrium points—, this perturbation generates a initial conditions that excites periodic motion in said equilibrium point vicinity. This perturbation can be given in the form of position and/or velocity errors. Periodic motion, in this context, refers to the property that if the state vector

$$\bar{x} = \left\{ \begin{array}{cccccc} x & y & z & \dot{x} & \dot{y} & \dot{z} \end{array} \right\}$$

is a solution satisfying the nonlinear equations of motion in Equation 2.75 in forward time, t, then by periodicity, the vector state

$$\bar{x} = \left\{ \begin{array}{cccccc} x & -y & z & -\dot{x} & \dot{y} & -\dot{z} \end{array} \right\}$$

also satisfies the equations of motion in reverse time, $-t$. Once a periodic solution in the CR3BP is identified, this orbit can be grown into a family of solutions —family of orbits— by following a numerical continuation strategy [71]. While there exist a variety of different continuation schemes, two are examined in this investigation.

Natural Parameter Continuation

A family of orbits, in its more basic definition, is referred to as a set of periodic orbits that share a set of natural characteristics that evolve continuously with each new member of the family. Some of these natural characteristics include continuity in the evolution of orbital period across all members of the family, a continuous evolution in energy —or Jacobi constant—, as well as a continuous evolution in the position and velocity components.

To grow a family from an individual periodic solution utilizing a natural parameter continuation scheme, the following steps are followed:

1. From the initial conditions of an already converged periodic orbit,

$$\bar{x}_{0,\mathrm{i}} = \left\{ \begin{array}{cccccc} x_{0,\mathrm{i}} & y_{0,\mathrm{i}} & z_{0,\mathrm{i}} & \dot{x}_{0,\mathrm{i}} & \dot{y}_{0,\mathrm{i}} & \dot{z}_{0,\mathrm{i}} \end{array} \right\}$$

with orbital period $\mathbb{P}_{0,\mathrm{i}}$, and Jacobi constant $C_{0,\mathrm{i}}$, select a quantity to utilize as the natural parameter to continue, e.g., select the $x-$ component of the position vector

2. Add a small perturbation to the specified natural parameter, and utilize this perturbed stated as the initial condition for a new member of the periodic orbits family

$$\bar{x}_{0,\mathrm{i+1}} = \left\{ \begin{array}{cccccc} x_{0,\mathrm{i}} + \delta x_{0,\mathrm{i}} & y_{0,\mathrm{i}} & z_{0,\mathrm{i}} & \dot{x}_{0,\mathrm{i}} & \dot{y}_{0,\mathrm{i}} & \dot{z}_{0,\mathrm{i}} \end{array} \right\}$$

3. Converge the new periodic solution utilizing a numerical method

The process is continued until a specified number of members in a family is achieved, or until the family reaches an end. By definition, a family of orbits reaches an ending condition when the evolution of the natural parameter no longer increases or decreases, but instead, reaches an asymptotic behaviour. Furthermore, the size of the perturbation, $\delta x_{0,\mathrm{i}}$, determines how close one orbit member is to the next. This value can be modified by the user, depending on the requirements of the family of orbits sought.

Pseudo-Arc Length Continuation

To grow a family from an individual periodic solution utilizing a pseudo-arc length continuation scheme, the problem is constructed by formulating an additional constraint vector in the numerical algorithm for converging the next periodic orbit.The additional constraint is given such that, a perturbation is applied to the initial conditions of the original orbit along the direction tangent to the family, as follows:

$$(\bar{x}_{0,\mathrm{i+1}} - \bar{x}_{0,\mathrm{i}})^T \sqcap (D\mathbf{F}_{0,\mathrm{i}}) - \mathcal{S} = 0 \tag{2.91}$$

where $\mathcal{S}$ corresponds to the step size, $\sqcap$ represents the null vector of the matrix of partial derivatives, $D\mathbf{F}_{0,\mathrm{i}}$, such that, the steps for converging the next periodic orbit member of the family are summarized as follows:

1. From the initial conditions of an already converged periodic orbit,

$$\bar{x}_{0,\mathrm{i}} = \left\{ \begin{array}{cccccc} x_{0,\mathrm{i}} & y_{0,\mathrm{i}} & z_{0,\mathrm{i}} & \dot{x}_{0,\mathrm{i}} & \dot{y}_{0,\mathrm{i}} & \dot{z}_{0,\mathrm{i}} \end{array} \right\}$$

   with orbital period $\mathbb{P}_{0,\mathrm{i}}$, and Jacobi constant $C_{0,\mathrm{i}}$, compute the null vector of the matrix of partial derivatives, $\sqcap(D\mathbf{F}_{0,\mathrm{i}})$

2. Add a small perturbation along the direction tangent to the family, and utilize this perturbed stated as the initial condition for a new member of the periodic orbits family

$$\bar{x}_{0,\mathrm{i+1}} = \bar{x}_{0,\mathrm{i}} + \mathcal{S}\sqcap(D\mathbf{F}_{0,\mathrm{i}})$$

3. Converge the new periodic solution utilizing a numerical method, by augmenting the vector of constraints, $\mathbf{F}_{0,\mathrm{i+1}}$, as follows:

$$\mathbf{G_{0,i+1}} = \left\{ \begin{array}{c} \mathbf{F_{0,i+1}} \\ (\bar{x}_{0,\mathrm{i+1}} - \bar{x}_{0,\mathrm{i}})^T \sqcap (D\mathbf{F}_{0,\mathrm{i}}) - \mathcal{S} = 0 \end{array} \right\}$$

where $\mathbf{G_{0,i+1}}$ is the augmented vector of constraints for the next orbit member of the family. Similar to the natural parameter continuation scheme, the process is continued until the family reaches an ending conditions, or until a specified number of periodic orbits is generated.

2.3.4 Libration Point Orbits (LPOs)

In addition to the libration points offering fundamental information regarding the points in space where the net sum of forces acting on the spacecraft vanishes, they also offer a valuable insight into the type of motion that the spacecraft undergoes while navigating the space under the circular restricted three-body problem regime [72]. This motion corresponds to periodic orbits that exist in the vicinity of the Lagrangian points, and are most commonly known as Libration Point Orbits (LPOs).

Throughout the years, many authors have discovered and extensively examined the existence of periodic orbits within the context of the circular restricted three-body problem, that have been crucial for the planning and execution of multiple missions flown to date. Some examples of periodic motion that exist in the Earth-Moon CR3BP system include, but are not limited to, Lyapunov orbits, halo orbits and vertical orbits, as well as some resonant orbits whose period is directly related to the period of the Moon around the Earth.

Once a periodic motion is identified, a continuation scheme can be utilized to determine a family of orbits. These families are typically described in terms of a continuously evolving parameter, such as, orbital period or Jacobi constant. The following figures illustrate a representation of some of the periodic families of orbits utilized in this investigation to construct initial guesses for the development of the orbit chaining framework. Figure 2.5 represents a family of Lyapunov orbits that evolves around the L_2 Lagrangian point in the Earth-Moon CR3BP. This family is planar —no out-of-plane components— and its excursion in energy level is represented as the color variable in the plot. The larger orbits present an excursion very close to the Moon, which makes the numerical computation sensitive when approaching this vicinity.

Figure 2.6 represents a family of Distant Retrograde Orbits (DROs) that evolves around the second primary P_2; since this family is computed within the context of the Earth-Moon CR3BP system, this particular DRO family evolves around the Moon [73]. The DRO family represented in this figure is a family of planar orbits —no out-of-plane components—, that exerts linearly stable characteristics. The larger the family is grown, the closer the motion gets to the Earth, P_1.

Figure 2.7 represents a family of Short Period Orbits (SPOs) that evolves around the Earth-Moon circular restricted three-body problem L_4 libration point. The L_4 SPO family is composed of individual planar orbits —no out-of-plane components—, that in its majority, exert linearly stable characteristics. The larger members of the family approach the Earth, P_1 on the L_3 libration point side, and offer large excursions of the xy-plane in this region

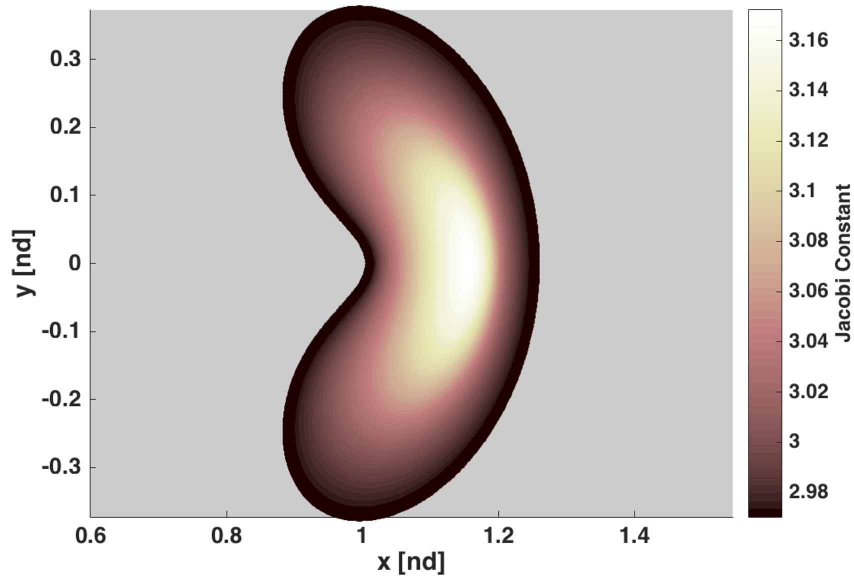

Figure 2.5. Family of L_2 Lyapunov orbits in the Earth-Moon CR3BP system

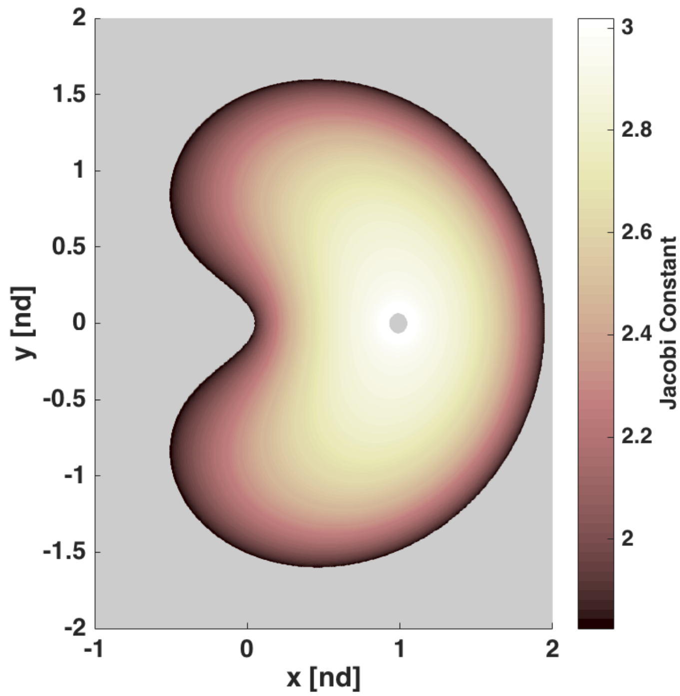

Figure 2.6. Family of P_2 DRO orbits in the Earth-Moon CR3BP system

of space. This family is characterized for its symmetry, and similarly, the same family is encountered in the vicinity of the L_5 libration point —the L_5 SPO family of orbits—, that present exactly the same characteristics in terms of large excursions in configuration space, as well its span in energy levels.

These families of orbits exist within the context of all other circular restricted three-body problem regimes, regardless of the mass parameter μ that characterized them. For instance, the commonly known trojan asteroids in the Jovian system, travel in periodic type motion around the L_4 and L_5 lagrangian points of the Sun-Jupiter CR3BP dynamical system.

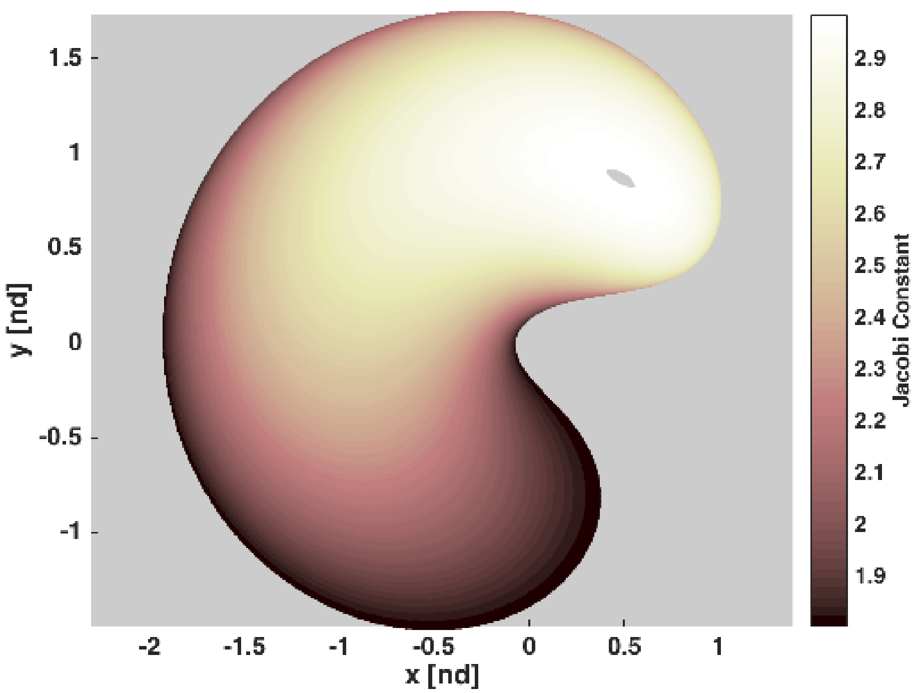

Figure 2.7. Family of L_4 SPO orbits in the Earth-Moon CR3BP system

Figure 2.8 represents two different family of orbits that evolve around the L_2 libration point: the L_2 Southern (S) halo family, and the L_2 Northern (N) halo family. Both of these families are composed of individual three-dimensional orbits. These orbits are considered unstable in the Lyapunov sense, as they offer flow that travels to and from the orbit naturally —ballistic arcs— and traverse large regions of space. This flow is derived from the theory of invariant manifolds. As the members of these families approach the Moon, P_2, they become more and more rectilinear, giving birth to a subset of orbits that belong to these families known as the L_2 southern and northern Near Rectilinear Halo Orbits (NRHO) [74].

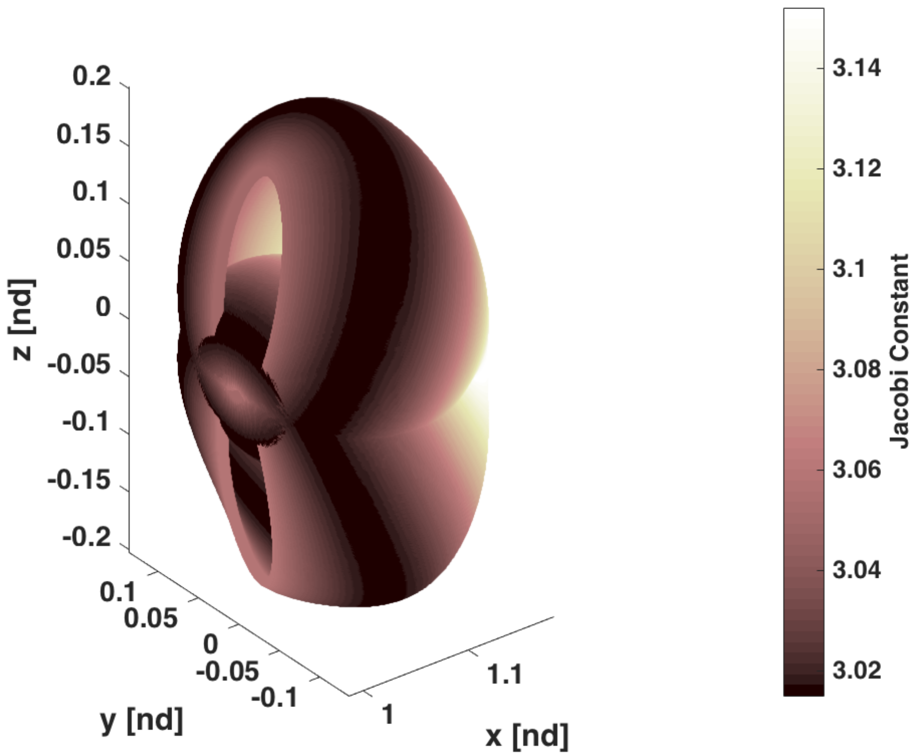

Figure 2.8. Family of Northern (N) and Southern (S) L_2 halo orbits in the Earth-Moon CR3BP system

Figure 2.9 represents a family of vertical orbits that evolves around the L_2 Lagrangian point in the Earth-Moon CR3BP system. This family is composed of individual linearly unstable individual three-dimensional orbits that, as they grow further away from the libration point, reach a point in space at which the larger orbits grown past the Earth and the Moon, i.e., they present excursions that navigate the entire Earth-Moon system, offering a wide variety of possibility for initial guess generation of spacecraft transfer scenarios. Moreover, the energy span of this family of orbits reaches the negative values, suggesting very close proximity with highly-sensitive dynamical regions in space.

Figure 2.10 corresponds to the family of axial orbits that evolves around the L_2 Lagrangian point within the context of the Earth-Moon circular restricted three-body problem.

The three-dimensional individual orbits members of this family are unstable in the Lyapunov sense, offering manifold arcs that freely approach and depart from the periodic orbit.

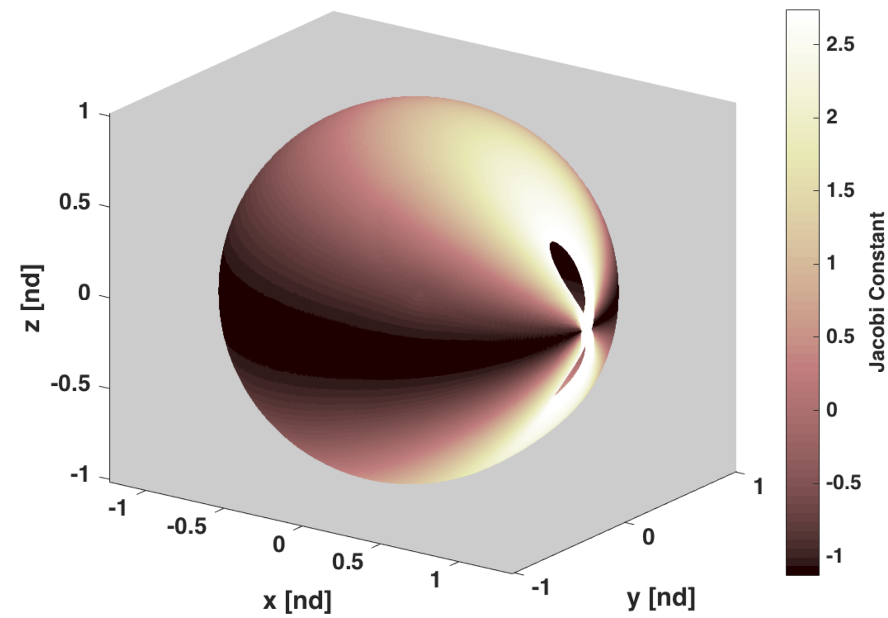

Figure 2.9. Family of L_2 vertical orbits in the Earth-Moon CR3BP system

The last sample family of periodic orbits presented in this section corresponds to a subset of the Earth-Moon $3:4$ resonant family illustrated in Figure 2.11. This family is considered an exterior-type resonant orbit, as its span in configuration —position— space, reaches well beyond the larger primary of the system, the Earth. Furthermore, even though the orbits are significantly large and thus, with large values of orbital periods, their energy levels remain well within a specific range and do not offer much variation. The energy characteristics of this family provides both benefits and drawbacks when utilizing members of this particular group for the construction of initial guesses in the orbit chaining framework.

In the case in which large exterior transfers are sought, this family offer a wide variety of suitable candidates for intermediate arcs in the generation of the initial guess estimate, as long as the energy level falls within the range of values needed to move the spacecraft around the space. Some transfer examples for low-thrust spacecraft travelling between LPOs

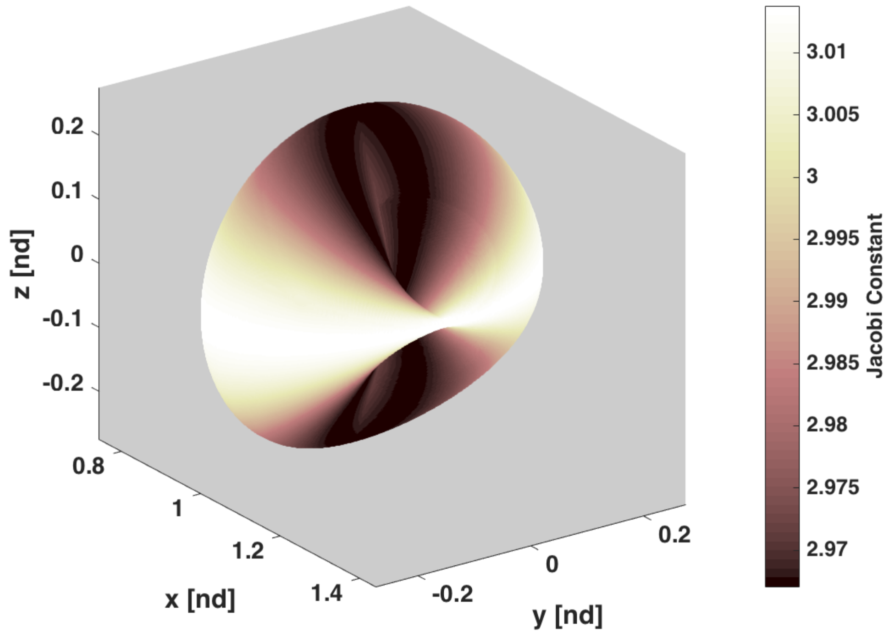

Figure 2.10. Family of L_2 axial orbits in the Earth-Moon CR3BP system

in the Earth-Moon CR3BP system that utilize this family of orbit for the construction of the initial guess, is presented later in the Applications section of this investigation.

2.4 Low-Thrust $\mathcal{N}$-Body Problem

To represent the motion of a low-thrust spacecraft, P_3, moving with respect to a primary body, P_q, in a time-dependent system, under perturbations from the gravitational influences of $\mathcal{N}$ additional nearby bodies, as represented in Figure 2.12, let $\tilde{T}$ represent the dimensional thrust acceleration magnitude, M correspond to the dimensional mass of the spacecraft, M_{j} ($\mathrm{j} = 1, , n$) be the dimensional mass of each additional perturbing body, and $\tilde{G}$ be the dimensional gravitational constant. The spacecraft's acceleration vector expressed in a J2000 inertial reference coordinate frame, centered on the primary body, is given by:

$$\ddot{\bar{R}}_{q3} = -\frac{\tilde{G}M_q}{R_{q3}^3}\bar{R}_{q3}^3 + \tilde{G}\sum_{\mathrm{j}=1,\mathrm{j}\neq q,3}^{\mathcal{N}} M_{\mathrm{j}}\left(\frac{\bar{R}_{3\mathrm{j}}}{R_{3\mathrm{j}}^3} - \frac{\bar{R}_{q\mathrm{j}}}{R_{q\mathrm{j}}^3}\right) + \frac{\tilde{T}}{M}\hat{a}_T \tag{2.92}$$

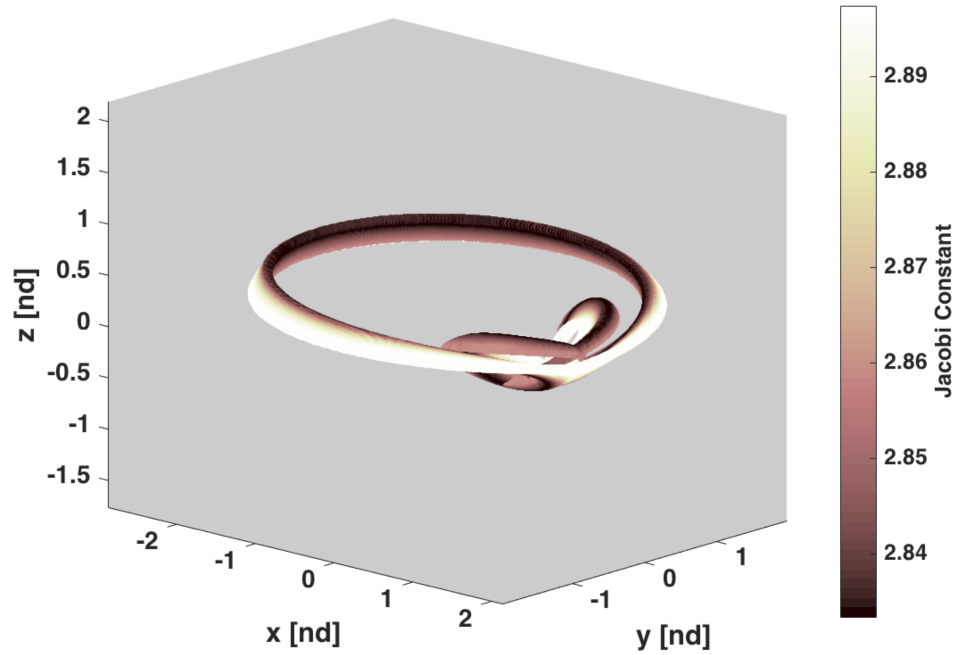

Figure 2.11. Family of 3 : 4 resonant orbits in the Earth-Moon CR3BP system

where the unit vector $\hat{a}_T$ represents the thrust orientation vector, the vector $\bar{R}_{q3}$ corresponds to the inertial dimensional position vector from the primary body to the spacecraft, the vector $\bar{R}_{q\mathrm{j}}$ is the dimensional position vector from each perturbing body to the primary body in inertial coordinates, and the vector $\bar{R}_{3\mathrm{j}}$ corresponds to the dimensional inertial position vector from the spacecraft to each of the perturbing bodies.

Equation 2.92 is derived in dimensional inertial coordinates following a Newtonian approach, as follows: the inertial position vector from the central body, P_q, to the spacecraft, P_3, is given by:

$$\bar{R}_{q3} = \bar{R}_3 - \bar{R}_q \tag{2.93}$$

Since these position vectors are all expressed in terms of inertial cartesian components, the time derivative with respect to an inertial frame are straightforward —there is no need to utilized the basic kinematic equation— hence, the inertial position and velocity of the spacecraft with respect to the central body are:

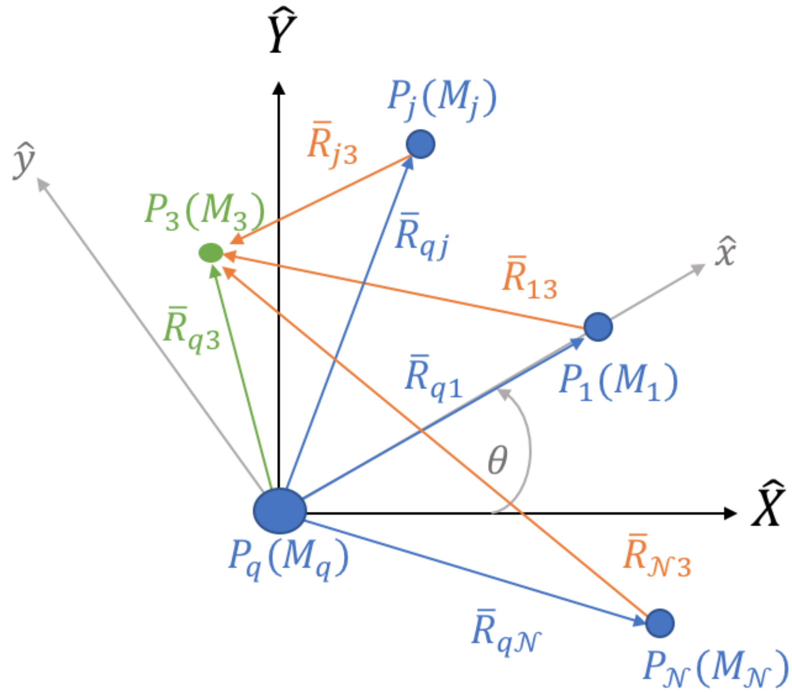

Figure 2.12. Graphical representation of the N-body problem. Particle P_{j} under the gravitational influence of $\mathcal{N}-1$ attracting bodies

$$
\begin{aligned}
{}^{\mathbf{I}}\dot{\bar{R}}_{q3} &= {}^{\mathbf{I}}\dot{\bar{R}}_3 - {}^{\mathbf{I}}\dot{\bar{R}}_q && (2.94)\\
{}^{\mathbf{I}}\ddot{\bar{R}}_{q3} &= {}^{\mathbf{I}}\ddot{\bar{R}}_3 - {}^{\mathbf{I}}\ddot{\bar{R}}_q && (2.95)
\end{aligned}
$$

Applying Newton's second law of gravity, the individual inertial acceleration terms in Equations 2.94 and 2.95 are expressed as:

$$
\begin{aligned}
M_q{}^{\mathbf{I}}\ddot{\bar{R}}_q &= -\tilde{G}\sum_{\mathrm{j}=1,\mathrm{j}\neq q}^{\mathcal{N}} \frac{M_q M_{\mathrm{j}}}{R_{\mathrm{j}q}^3}\bar{R}_{\mathrm{j}q} && (2.96)\\
M_3{}^{\mathbf{I}}\ddot{\bar{R}}_3 &= -\tilde{G}\sum_{\mathrm{j}=1,\mathrm{j}\neq 3}^{\mathcal{N}} \frac{M_3 M_{\mathrm{j}}}{R_{\mathrm{j}3}^3}\bar{R}_{\mathrm{j}3} && (2.97)
\end{aligned}
$$

Substituting Equations 2.96 and 2.97 into Equation 2.95, yields:

$$^{\mathbf{I}}\ddot{\bar{R}}_{q3} = -\frac{\tilde{G}}{M_3}\sum_{\mathrm{j}=1,\mathrm{j}\neq q}^{\mathcal{N}}\frac{M_3 M_\mathrm{j}}{R_{\mathrm{j}q}^3}\bar{R}_{\mathrm{j}q} + \frac{\tilde{G}}{M_3}\sum_{\mathrm{j}=1,\mathrm{j}\neq 3}^{\mathcal{N}}\frac{M_3 M_\mathrm{j}}{R_{\mathrm{j}3}^3}\bar{R}_{\mathrm{j}3} \tag{2.98}$$

Simplifying the mass of the spacecraft, M_3, from the above equation, and reversing the orientation of the inertial position vectors of the spacecraft with respect to the primary —perturbing— bodies yields:

$$^{\mathbf{I}}\ddot{\bar{R}}_{q3} = \tilde{G}\sum_{\mathrm{j}=1,\mathrm{j}\neq 3}^{\mathcal{N}}\frac{M_\mathrm{j}}{R_{3\mathrm{j}}^3}\bar{R}_{3\mathrm{j}} - \tilde{G}\sum_{\mathrm{j}=1,\mathrm{j}\neq q}^{\mathcal{N}}\frac{M_\mathrm{j}}{R_{q\mathrm{j}}^3}\bar{R}_{q\mathrm{j}} \tag{2.99}$$

Finally, to arrive at Equation 2.92, isolate the $\mathrm{j} = 3$ term from the second term in Equation 2.99, and combine the two summations into one.

The acceleration term introduced by the low-thrust engine to the equations of motion, is valid independently of the engine model assumed, i.e., it is valid for both the Constant Specific Impulse (CSI) engine model, as well as the Variable Specific Impulse (VSI) regime. Furthermore, the relationship between the engine specific impulse, I_{sp}, and the magnitude of the thrust force is given by:

$$\tilde{T} = \frac{2\mathcal{P}}{I_{sp}g_0} \tag{2.100}$$

where g_0 is the dimensional reference gravitational acceleration constant for the system of interest. Furthermore, in a CSI regime, in which the power of the engine is assumed to be constant, the control authority on the trust acceleration magnitude is restricted to a turn-and-hold type of regime, such that:

$$\tilde{T} = \begin{cases} \text{engine on, } \tilde{T} = \tilde{T}_{max} \\ \text{engine off, } \tilde{T} = 0 \end{cases}$$

and, the mass flow rate of the spacecraft is computed analytically as:

$$\dot{m} = -\frac{\tilde{T}}{I_{sp}g_0} \tag{2.101}$$

note that, the equation for the mass rate of flow under the CSI regime possesses an analytical solution, whereas, in a VSI regime, the mass flow rate of the spacecraft must be integrated as part of the state vector to obtain its time history.

Lastly, recall that the J2000 coordinate frame is an Earth-centered inertial reference frame where all directions are recorded on January 1st, 2000 at 12:00:00 Ephemeris Time (ET) (Julian Date: 2451545.0 ET) [75], in which the x-axis is directed along the vernal equinox, the z-axis is parallel to the Earth spin axis direction, and the y-axis completes the right-handed triad. The relative position quantities in Equation 2.92 associated with the gravitational bodies, are accessed via SPICE toolkits [76], and are computed from the NASA's Jet Propulsion Laboratory DE421 ephemerides data.

In this investigation, the solutions computed in the J2000 inertial reference frame are transformed into alternate frames inertial and rotating in the ephemeris models for further analysis. For instance employing the Moon as the central body in the inertial frame is of great advantage when visualizing trjectories between libration point orbits in the cislunar region. There exist multiple approaches for transforming trajectories from a primary body centered inertial frame to a barycentered rotating frame some of which are presented in the work by Pavlak [77] and Stuart [78].

3. LOW-THRUST SPACECRAFT OPTIMIZATION TECHNIQUES

With the thrust acceleration of the spacecraft being the main control variable for a low-thrust vehicle in the CR3BP-LT regime, an informed guess for the control history becomes crucial to determining a continuous solution to the equations of motion. Furthermore, this solution is expected to satisfy certain constraints along the path, while minimizing a predetermined performance function that supports the mission application requirements. To identify a suitable control history for the thrust acceleration terms, optimal control theory is employed, and both direct and indirect methods are explored to minimize the propellant consumption of the spacecraft, along with the time-of-flight of the trajectories.

3.1 An Overview of Optimal Control Theory

Within the context of optimal control theory, the optimal control problem determines of a set of control, also referred to as design variables, that extremize an objective function. In the low-thrust spacecraft trajectory design problem a thrust orientation vector must be specified at each instant of time to minimize a cost, commonly represented in terms of propellant consumption or time-of-flight (ToF). Many authors, such as, Betts [79], [80], Conway [81], Rao [82], and Topputo and Zhang [83] have devoted significant effort to solve this optimization problem. Optimal control was born in 1697 in Groningen, Netherlands when Johann Bernoulli published his solution of "Brachystochrone Problem". The "Brachystochrone Problem" is illustrated in Figure 3.1, and its main goal is to answer the following question: find a trajectory which is traveled in the shortest time.

This problem was solved by Johann Bernoulli, Jacob Bernoulli, Newton, Leibnitz, Tschirnhaus, and L'hospital, and it was expected to be solved by Huygens who died in 1695. The solution is the well-known cycloid. Before this problem was posed and solved, the shortest path joining two points was a straight line. Later, the Isoperimetric Problem (Dido's problem) arose, whose goal was to find the plane curve of a given length that encloses the largest possible area. Hero (or Heron) of Alexandria published that a light ray emitted by an object travels a path which is shortest —fastest—, while Fermat (1601-1665) predicted that light rays follow the fastest (i.e. minimum time) paths. Later, in 1685, Newton worked on the determination of the shape of a body with minimum drag, which gave birth to the Calculus of Variations (CoV) [84].

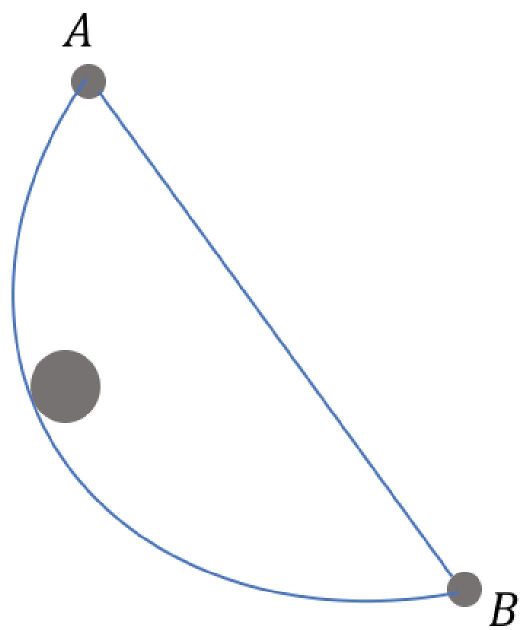

Figure 3.1. The Brachystochrone Problem: the birth of the optimal control theory

In 1744, Euler, a student of Johann Bernoulli at University of Basel at the age of 13 published his thesis: "The method of finding plane curves that show some property of maximum and minimum". Around the same time Lagrange became interested in variational problems after reading Euler's works and wrote a letter to Euler in 1755 at the age of 19, from these interactions they developed the stationary condition for maximum or minimum —also known as the Euler-Lagrange Equation—.

$$S(q(t)) = \int_a^b \mathcal{L}(q, \dot{q}, t)dt \tag{3.1}$$

where S represents an arbitrary cost function, and q corresponds to an arbitrary state variable. Furthermore, $\mathcal{L}$ is the energy function given by:

$$\mathcal{L}(q,\dot{q},t) = \text{kinetic energy - potential energy}$$

such that, the Euler-Lagrange necessary condition for maximum or minimum is given by:

$$\frac{d}{dt}\frac{\partial \mathcal{L}}{\partial \dot{q}} - \frac{\partial \mathcal{L}}{\partial q} = 0 \tag{3.2}$$

Later on, Legendre (1752-1833) developed an additional necessary condition for a minimum, that states:

$$\frac{\partial^2 \mathcal{L}}{\partial \dot{q}^2} > 0 \tag{3.3}$$

In the 1800s, Hamilton posed the following question: is it possible that both can be expressed necessary conditions for a minimum of one and the same function? The answer to this questions gave birth tho well-known Hamiltonian function, $\mathcal{H}$, given by:

$$\mathcal{H}(x,u,p,t) = p^T f(x,u,t) - \mathcal{L}(x,u,t) \tag{3.4}$$

where x represents an arbitrary state variable, u corresponds to an arbitrary control variable, and p is an arbitrary optimization parameter, also known as co-states or lagrange multipliers. Moreover, Hamilton redefined the optimal control problem as:

$$\begin{aligned} min\mathcal{J} \quad &= \quad \int_a^b \mathcal{L}(x,u,t)dt \\ \text{subject to} \quad & \quad \dot{x} = f(x,u,t) \\ & \quad x(a) = x_a \\ & \quad x(b) = x_b \end{aligned} \tag{3.5}$$

where x_a and x_b represent the initial and final condition on the state variable, respectively. The necessary conditions for a minimum as proposed by Hamilton are given by:

$$\frac{dx}{dt} = \frac{\partial \mathcal{H}}{\partial p} \tag{3.6}$$

$$\frac{dp}{dt} = -\frac{\partial \mathcal{H}}{\partial x} \tag{3.7}$$

$$\frac{\partial \mathcal{H}}{\partial u} = 0 \tag{3.8}$$

In the 1900s, Pontryagin introduced his maximum principle:

$$\mathcal{H}(x^*, u^*, p^*, t) \geq \mathcal{H}(x, u, p, t) \tag{3.9}$$

that is the most general necessary conditions for a maximum. Furthermore, it is true for all admissible control values where the symbol $*$ denotes optimal values. This principle works for a system with inequality constraints on the states and/or the control variables. There exist different optimization methods to determine a solution once the optimal control problem is formulated. These methods are divided into two categories: indirect and direct approaches. Indirect methods apply the Euler-Lagrange theorem to the continuous optimal control problem to transform it into a Two-Point Boundary Value Problem, TPBVP; while direct methods extremize the cost function directly [85].

The main differences between the two categories of optimization problems is that direct methods are first discretized into sub problems, and then the optimal control problem is transformed into a Nonlinear Programming Problem, NLP. On the contrary, indirect optimization methods first optimize by means of the Euler-Lagrange theory to generate a TPBVP, after which the problem is discretized and solved.

3.2 Indirect Optimization Methods

Indirect optimization methods rely on the calculus of variations, also referred to as the Euler-Lagrange theory, that was develop in the 1700s by mathematicians Euler and Lagrange. The main idea of this approach is to transform the general optimal control problem into a parameter optimization problem, in which a Two-Point Boundary Value Problem (TPBVP) is solved. To formulate the optimal control problem as a well-defined two point boundary value problem, its solution is sought via the introduction of adjoint states —also termed co-states or Lagrange multipliers — as follows [60], [61].

To illustrate the implementation of the Euler-Lagrange theory, let the first order system of equations given by $\dot{x}$, represent the nonlinear equations of motion that describe the path of a state variable, x, such that:

$$\dot{x}(t) = f\left(x(t), u(t), w(t), p(t), t\right) \tag{3.10}$$

where $f \in \mathbb{R}^n$ represents a nonlinear function describing the dynamical environment. $u(t) \in \mathbb{R}^m$ is the input or control variable, $w \in \mathbb{R}^s$ are the disturbance inputs, and $p(t) \in \mathbb{R}^l$ correspond to the optimization parameters. Furthermore, if the are no disturbances, and all the parameters are known, Equation 3.10 reduces to:

$$\dot{x}(t) = f\left(x(t), u(t), t\right) \tag{3.11}$$

The Euler-Lagrange indirect optimization problem consists of finding a history of the control input $u(t)$ for $t_0 \leq t \leq t_f$ which drives the state from its initial value to its final value and at the same time minimizes (or maximizes) a cost function. The cost function —also referred to as the objective function— can be given in one of three forms:

- **Mayer problem:**
$$\mathcal{J} = \check{\phi}\left(x(t_f), t_f\right) \tag{3.12}$$

- **Lagrange Problem**
$$\mathcal{J} = \int_{t_0}^{t_f} \{\mathcal{L}\left(x(t), u(t), t\right)\} dt \tag{3.13}$$

- **Bolza Problem**
$$\mathcal{J} = \check{\phi}\left(x(t_f), t_f\right) + \int_{t_0}^{t_f} \{\mathcal{L}\left(x(t), u(t), t\right)\} dt \tag{3.14}$$

where the function in the integrand corresponds to the path constraints and the scalar function $\mathcal{L}$ is known as the Lagrangian function. Moreover, any optimal control problem can be expressed in the form of an unconstrained problem, one that seeks to find the control history without satisfying any extra constraints on the states variables or the control variables;

or a constrained minimization problem, one that is subject to equality and/or inequality constraints either on the states or on the control variables.

When a constrained minimization problem is approached, the best way to solve these types of problems is by adjoining —adding— the equality constraints to the cost —objective— function, by means of a vector of Lagrange multiplier, $\bar{\lambda} \in \mathbb{R}^n$, that is also referred to as the vector of co-states. These co-states augment then the objective function, such that, a larger number of equations must now be solved. Some of the most common objective functions for the spacecraft trajectory design problem are:

- **Minimum-time problem:**

$$\mathcal{J} = \int_{t_0}^{t_f} \{1\} dt = t_f - t_0 \tag{3.15}$$

- **Minimum-fuel Problem**

$$\mathcal{J} = \int_{t_0}^{t_f} \{\dot{m}\} dt = m(t_f) - m(t_0) \tag{3.16}$$

  where $\dot{m}$ is the mass flow rate of the fuel.

Assume that is desired to minimize a cost function of the Bolza problem type, where the state variables are subject to the differential equations in Equation 3.11, and to the boundary conditions $x(t_0) = x_0$ and $x(t_f) = x_f$. Furthemore, let $\mathcal{J}$ be a differentiable functional of x; if x^* is an extrema, then if follows that:

$$\delta\mathcal{J}(x^*, \delta x) = 0 \text{ for all admissible } \delta x$$

By utilizing Lagrange multipliers, the constrained Bolza problem is transformed into an unconstrained with an augmented cost function, as follows:

$$\mathcal{J}_a = \check{\phi}\left(x(t_f), t_f\right) + \int_{t_0}^{t_f} \left\{\mathcal{L}\left(x(t), u(t), t\right) + \lambda^T(t)\left[f\left(x(t), u(t), t\right) - \dot{x}\right]\right\} dt \tag{3.17}$$

Next, a Hamiltonian function is realized, such that:

$$\mathcal{H}\left(x(t), u(t), \lambda(t), t\right) = \mathcal{L}\left(x(t), u(t), t\right) + \lambda^T(t) f\left(x(t), u(t), t\right) \tag{3.18}$$

and the augmented cost function is rewritten as:

$$\mathcal{J}_a = \check{\phi}\left(x(t_f), t_f\right) + \int_{t_0}^{t_f} \{\mathcal{H}\left(x(t), u(t), t\right)\} dt - \int_{t_0}^{t_f} \{\lambda^T(t)\dot{x}\} dt \tag{3.19}$$

using integration by parts on the augmented cost function yields:

$$\mathcal{J}_a = \check{\phi}\left(x(t_f), t_f\right) + \left(\lambda^T(t_0)x(t_0) - \lambda^T(t_f)x(t_f)\right) + \int_{t_0}^{t_f} \{\mathcal{H}\left(x(t), u(t), t\right) + \dot{\lambda}^T(t)x(t)\} dt \tag{3.20}$$

to identify the necessary conditions for optimality, the variations on the augmented cost function are assessed as follows:

$$\begin{aligned} \Delta\mathcal{J}_a(x, u, , t) &= \mathcal{J}_a(x + \delta x, u + \delta u, , t) - \mathcal{J}_a(x, u, , t) && (3.21) \\ &= \delta\mathcal{J}_a + H.O.T && (3.22) \end{aligned}$$

Utilizing calculus of variations, and assuming that the final time, t_f, is fixed, the variations are expanded such that:

$$\begin{aligned} \delta\mathcal{J}_a &= \left[\left(\frac{\partial\check{\phi}}{\partial x} - \lambda^T(t_f)\right)\delta x\right]_{t_f} + \left[\lambda^T(t)\delta x\right]_{t_0} + \int_{t_0}^{t_f} \left(\frac{\partial\mathcal{H}}{\partial u}\delta u + \left[\frac{\partial\mathcal{H}}{\partial x} + \dot{\lambda}^T\right]\delta x\right) dt && (3.23) \\ &= \delta\mathcal{J}(t_f) + \delta\mathcal{J}(t_0) + \delta\mathcal{J}(t_0, t_f) && (3.24) \end{aligned}$$

the necessary conditions for optimality are obtained by setting $\delta\mathcal{J}_a = 0$, yielding:

$$\dot{\lambda}^T = -\frac{\partial \mathcal{H}}{\partial x} \tag{3.25}$$

$$\text{with } \lambda^T(t_f) = \frac{\partial \check{\phi}}{\partial x} \tag{3.26}$$

$$0 = \frac{\partial \mathcal{H}}{\partial u} \tag{3.27}$$

Note that these optimality equations form a two-point boundary value problem, for which the value of the Lagrange multipliers at the final time is required. To solve for this equations, a backwards propagation in time is necessary, for which the principle of Dynamic Programming (DP) is utilized —discussed in Section 3.4.1—. The set of equations in Equations 3.25-3.27 are the well-known Euler-Lagrange equations for optimality.

In addition to the necessary conditions for optimality, there exists a set of sufficient conditions for optimality that are required to be met in order for the optimal solution to be considered a minimum, as follows:

- **Legendre-Clebsch (or comvexity) condition:**

$$\frac{\partial^2 \mathcal{H}}{\partial u^2}\left(x^*, u^*, \lambda^*, t\right) = \mathcal{H}_{uu} > 0 \text{ for } t \in [t_0, t_f] \tag{3.28}$$

- **Conjugate point:** these are points where minimizing trajectories are intersected (or joined) together. Furthermore, If there are no conjugate points on the optimal path, the locally optimal trajectory is unique.

Moreover, if terminal constraints are added to either the state or the control variables in the original formulation of the optimal control problem, let a function $\Phi\left(\bar{x}, \bar{u}, t\right)$ be utilized to incorporate the initial and final constraints, such that:

$$\check{\Phi}\left(x, u, t\right) = \check{\phi} + \nu^T \psi \tag{3.29}$$

with $\check{\psi}$ representing the equality constraints on the initial and final conditions on the state variables, $\check{\phi}$ corresponds to the terminal constraints and $\bar{\nu}$ is the vector of Lagrange multipliers to adjoint the boundary constraints.

Once all necessary and sufficient conditions are determined for the optimal control problem, the minimum (maximum) principle for the optimal control problem, introduced by Pontryagm, is stated such that:

$$\mathcal{H}\left(x^*(t), u(t), \lambda(t), t\right) \geq \mathcal{H}\left(x^*(t), u^*(t), \lambda(t), t\right) \tag{3.30}$$

for all t and $u \in U$, where u^* is the control input that minimizes the Hamiltonian function $\mathcal{H}$.

Consider the case of finding an optimal path for a low-thrust spacecraft travelling in the vicinity of Moon, within the context of the circular restricted three-body problem. The optimal control problem is formulated such that it is desired to minimize the performance function, J, as:

$$\min J = -\frac{1}{2} W_1 \left(1 - m_f\right)^2 + W_2 ToF \tag{3.31}$$

The cost function in Equation 3.31 is comprised of two different terms, one concerned with the minimization of the propellant consumption of the spacecraft,$-\frac{1}{2} W_1 \left(1 - m_f\right)^2$, and the second one, introduced to minimize for the time-of-flight —or duration– of the trajectory, $W_2 ToF$. Furthermore, to highlight the priority of each of the terms in the objective function, scalar weights W_1 and W_2 are introduced.

The goal of the optimal control problem is to minimize the performance function subject to the nonlinear differential equations of motion described in Equation (2.75), and with a set of prescribed initial and final conditions for the state vector, $\bar{x}(t_0) = \bar{x}_0$ and $\bar{x}(t_f) = \bar{x}_f$, such that:

$$\psi_0 = \left\{ \begin{array}{c} \bar{r}_0 - \bar{r}_{\mathrm{i}} \\ \bar{v}_0 - \bar{v}_{\mathrm{i}} \\ m_0 - 1 \end{array} \right\} = \bar{0} \tag{3.32}$$

$$\psi_f = \begin{Bmatrix} \bar{r}_f - \bar{r}_f \\ \bar{v}_f - \bar{v}_f \end{Bmatrix} = \bar{0} \tag{3.33}$$

with the subscripts i and f signifying initial and final conditions, respectively. Furthermore, a constraint exists as well on the thrust orientation vector, such that it is always of magnitude equal to one, as follows:

$$\hat{a}_T^T \hat{a}_T - 1 = 0 \tag{3.34}$$

Following the Euler-Lagrange theory, a set of Lagrange multipliers, $\bar{\lambda}$ and $\bar{\nu}$, are introduced to augment the cost function, such that the dynamics of the system, and the terminal constraints, are adjoined to the performance function, as follows:

$$\min J = -\frac{1}{2} W_1 \left(1 - m_f\right)^2 + W_2 ToF + \bar{\nu}_0^T \psi_0 + \bar{\nu}_f^T \psi_f + \int_{t_0}^{t_f} \left\{ H - \bar{\lambda}^T \dot{\bar{x}} \right\} dt \tag{3.35}$$

Recall that the state vector for the low-thrust spacecraft trajectory design problem within the context of the CR3BP-LT, in terms of non dimensional rotating coordinates is given by:

$$\bar{x} = \begin{Bmatrix} \bar{r} \\ \bar{v} \\ m \end{Bmatrix} \tag{3.36}$$

Therefore, the Lagrange multipliers that adjoin the equations of motion corresponding to this state vector are written as:

$$\bar{\lambda} = \begin{Bmatrix} \bar{\lambda}_r \\ \bar{\lambda}_v \\ \lambda_m \end{Bmatrix} \tag{3.37}$$

Moreover, note that the performance function in Equation 3.31 is of the Mayer problem type, i.e. the Lagrangian function, L, equals zero; thus, the Hamiltonian function for this low-thrust spacecraft optimal control problem is formed as follows:

$$
\begin{aligned}
H &= L + \bar{\lambda}^T \dot{\bar{x}} \\
&= \bar{\lambda}_r^T \bar{v} + \bar{\lambda}_v^T \left[\bar{f}(\bar{r}, \bar{v}) + \frac{T}{m} \hat{a}_T \right] - \lambda_m^T \frac{T^2}{2\mathcal{P}}
\end{aligned} \tag{3.38}
$$

where $\bar{\lambda}_r^T$, $\bar{\lambda}_v^T$, and $\bar{\lambda}_m^T$ correspond to the position, velocity and mass co-states, respectively. Applying the necessary and sufficient conditions for optimality to the first-order derivatives of Equation (3.38), the following equalities are true:

$$
\begin{aligned}
\dot{\bar{\lambda}}^T &= -\frac{\partial H}{\partial \bar{x}} \\
&= \begin{cases} \dot{\bar{\lambda}}_r = -\bar{\lambda}_v^T \frac{\partial f(\bar{r},\bar{v})}{\partial \bar{r}} \\ \dot{\bar{\lambda}}_v = -\bar{\lambda}_r^T - \bar{\lambda}_v^T \frac{\partial f(\bar{r},\bar{v})}{\partial \bar{v}} \\ \dot{\lambda}_m = \dot{\lambda}_v \frac{T}{m^2} \end{cases}
\end{aligned} \tag{3.39}
$$

$$
\begin{aligned}
\bar{0} &= \frac{\partial H}{\partial \bar{u}} \\
&= \begin{cases} 0 = \frac{\partial H}{\partial T} \\ 0 = \frac{\partial H}{\partial \hat{a}_T} \end{cases} \\
&= \begin{cases} 0 = \bar{\lambda}_v \frac{\hat{a}_T}{m} - \lambda_m \frac{T}{\mathcal{P}} \\ 0 = \bar{\lambda}_v^T \frac{T}{m} + 2\zeta \hat{a}_T \end{cases}
\end{aligned} \tag{3.40}
$$

where ζ corresponds to the Lagrange multipliers associated with the constraint on the direction of the thrust orientation vector of the spacecraft. Moreover, exploiting Pontryagin's maximum principle, it is determined that the performance function is minimized when the thrust direction, $\hat{a}_T$, is oriented parallel to the velocity co-state, $\bar{\lambda}_v^T$, and the power is set at its maximum value, as follows:

$$\mathcal{P} = \mathcal{P}_{max} \tag{3.41}$$

yielding the following control law:

$$\hat{a}_T = \frac{\bar{\lambda}_v^T}{\lambda_v^T} \tag{3.42}$$

This control law is more commonly denoted Lawden's primer vector [86]. Furthermore, since the solution is found via a method for satisfying a set of boundary conditions, the trajectory does meet all initial, final, and path constraints, without directly minimizing the cost function. The main drawback of Lawden's primer vector solution is that the thrust orientation vector is oriented along a different location in space at each time step, which makes its implementation in real-life applications feasibly impossible.

The main drawbacks of the indirect optimization methods are then the difficulty to generate educated initial guesses for the co-states variables —Lagrange multipliers— given that the computation of the required partial derivatives is non-trivial. Furthermore, any changes made to the original formulation of the optimal control problem requires a re derivation of the Euler-Lagrange Theory for the numerical value of the adjoints, and a reformulation of a new two-point boundary value problem arises.

The generation of optimal spacecraft trajectories involves the formulation of an optimal control problem, and the solution of the time histories evolution of the control variables, in order to meet a set of specified boundary conditions. Nonlinear Programming (NLP) techniques are a common approach exploited to compute these histories of the control variables, and solve for the associated Two-Point Boundary Value Problem (TPBVP). In general, it has been shown by previous authors that direct optimization methods are more robust; however, those methods introduce a large increase in the dimensionality of the problem. On the contrary, while indirect optimization schemes also introduce numerical challenges, those are mainly due to the robutsness of the initial guesses. Both approaches —direct and indirect optimization methods— are explored in this investigation.

3.3 Direct Optimization Methods

Direct optimization methods are generally characterized for being more straightforward to implement than indirect approaches. This is due to the fact that the optimal control problem is transformed into a nonlinear programming problem, in which a discretization of the states is performed first, and then, the two-point boundary value problem is addressed. This feature enables for direct approaches to reduce the number of analytical partial derivatives that need to be computed, as well as, easier implementation of terminal constraints [87].

However, one of the main disadvantages of the direct approaches is the increase in dimensionality of the optimal control problem. This drawback can be alleviated by utilizing numerical techniques, that allow for computation of numerical derivatives of Jacobian and Hessian matrices, and hence, a trade-off between large dimensionality of the problem and the potential addition of numerical errors is obtained. Another drawback of the direct optimization approaches is that the solutions found are only locally optimal solution, and there is no guarantee that a global solution can be produced. Ultimately, the optimal solution generated is that which resides in the vicinity of the initial guess provided to the optimization algorithm.

Direct methods use the gradient of the cost function to ensure that, at each iteration, the solution is shifted in a direction that minimizes the norm of the gradient of the performance. The most common approach for direct optimization schemes is to transform the optimal control problem into a parameter optimization problem that can be solved using non-linear programming, as follows:

$$\begin{gathered}\min_{\bar{x}} E(\bar{x}) \\ \text{subject to the inequality constraints } \bar{c}_l \leq \bar{c}(\bar{x}) \leq \bar{c}_u \\ \text{and the bounds } \bar{x}_l \leq \bar{x} \leq \bar{x}_u\end{gathered}$$

where the vector $\bar{c}(\bar{x})$ is comprised of the path constraints, and $E(\bar{x})$ is a function that depends on one or more state variables. Defining a Lagrangian function $\mathbb{L}$, one of the most common approaches for solving a direct optimization problem is the Sequential Quadratic

Programming (SQP) method, that employs a quasi-Newton approach to solve for the Hessian matrix of the Lagrangian equation:

$$\mathbb{L}(\bar{x}, \bar{\lambda}) = E(\bar{x}) - \bar{\lambda}^T \bar{c}(\bar{x}) \tag{3.43}$$

where the vector $\bar{\lambda}$ corresponds to a set of Lagrange multipliers that do not necessarily represent the co-states in Equation (3.38). The necessary conditions for solving the nonlinear programming problem are formed as the gradient of the Lagrangian function with respect to both the states and the Lagrange multipliers:

$$\begin{aligned} \nabla_x \mathbb{L}(\bar{x}, \bar{\lambda}) &= \bar{g}(\bar{x}) - \mathbb{G}^T(\bar{x})\bar{\lambda} = 0 \\ \nabla_\lambda \mathbb{L}(\bar{x}, \bar{\lambda}) &= -\bar{c}(\bar{x}) \end{aligned} \tag{3.44}$$

for which $\bar{g}(\bar{x}) = \nabla_x E$, is the gradient of the performance function, and $\mathbb{G}$ is the Jacobian matrix of the equality constraint vector. To obtain the updates of the states and the Lagrange multipliers, the following linear system is formed

$$\begin{bmatrix} H_L & -\mathbb{G}^T \\ \mathbb{G} & \bar{0} \end{bmatrix} \begin{Bmatrix} \Delta\bar{x} \\ \Delta\bar{\lambda} \end{Bmatrix} = \begin{Bmatrix} -\bar{g} \\ -\bar{c} \end{Bmatrix} \tag{3.45}$$

where H_L represents the Hessian matrix, or matrix of second derivatives of the equality constraints. Note that by utilizing direct methods, a turn-and-hold model can be constrained on the thrust orientation vector, which facilitates feasibility of real-life implementation finite-burn maneuvers.

Another characteristic of the direct optimization techniques, mainly when apply to the low-thrust trayectory design problem, is that the vector of control variables —design variables— are dicretized along the baseline trajectory. Furthermore, the locally optimal solution is generated by implementing the Karush-Kuhn-Tucker (KKT) conditions for optimality [88]:

1. The optimal solution found, $\bar{x}^*$, is feasible

2. Let the Lagrange multipliers utilized to adjoint the constraints on the state vector be defined by $\bar{\nu} \geq 0$, then, the following equation must be satisfied for every i^{th} discretization step:

$$\nu_{\mathrm{i}} g_{\mathrm{i}}(\bar{x}^*) = 0$$

3. the gradient of the augmented objective function vanishes

These conditions are valid for all constraints within or on the boundaries, characteristic that makes the locally optimal solution found with direct approaches robust to the implementation of constraints both on the state variables or on the vector of controls.

3.4 Global Optimization Methods

Conway [81] introduced the concept of global optimization techniques as an attempt to alleviate the burden for direct and indirect optimization approached to find a globally optimal solution. These methods are generally characterized for exploring a large sample space and multiple combination of initial guesses, in order to arrive at a global optimal, hence, the trade-off involves a larger computation time utilizing numerical methods, than those necessitated with direct and/or indirect approaches.

Many variations of global optimization methods have been introduced in the low-thrust trajectory design problem by multiple authors [89]–[92], and some examples of these type of optimization approaches include, but are not limited to, ant-colony optimization, monotonic basin hopping, dynamic programming, and more recently, reinforcement learning approaches [93]–[95].

3.4.1 Dynamic Programming

In Dynamic Programming (DP), an optimal control is found by the principle of optimality (PoO). Dynamic Programming is a computational technique which extends a decision-making concept to sequences of decisions which together define an optimal policy (optimal control history). Consider the cost function $\mathcal{J}(u)$ given by:

$$\mathcal{J}(u) = \check{\phi}\left(x(t_f), t_f\right) + \int_{t_0}^{t_f} \{\mathcal{L}\left(x(t), u(t), t\right)\} dt \tag{3.46}$$

with $t \in [t_0, t_f]$; the dynamics of the system are given by:

$$\dot{x}(t) = f\left(x(t), u(t), t\right) \tag{3.47}$$

subject to the initial conditions $x(t_0) = x_0$. Define a value function, $\mathcal{V}^*$, for the time interval $[t_1, t_f]$, where $t_0 < t_1 < t_f]$, such that:

$$\mathcal{V}^*(x^*, t_1) = \min_u \{\check{\phi}\left(x(t_1), t_1\right) + \int_{t_1}^{t_f} \{\mathcal{L}\left(x^*(t), u(t), t\right) dt\}\} \tag{3.48}$$

taking the derivative of the value function with respect to time yields:

$$-\frac{\partial \mathcal{V}^*(x^*, t_1)}{\partial t} = \mathcal{L}\left(x^*(t_1), u^*(t_1), t_1\right) + \left(\frac{\partial \mathcal{V}^*}{\partial x}\right) f\left(x^*(t_1), u^*(t_1), t_1\right) \tag{3.49}$$

Recall the definition of the Hamiltonian function:

$$\mathcal{H}\left(x(t), u(t), \lambda(t), t\right) = \mathcal{L}\left(x(t), u(t), t\right) + \lambda^T(t) f\left(x(t), u(t), t\right) \tag{3.50}$$

setting

$$\lambda(t)^{*T} = \frac{\partial \mathcal{V}^*}{\partial x} \tag{3.51}$$

along the optimal trajectory, yields Hamilton-Jacobi-Bellman (HJB) equation given by:

$$-\frac{\partial \mathcal{V}^*(t)}{\partial t} = \mathcal{H}\left(x^*(t), u^*(t), \frac{\partial \mathcal{V}^*(t)}{\partial x}, t\right) \tag{3.52}$$

with the boundary condition:

$$\mathcal{V}^*(t_f) = \check{\phi}\left(x^*(t_f), t_f\right) \tag{3.53}$$

Some of the advantages of the Dynamic Programming schemes include that the constraints on the states and control variables are easily incorporated, DP yields the optimal control in a feedback form, and, it utilizes the principle of optimality to dramatically reduce the number of calculations required to determine the optimal control laws. Furthermore, the HJB equation is in concert with the Maximum Principle, and should be integrated backwards in time. The value function may not be differentiable [96].

4. CISLUNAR TRAJECTORY DESIGN FRAMEWORK

Within the context of trajectory design for vehicles powered by low-thrust engines in the vicinity of the Moon, the generation of locally optimal solutions for the control history of the thrust orientation vector is a non-trivial process, challenging in terms of both time-of-flight and propellant usage [97], [98]. Multiple geometries exist in the design of low-cost low-thrust transfers between libration point orbits. These geometries depend upon the physical constraints of the low-thrust engine, in terms of both magnitude and orientation of the thrust vector, and on the stability characteristics of the destination and departure orbits. Within the context of the unperturbed Circular Restricted Three-Body Problem (CR3BP), where the primary bodies are assumed to be point masses, the dynamical equations of motion that describe the behavior of a spacecraft in this system are time-invariant [99]. With the introduction of a thrust force, the time dependency also induces an energy variation. In this investigation, the geometries of the transfer trajectories for a low-thrust vehicle, are described in terms of three types of categories for low-thrust transfers between libration point orbits.

- Direct transfers: transfers that resemble the geometry of minimum impulsive burn trajectories.

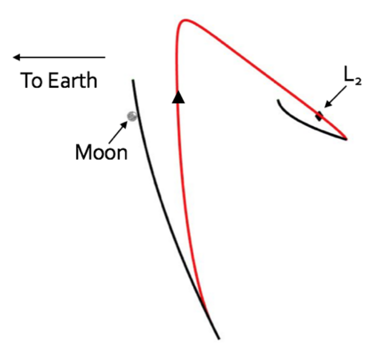

Figure 4.1. Sample Direct Transfer

- Interior Transfers or Sliding-Type Geometry: transfers that access multiple members of periodic orbit families, to generate solutions that do not depart the vicinity of interest.

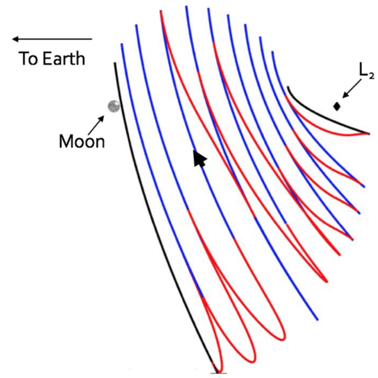

Figure 4.2. Sample Interior Transfer or Sliding-Type Geometry

- Exterior Transfers or Escape-Type Geometry: trajectories that utilize exterior manifold arcs and/or exterior-type orbits, to generate transfers that depart the vicinity of interest with a possible return.

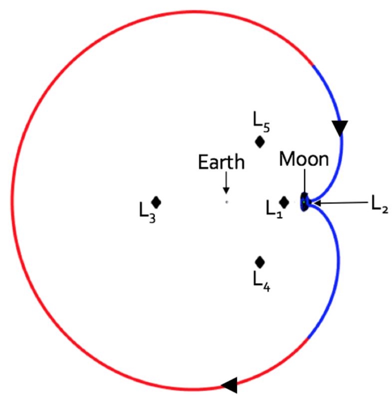

Figure 4.3. Sample Exterior Transfer or Escape-Type Geometry

The sliding algorithm described in this investigation accommodates all three categories of transfer geometries by exploiting an orbit chaining framework [100].

The orbit chaining framework employs any type of dynamical structure. The main goal of the sliding algorithm strategy is, then, to identify natural dynamical structures, such as periodic orbits or invariant manifold branches, to traverse the gaps in position and velocity space between a departure and an arrival orbit. The orbit chain is constructed following the six-steps below:

1. Analyze any dynamical structures that exist in the vicinity of the departure and arrival orbits.

2. Select natural arcs that offer high-efficiency energy paths

3. Clip the sections of the arcs that best suit the transfer requirements and form an initial guess.

4. Subdivide the initial guess for the trajectory into smaller segments and patch points.

5. Stack additional revolutions of the initial and final orbits as appropriate.

6. Define the control history by utilizing either a differential corrections process or an optimizer, to produce a converged solution.

The previous steps detailed the procedure realized in the adaptive algorithm to construct locally optimal solutions via orbit chaining, by identifying and utilizing the minimum number of intermediate arcs to link together from the departure to the arrival orbits which subsequently produces an end-to-end transfer.

Transfers with a sliding-type geometry exploit natural arcs within an orbit chaining framework and offer the capability to identify interior transfer geometries when manifolds arcs are not available. The orbit chaining framework then allows any periodic orbit that exists within the model to be leveraged as an intermediate arc and to generate suitable initial guesses for all the various type of transfers:

1. To generate direct transfers, the adaptive sliding algorithm selects the values for the maximum thrust acceleration level, and the engine specific impulse, to resemble those of chemical engines.

2. To compute interior transfers, the adaptive sliding algorithm utilizes arcs from families of periodic orbits within the vicinity of interest.

3. To produce exterior transfers, the adaptive sliding algorithm exploits arcs from families of periodic orbits that experience long transits throughout the Earth-Moon system.

The complexity in designing these transfer trajectories is first addressed by exploring the dynamics for the low-thrust spacecraft in an environment where the motion of the vehicle is described in a multi-body scenario. The adaptive sliding algorithm is formulated within this context. Thus, the various energy levels and stability characteristics across families of multi-body orbits that exist within this model —the Low-Thrust augmented Circular Restricted Three Body Problem (CR3BP-LT)— are exploited. The fidelity of the results from this algorithm is further expanded to an ephemeris model that includes the gravitational attraction of the Sun, the Earth and the Moon (SEM ephemeris model).

4.1 Generation of Exterior Transfers

In this investigation, the proposed scheme for constructing initial guesses to deliver exterior-type geometries for low-thrust spacecraft trajectory is summarized in the diagram in Figure 4.4. The spacecraft originates in the vicinity of the libration point orbits in the CR3BP as represented for the Earth-Moon system. The strategy then varies for spacecraft pathways to link two stable orbits, two unstable orbits, or a combination.

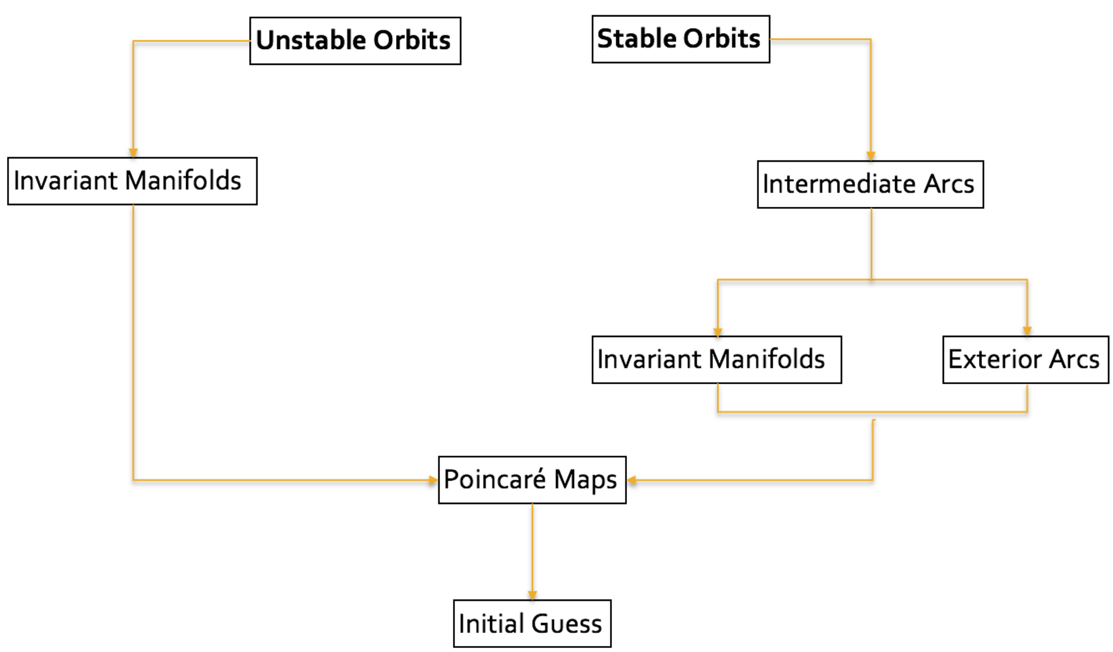

Figure 4.4. Graphical representation of the algorithm for generation of exterior trajectories

Within the context of the CR3BP a periodic orbit is a solution to the nonlinear differential equations and represents the motion of the spacecraft as a closed periodic path. To analyze the stability of periodic orbits, the model is formulated in terms of a set of linear variational equations [101]. The solution to this linear system is:

$$\delta\bar{x}(t) = \Phi(t, t_0)\delta\bar{x}(t_0) \tag{4.1}$$

where $\delta\bar{x}(t)$ represents the variations of the state vector at time t, $\Phi(t, t_0)$ corresponds to the State Transition Matrix (STM) and $\delta\bar{x}(t_0)$ identifies the initial variations of the state vector. The eigenvalues of the monodromy matrix are the modes that dictate the linear behavior in the vicinity of a periodic orbit and, therefore, its stability.

The state vector in the natural CR3BP —that is, the system for which the low-thrust acceleration has not been incorporated— is six-dimensional (three dimensions corresponding to the position elements, and three for the velocity components). Representing a periodic orbit as a fixed point, its stability is assessed via the monodromy matrix (i.e., the state transition matrix after precisely one period of the orbit). For a given location along the orbit, the monodromy matrix corresponding to each fixed point possesses six eigenvalues and a corresponding set of associated eigenvectors. Two eigenvalues, denoted the trivial pair, are always equal to one; the remaining four eigenvalues, denoted the nontrivial eigenvalues, occur as two reciprocal pairs, and are of the form $\lambda_{\mathrm{i}} = a \pm b_{\mathrm{j}}$, with $\mathrm{i} = 1, , 4$ and $\mathrm{j} = 1, 2$, where a and b are real numbers. Figure 4.5 offers a representation of the magnitude of the eigenvalues in the complex plane.

The linear stability of a periodic orbit is determined by considering the form and magnitude of each of the four nontrivial eigenvalues; there are two possible forms for each of the nontrivial pairs [102]:

- Complex roots, i.e., $\lambda_{1,2} = a \pm b_{\mathrm{i}}$. If the roots lie on the unit circle, the solution is bounded, or marginally stable; a perturbed path neither approaches nor departs from the reference over time.

- Real roots, i.e., $b = 0$ and $\lambda_1 = a$, $\lambda_2 = 1/a$. These roots correspond to exponential growth or decay of the variation between the reference and perturbed paths over time.

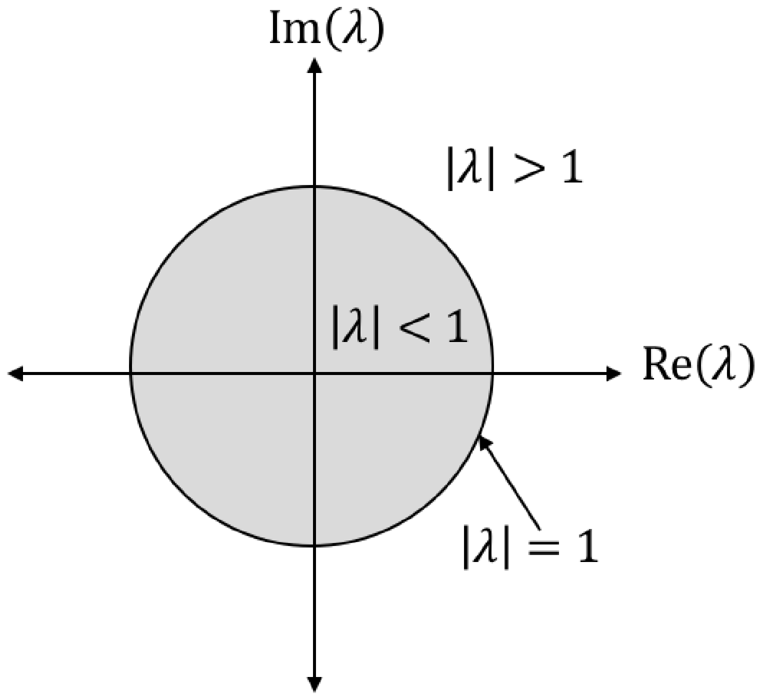

Figure 4.5. Graphical representation of Magnitude of the Eigenvalues of the Monodromy Matrix in the Complex Plane

Following the schematic in Figure 4.4, if one or both of the departure and arrival orbits exhibit unstable behavior, a Poincaré map analysis is completed. Alternatively, if both orbits exhibit stable behavior, an alternate structure is sought as an intermediate arc, one that exists in the form of manifold structures or exterior-type periodic orbits, for example, resonant orbits, and drive the geometry of the final transfer.

One of the most common approaches to generate resonant orbits consist of correction strategies and/or continuation methods, to transform a two-body resonant periodic orbit into the three-body model. Within the context of the Earth-Moon CR3BP model, a spacecraft is defined to be in p:q resonance with the Moon, if it completes p orbits with respect to the Earth in the same time interval in which the Moon achieves exactly q orbits [22]. In this definition, p and q are two positive integers. Employing a continuation method, a family of resonant orbits is generated and, similar to the families of libration point orbits, may offer useful options for constructing trajectories in more complex scenarios. Figure 4.6 represents a 3:4 resonant family of orbits as an example of suitable candidates for the initial guess generation of exterior transfers.

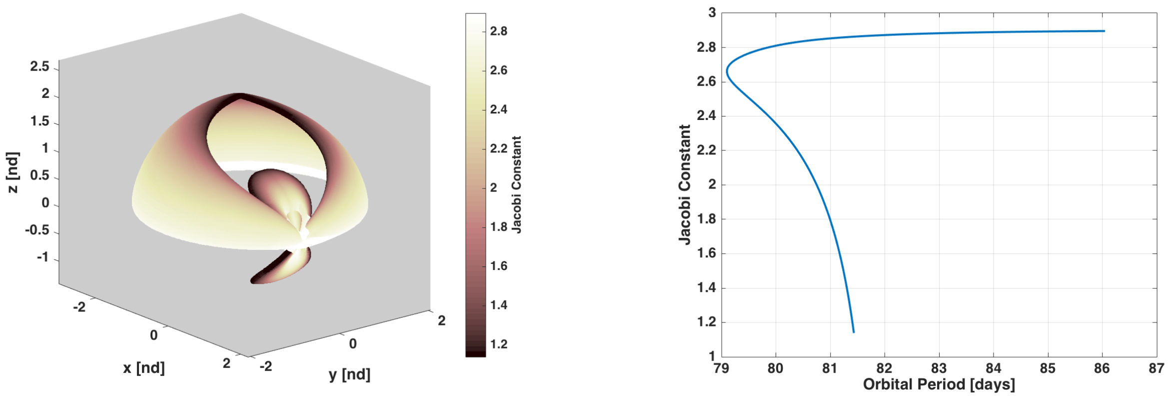

(a) Sample 3:4 Resonant Family. Spatial View.

(b) Sample 3:4 Resonant Family. Energy Evolution.

Figure 4.6. Sample 3:4 3D Resonant Family in the Earth-Moon CR3BP

Significant insight into the flow along a trajectory is accomplished by reducing the dimension of the system such that implicit information is captured in a lower dimensional visual representation. Poincaré mapping is a very useful approach to effectively reduce the dimensionality of a dynamical system and allow for concise visualization of the flow.

4.1.1 Poincaré Mapping

Poincaré maps are a very powerful tool for understanding and visualizing the underlying dynamics of a particular region of space. These maps are greatly used in the trajectory design problem to construct initial conditions for spacecraft transfers.

To construct such a map, a hyperplane or surface of section (Σ^+) is selected as illustrated in Figure 4.7, at which crossings of a propagated trajectory for a variety of initial conditions, $\bar{x}_1$, are recorded. The mapping $\bar{x}_1 \rightarrow \rho(\bar{x}_1)$ is then termed the Poincaré map, and each time a propagation crosses the hyperplane, its information is recorded [28]. The quantity $\rho(\bar{x}_1)$ is referred to as an iteration of the initial condition, $\bar{x}_1$.

Any initial state on a Poincaré map unveils the set of all intersections recorded on the hyperplane, offering a deeper understanding of the dynamical system behaviour in the spec-

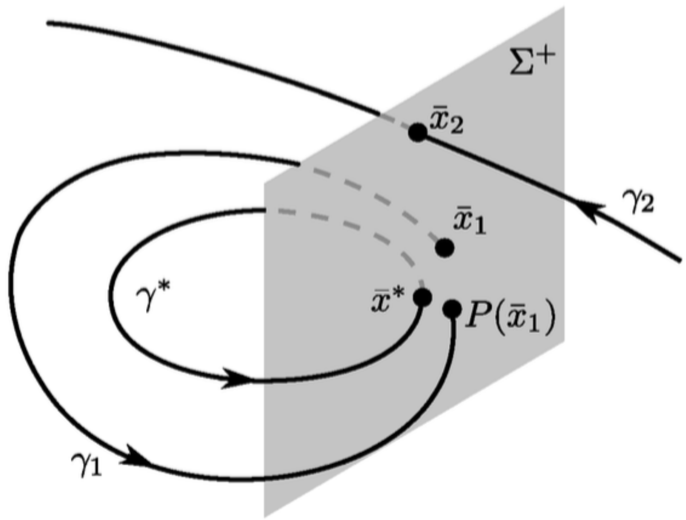

Figure 4.7. Graphical representation of a Poincaré section

ified region of interest. The generation of exterior trajectories for linking unstable orbits is then accomplished by propagating the branches from the invariant manifolds or from exterior resonant orbits and represent them on a map [103]. The corresponding intermediate arcs are extracted for inclusion in the construction of an initial guess. An infinite number of possibilities exist for the selection of intermediate orbits —or arcs— and a few are examined in this investigation.

A Poincaré map can be generated either using short- or long-duration simulations of the initial conditions; however, utilizing short-duration arcs generally yields incomplete structures, that do not provide sufficient insight into the natural flow. In the low-thrust trajectory design problem for generating transfers between periodic orbits within the context of the CR3BP, Poincaré mapping techniques are utilized to capture the recording of long manifold arcs emanating from unstable periodic orbits into a specified hyperplane. Figure 4.8 illustrate a sample for the unstable and stable branches of the manifold arcs that naturally approach the periodic orbit. The Red and Magenta arcs correspond to the positive and negative directions of the unstable manifold branches, respectively, propagated in forward time from the periodic orbit. Similarly, the blue and cyan arcs represent the positive and negative directions of the stable manifold branches, propagated backwards in time from the periodic orbit.

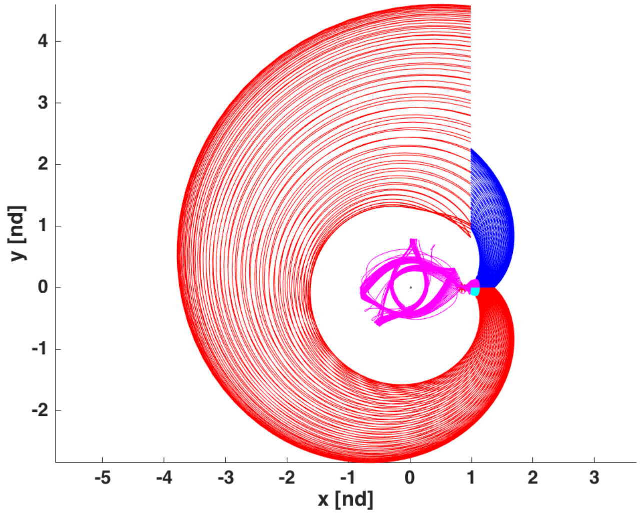

Figure 4.8. Sample Representation of Unstable and Stable Manifold Branches for Libration Point Orbits in the CR3BP.

The intersection of these manifold crossings on the hyperplane of the Poincaré map are presented in Figure 4.9; each point on the map correspond to a distinct ballistic trajectory. Blue points represent the crossings of positive stable manifold branch, and the red points represent the crossings of positive unstable manifold branch; the selection of points that overlap in the Poincaré map, serves as the initial guess trajectory for finding transfer options between these libration point orbits.

4.2 Generation of Interior Transfers: Adaptive Sliding Algorithm

The proposed decision process for constructing sliding-type solutions in the CR3BP-LT model, is summarized in Figure 4.10. Note that the framework ultimately incorporates slides through any number of different families that are then stacked to reach a destination. To estimate the minimum number of intermediate orbits for 'sliding' enroute to the destination, the procedure relies on a parametrization of the energy evolution for the family in consideration, along with an accessible region —in configuration space— provided by the thrust capabilities of the spacecraft. This accessible region is denoted the Thrust Range Surface (TRS).

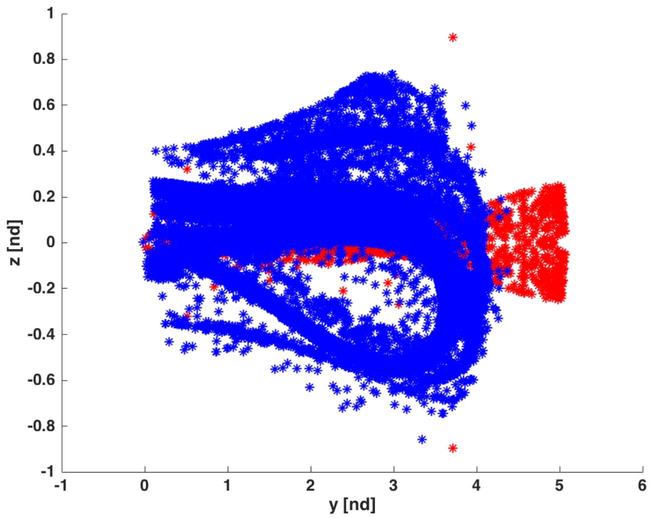

Figure 4.9. Sample Representation of a Poincaré Map Reflecting the Crossings of the Unstable and Stable Manifold Branches for a Libration Point Orbit in the CR3BP.

The algorithm is initialized by supplying three user-defined inputs: the departure and destination orbits as well as the maximum thrust acceleration level available due to the physical capabilities of the spacecraft. The output is a fully converged locally optimal transfer between the two orbits of interest. Furthermore, the solutions of this type do not depart the lunar vicinity (or some other bounded region in configuration space). The approach for constructing sliding-type geometry transfers is summarized, and visually represented, in the two steps described below. The sample transfer for a 14kg low-thrust spacecraft from a L_2 Southern (S) Near Rectilinear Halo Orbit (NRHO) to a L_2 Northern (N) halo orbit, with a maximum thrust acceleration level consistent with that of the Lunar IceCube spacecraft, $8 \times 10^{-5} m/s^2$ is described as follows:

Step 1. Once the departure and arrival orbits are identified, as in Figure 4.11(a), the algorithm loads (or computes) a full representation of the families to which these orbits of interest belong. The capability does exist to represent additional families in the vicinity. For each family of interest, its representation in configuration space, as well as its period and energy evolution, are populated. While there exist multiple ways of parametrizing the

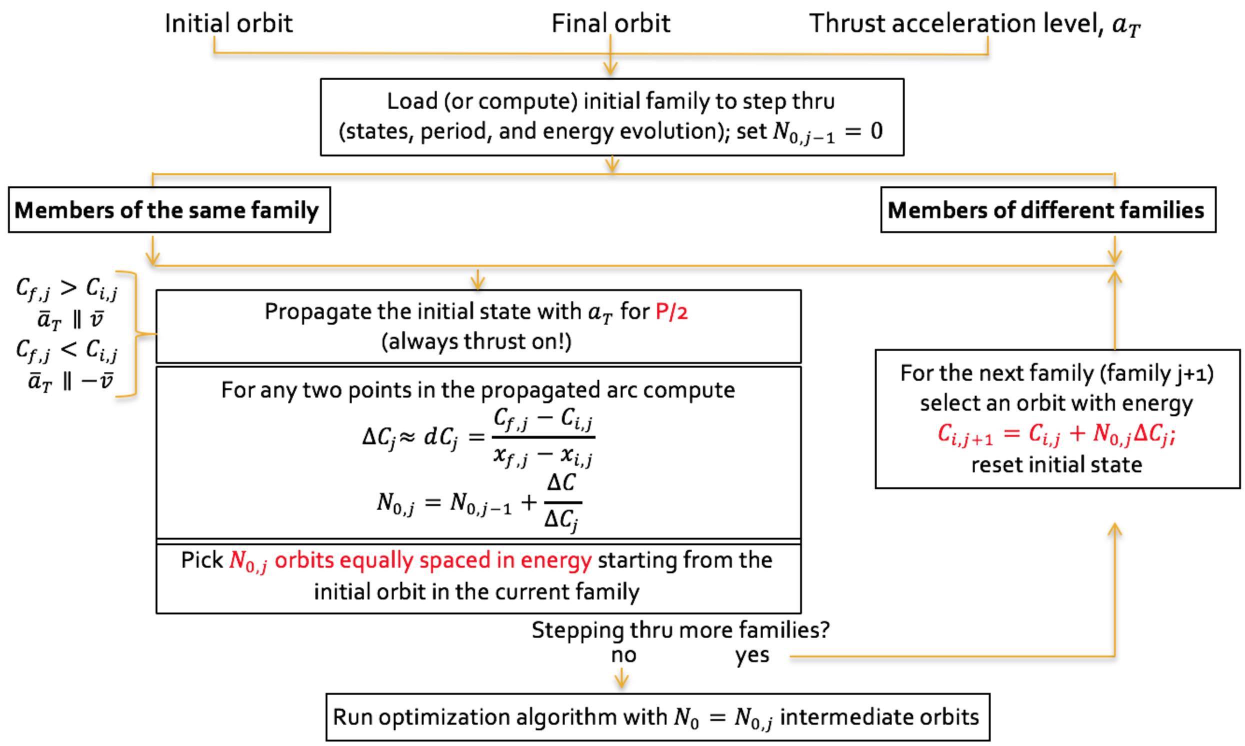

Figure 4.10. Energy-Informed Sliding Algorithm for Generation of Interior Trajectories

energy evolution along a family of periodic orbits, the strategy in this algorithm employs a representation of the Jacobi constant evolution across the members of the family against the maximum and minimum x- coordinates for each orbit member as illustrated in Figure 4.11(b); this representation produces a surface denoted the Energy Surface (ES) along the family, from which a limited grid search is conducted to select the intermediate orbits to serve as the initial guess for the transfer.

When the Energy Surface in Figure 4.11(b) exhibits monotonic growth (i.e., no extrema along the curve), this behavior indicates that no two orbits in the family possess the same value of Jacobi constant. Hence, once a direction of motion is identified, intermediate orbits for sliding are directly selected from the Energy Surface, either to increase or to decrease the energy to a value equal to that of the target orbit.

When the energy surface exerts a non-monotonic growth (i.e., extrema along the curve), it suggests that the energy associated with each member of the family is no longer unique, and an extra step is required to identify the intermediate orbits best suited to slide through

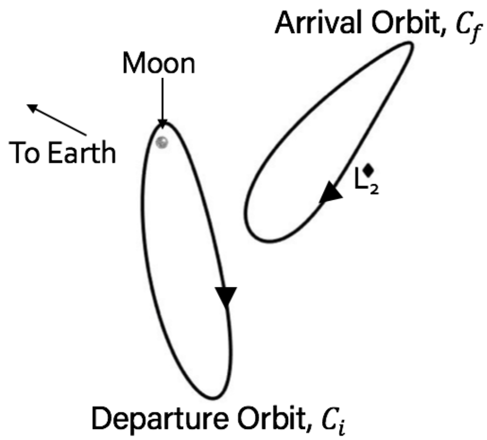

(a) Sample Departure and Arrival Orbits from the L_2 S and N Halo Families of Orbits.

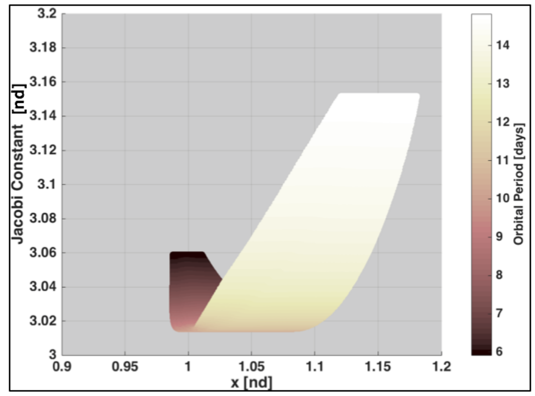

(b) Energy Surface for the L_2 S Halo Family.

Figure 4.11. Sample Problem Setup for the Adaptive Sliding Algorithm

enroute to the destination orbit. This remark also suggests that the sliding direction across the family is not unique, i.e., there exist multiple ways to construct initial guesses for the sliding-type geometry. Two approaches for the selection of the intermediate orbits when energy is not unique, are explored in this investigation: 1. A Thrust Range Surface (TRS) (Figure 4.12), jumps along the Energy Surface, skipping the extrema in energy, and reducing the redundancies; 2. The algorithm decreases and/or increases energy in a non-monotonic fashion, by shifting the Energy Surface without skipping the extrema.

A Thrust Range Surface is a map in configuration space; the values of the components of the state vector are recorded at the end of a propagation segment that is initiated with the same set of initial conditions, but with only the thrust direction modified for each outcome. This surface supplies initial guesses for arcs that do not slide incrementally through the family, rather arcs that are jumping along the Energy Surface to a value for which the selection of the orbit ultimately becomes unique. The shape and reach of a Thrust Range Surface is a function of the acceleration magnitude as well as the orbit being examined.

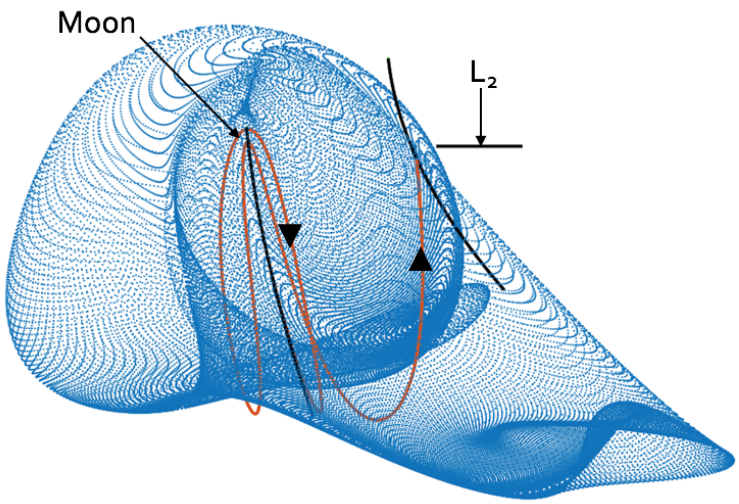

Figure 4.12. Thrust Range Surface for a L_2 Southern Near Rectilinear Halo Orbit (NRHO); TRS, Used to Skip Extrema along the Energy Surface

Step 2. To generate a converged locally optimal solution, the strategy then involves the formulation of an energy-informed minimization problem. The goal is the determination of the smallest number of intermediate orbits, N, that minimize the following cost function:

$$J = \min_{N \in \mathbb{N}} \left\{ \left[W_1 \left(\frac{1}{2} \sum_{\mathrm{j}=1}^{N} \Delta C_{\mathrm{j}}^2 \right) \right] - [W_2 ToF] \right\} \tag{4.2}$$

where C_{j} represents the energy of each intermediate orbit as reflected in the corresponding value of the Jacobi constant, and ToF is the total time-of-flight along the transfer. This nondimensional objective function is comprised of two different terms: (i) an energy related term, whose main purpose is the reduction of the number of energy changes from one propagation arc along the transfer to the next; such a minimization is accomplished by means of a mass-optimal solution; and (ii) a time-of-flight term, included in the objective function to accommodate time-optimal trajectories. The weights associated with each of the individual terms are represented by $W_{1,2}$, respectively, and aid in prioritizing the type of optimal transfer to be delivered. The problem formulation then requires an initial guess for the optimal number of intermediates orbits, N_0, as well as for the change of energy per orbit, $\Delta C_{\mathrm{j}0}$.

To generate mass locally optimal transfers with a sliding-type geometry, the sliding algorithm solves the minimization problem in Equation (4.2), by initially assigning $W_1 = 1$ and

$W_2 = 0$. From the initial guess, a feasible solution is first generated by means of a multiple-shooting differential corrections scheme that discretizes each intermediate orbit into patch points and segments (each of which is allowed to thrust or coast over the duration of the arc); The discretization scheme allows n total points and $n-1$ total segments, as illustrated in Figure 4.13, where $\bar{x}_\mathrm{j}$ represents the state vector for each segment j, and the control variables required per arc segment are identified. The orientation of the thrust vector is defined by the control angles α and β that correspond to the in-plane and out-of-plane angles, respectively, and orient the thrust acceleration vector in the barycentric rotating frame. The algorithm employs a turn-and-hold control logic, such that the same thrust magnitude and orientation are fixed over the duration of each thrust/coast arc.

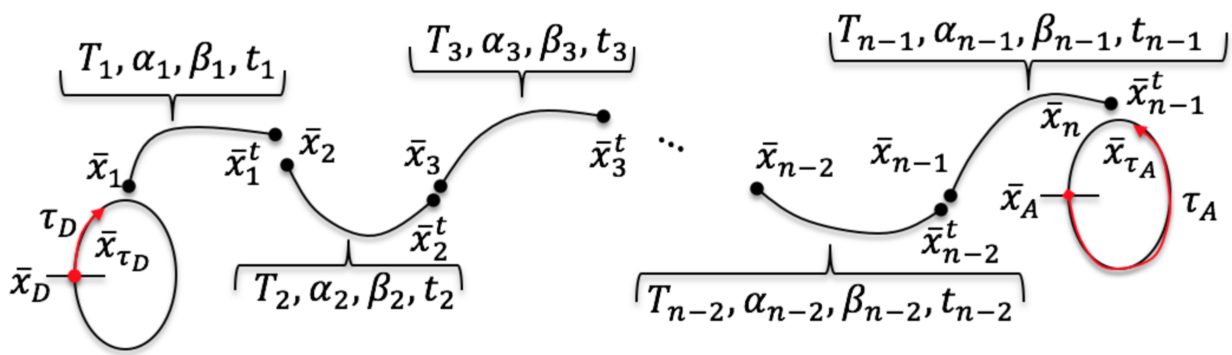

Figure 4.13. Illustration of a Multiple Shooting Differential Corrections Strategy for Low-Thrust Trajectory Solutions

4.2.1 Energy-Informed Initial Guess Generation

The basic framework in the adaptive algorithm is identifying the intermediate arcs through which the vehicle 'slides' enroute to its destination. As a first step, assume that the goal is 'sliding' along a single family of orbits employing a low-thrust force to accomplish the corresponding energy change. The main goal of the reduced algorithm is, then, the construction of the minimum number of intermediate orbits through which to 'slide' from departure to destination.

The initial guess estimate for the minimum number of intermediate orbits, N_0, that are required for sliding-type transfers between cislunar orbits that exist within the same family in the CR3BP model, is accomplished by leveraging the Jacobi constant of integration. For any particular transfer, once the departure and arrival orbits are identified, the total net energy change to accomplish the transfer is deduced from the simple relationship:

$$\Delta C = C_{departure} - C_{arrival} = C_{\mathrm{i}} - C_f$$

where $C_{\mathrm{i}} = C_{departure}$ is the energy of the initial/departure orbit, and $C_f = C_{arrival}$ corresponds to the energy of the final/destination orbit. Furthermore, the energy of the arrival orbit is decomposed in terms of the change in energy between each pair of intermediate orbits as follows:

$$C_f = C_{\mathrm{i}} + \sum_{\mathrm{j}=1}^{N} \Delta C_{\mathrm{j}} \tag{4.3}$$

To determine the initial direction of motion along the energy surface in Figure 4.11(b), i.e., the initial orientation of the thrust vector, the following logic is implemented:

$$\begin{cases} \bar{a}_T \| \bar{v} & \text{if } C_{f,\mathrm{j}} < C_{\mathrm{i,j}} \\ \bar{a}_T \| -\bar{v} & \text{if } C_{f,\mathrm{j}} > C_{\mathrm{i,j}} \end{cases}$$

If $C_{\mathrm{i,j}}$ represents the energy of the current intermediate orbit, and $C_{f,\mathrm{j}}$ is the energy of the next intermediate orbit, the algorithm induces thrust along the relative velocity direction whether or not an increase in energy is desired per Equation (4.3). Once the initial thrust arc is propagated for a fixed duration, the algorithm evaluates a linear approximation for the initial change in energy per orbit as described in Figure 4.14(a), and employs this approximation to estimate an initial guess for the number of intermediate orbits. This process is represented graphically as described in Figure 4.14(b), and computed numerically as follows:

$$\Delta C_{\mathrm{j}0} \approx dC_{\mathrm{j}} = \frac{C_{f,\mathrm{j}} - C_{\mathrm{i,j}}}{x_{f,\mathrm{j}} - x_{\mathrm{i,j}}} \tag{4.4}$$

$$N_{0,\mathrm{j}} = \frac{\Delta C}{\Delta C_{\mathrm{j}0}} \tag{4.5}$$

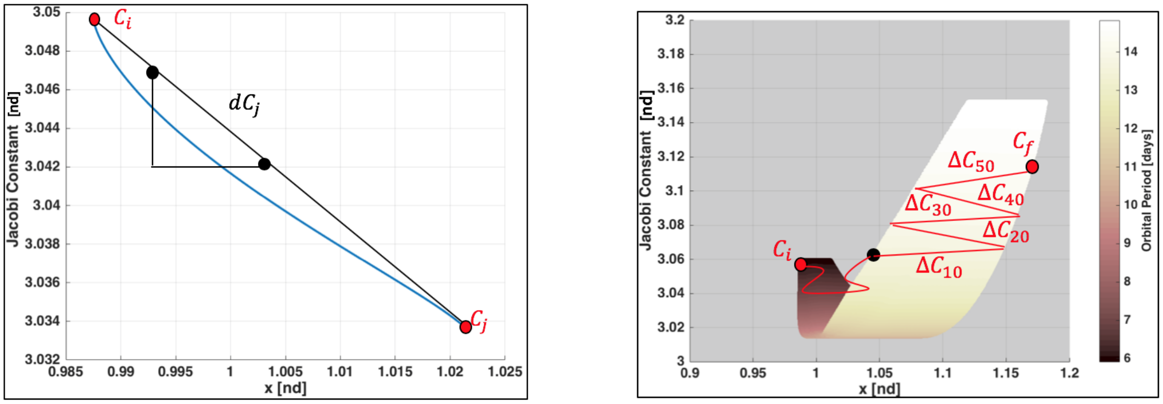

(a) Linear Approximation of Energy Change due to Maximum Thrust Acceleration Magnitude.

(b) Initial Estimate for Number of Intermediate Orbits in the L_2 S Halo Energy Space.

Figure 4.14. Visual Representation of the Energy-Informed Initial Guess Generation Process

Consider the regular expression for the Jacobi constant and its time derivative, augmented by the thrust acceleration term, where U^* is the pseudo-potential function of the natural CR3BP dynamics:

$$C = C\left(\bar{r}, \bar{v}, \bar{a}_T\right) = 2U^* - v^2 + 2\left(\bar{r} \cdot \bar{a}_T\right) \tag{4.6}$$

$$\begin{aligned}
\frac{dC}{dt} &= 2\frac{d}{dt}\left(U^*\right) - \frac{d}{dt}\left(x^2+y^2+z^2\right) + 2\frac{d}{dt}\left(\bar{r}\cdot\bar{a}_T\right) \\
&= 2\left(U_x^*\dot{x} + U_y^*\dot{y} + U_z^*\dot{z}\right) - 2\left(\dot{x}\ddot{x} + \dot{y}\ddot{y} + \dot{z}\ddot{z}\right) + 2\left(\dot{\bar{r}}\cdot\bar{a}_T + \bar{r}\cdot\dot{\bar{a}}_T\right) \\
&= 2\left[\dot{x}\left(U_x^* - \ddot{x}\right) + \dot{y}\left(U_y^* - \ddot{y}\right) + \dot{z}\left(U_z^* - \ddot{z}\right) + \left(\dot{\bar{r}}\cdot\bar{a}_T + \bar{r}\cdot\dot{\bar{a}}_T\right)\right] \\
&= 2\left[-2\dot{x}\dot{y} + 2\dot{y}\dot{x} + \dot{z}\left(0\right) + \left(\dot{\bar{r}}\cdot\bar{a}_T + \bar{r}\cdot\dot{\bar{a}}_T\right)\right] \\
&= 2\left(\dot{\bar{r}}\cdot\bar{a}_T + \bar{r}\cdot\dot{\bar{a}}_T\right)
\end{aligned} \tag{4.7}$$

Equation (4.7) represents the exact relationship between the rate of change of energy with respect to time, and the thrust acceleration level of the spacecraft. Moreover, using a Taylor series representation, the energy-like function in Figure 4.14(a) is expressed as:

$$C = C_1 + \frac{dC}{dx}(x - x_1) + \frac{1}{2!}\frac{d^2C}{dx^2}(x - x_1)^2 + ... \tag{4.8}$$

Let $\Delta C = C - C_1$ be the total change in energy from point (x_1, C_1) to point (x, C). Furthermore, from assumptions in direct optimization methods, approximate $dx = (x - x_1)$ to be small but finite, such that the following equations is valid:

$$dC = \tfrac{dC}{dx}dx, \text{ and } d^2C = \tfrac{d^2C}{dx^2}dx^2$$

To produce the general representation for the change of energy over a thrust segment:

$$\Delta C = dC + \frac{1}{2!}d^2C + ... \tag{4.9}$$

Equation (4.9) is then generalized to solve the optimization problem of interest, in Equation (4.2), such that the total change of energy per intermediate orbit is evaluated as:

$$\Delta C_{\mathrm{j}} = dC_{\mathrm{j}} + \frac{1}{2!}d^2C_{\mathrm{j}} + ... \tag{4.10}$$

where C_{j} corresponds to the energy-like function in Equation (4.6), and its derivatives are computed numerically by the sliding algorithm as follows:

$$dC_{\mathrm{j}} = \frac{\partial C_{\mathrm{j}}}{\partial \bar{r}}d\bar{r} + \frac{\partial C_{\mathrm{j}}}{\partial \bar{v}}d\bar{v} + \frac{\partial C_{\mathrm{j}}}{\partial \bar{a}_T}d\bar{a}_T \tag{4.11}$$

As indicated in the diagram in Figure 4.10, the process continues for each family that is incorporated into the construction of a particular initial guess for a transfer with a sliding-type geometry. For the sample scenario being examined, a visual representation of the initial guess in configuration space is illustrated in Figure 4.15(a). The algorithm then utilizes a direct optimization process via a multiple-shooting approach, as described in the previous section, to generate the optimal solution in the CR3BP-LT model in Figure 4.15(b).

To produce this solution, the sliding algorithm employs two intermediate orbits —one member of the southern halo family and one member of the northern halo family— combined with the TRS generated for the departure orbit, while guaranteeing that the constraint on the maximum thrust acceleration magnitude is not violated. To further evaluate the accuracy

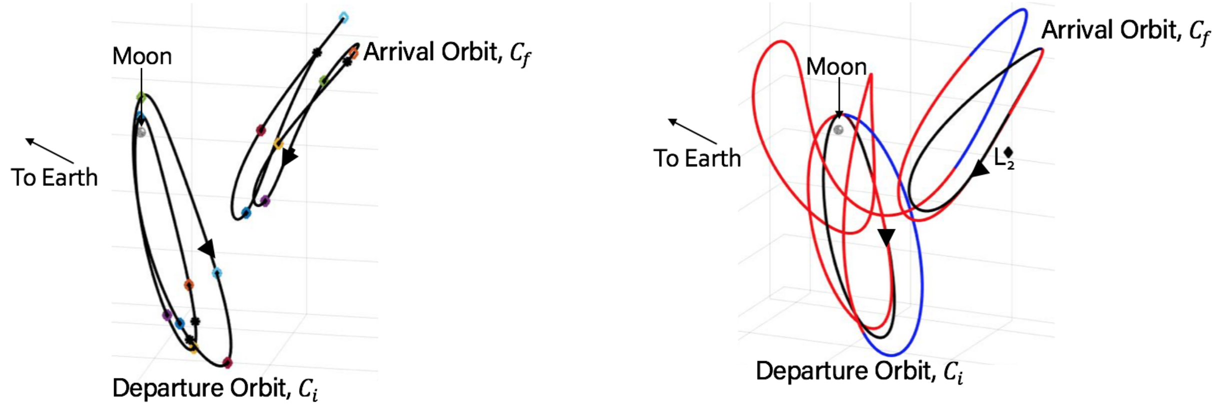

(a) Initial Guess from the Sliding Algorithm.

(b) Mass Optimal Converged Solution.

Figure 4.15. Sample Transfer Scenario from a L_2 S NRHO to a L_2 N Halo Orbit in the CR3BP-LT Model via Sliding Algorithm. Red and blue arcs represent thrust and coast arcs, respectively

and robustness of the adaptive sliding algorithm, all results are transitioned to a higher-fidelity ephemeris force model.

4.3 Corrections Algorithm for Low-Thrust Trajectory Solutions in the CR3BP-LT

The corrections process is implemented via a multiple-shooting scheme, one that seeks to generate a feasible solution that is continuous in the position, velocity and mass states. This multiple-shooting approach determines a solution by employing a multi-dimensional iterative Newton strategy, in which the update equation is based on the minimum norm solution as:

$$\bar{X}_{\mathrm{j+1}} = \bar{X}_{\mathrm{j}} - DF(\bar{X}_{\mathrm{j}})^T \left[DF(\bar{X}_{\mathrm{j}}) DF(\bar{X}_{\mathrm{j}})^T \right]^T \bar{F}(\bar{X}_{\mathrm{j}}) \tag{4.12}$$

where $\bar{X}_{\mathrm{j}}$ represents the vector of free variables —or controls— as in Figure 4.13, $\bar{F}(\bar{X}_{\mathrm{j}})$ corresponds to the vector of constraints, and $DF(\bar{X}_{\mathrm{j}})$ is the Jacobian matrix comprised of the partial derivatives of the constraints with respect to the free variables. Furthermore, all inequality constraints are converted into equality constraints via the use of slack variables, such that those constraints are also included in the vector $\bar{F}(\bar{X}_{\mathrm{j}})$ [104]. This conversion impacts the dimensionality of the problem, as each slack variable is also added to the vector of free variables, $\bar{X}_{\text{j}}$, as follows:

$$
\begin{aligned}
T_{\text{i}} - T_{max}\sin^2(\eta_{T_{\text{i}}}) = 0 \quad &, \quad t_{\text{i}} - \eta_{t_{\text{i}}} = 0 \\
\alpha_{\text{i}} - 2\boldsymbol{\pi}\sin^2(\eta_{\alpha_{\text{i}}}) = 0 \quad &, \quad \beta_{\text{i}} - \boldsymbol{\pi}\sin^2(\eta_{\beta_{\text{i}}}) = 0 \\
\tau_D - \mathbb{P}_D\sin^2(\eta_{\tau_D}) = 0 \quad &, \quad \tau_A - \mathbb{P}_A\sin^2(\eta_{\tau_A}) = 0
\end{aligned}
\tag{4.13}
$$

where $\eta_{T_{\text{i}}}$, corresponds to the slack variable related to the thrust magnitude for arc i; $\eta_{t_{\text{i}}}$ is the slack variable associated with the integration time along segment i; $\eta_{\alpha_{\text{i}}}$ and $\eta_{\beta_{\text{i}}}$ are the slack variables related to the thrust orientation vector along the ith arc; η_{τ_D} and η_{τ_A} correspond to the slack variables associated with the time-like parameters, τ_D and τ_A, that represent the coast segments along the departure and arrival orbits[14]; and, finally, the variables $\mathbb{P}_D$ and $\mathbb{P}_A$ are evaluated as the orbital period of the departure and arrival orbits, respectively.

The Jacobian matrix, $DF(\bar{X}_{\text{j}}) = \frac{\partial F(\bar{X}_{\text{j}})}{\partial \bar{X}_{\text{j}}}$, is constructed either analytically or via finite difference numerical derivatives. Once a feasible solution is generated, it serves as an initial guess for a direct optimization procedure as implemented in MATLAB's fmincon optimization function. The objective is the minimization of the performance function specified in Equation (4.2), subject to:

$$
\begin{aligned}
\text{the differential constraints} \quad & \ddot{x} = 2\dot{y} + U_x^* + \frac{T}{m} cos\,(\alpha)\, cos\,(\beta) \\
& \ddot{y} = -2\dot{x} + U_y^* + \frac{T}{m} \sin\,(\alpha)\, cos\,(\beta) \\
& \ddot{z} = U_z^* + \frac{T}{m} \sin\,(\beta) \\
& \dot{m} = -\frac{T^2}{2P} \\
\text{the prescribed conditions} \quad & \bar{x}_0 = \bar{x}_D,\, m_0 = 1,\, t_0 = 0,\, N_0, \bar{x}_n = \bar{x}_{\tau_A} \\
\text{the inequality constraints} \quad & 0 \leq T_1 \cdots T_{n-1} \leq T_{max},\, t_1 \cdots t_{n-1} > 0 \\
& 0 \leq \alpha_1 \cdots \alpha_{n-1} \leq 2\boldsymbol{\pi},\; -\boldsymbol{\pi}/2 \leq \beta_1 \cdots \beta_{n-1} \leq \boldsymbol{\pi}/2 \\
& 0 \leq \tau_D \leq \mathbb{P}_D,\, 0 \leq \tau_A \leq \mathbb{P}_A \\
\text{and the path constraints} \quad & \bar{x}_1 = \bar{x}_{\tau_D},\, \bar{x}_2 = \bar{x}_1^t,\; \cdots,\, \bar{x}_n = \bar{x}_{n-1}^t
\end{aligned}
\tag{4.14}
$$

where $\bar{x}_{\mathrm{j}}$ vectors (for $\mathrm{j} = 1, .., n$) correspond to the states at the beginning of each arc segment, and $\bar{x}_{\mathrm{j}}^t$ represent the states at the termination point on that particular segment. To ensure that the spacecraft departs and arrives at the specified destination and arrival orbits, two time-like parameters, τ_D and τ_A, are introduced into the multiple shooting algorithm as additional constraint variables to enforce coast arcs along the orbits of interest. Note that, in this strategy, τ_D is propagated forward in time, while τ_A is propagated backwards on the destination orbit.

4.4 Transition from CR3BP-LT to the Ephemeris Model

There exist multiple strategies to transition a sliding solution from the CR3BP-LT to the ephemeris model, two of which are explored in this investigation. Strategy I: using the sliding algorithm, generate a converged locally optimal trajectory in the CR3BP-LT model; transition the full solution to the ephemeris model by transforming each position, velocity, and thrust orientation state from rotating to inertial coordinates; correct —and possibly optimize— in the ephemeris model [105]. The transfer in Figure 4.16(a) is a locally optimal solution generated from the sliding algorithm in the CRTBP-LT model. Strategy I dictates that this transfer be transformed into inertial coordinates, and later re-converged using a higher-fidelity ephemeris model, with a goal that the transfer geometry be generally preserved, as illustrated in Figure 4.16(b).

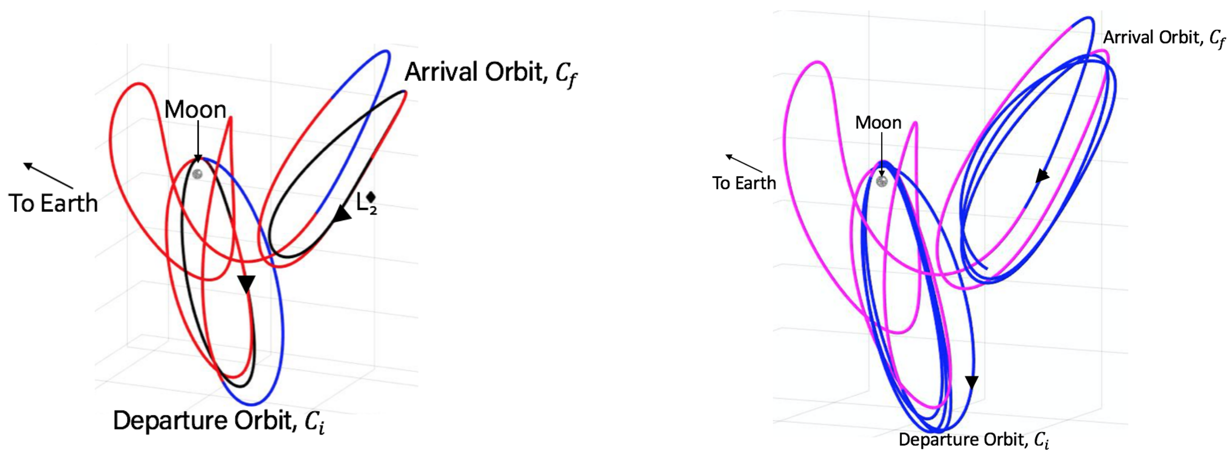

(a) L_2 S NRHO to L_2 N Halo Transfer in the CRTBP-LT via Sliding Algorithm.

(b) L_2 S NRHO to L_2 N Halo Transfer in the Ephemeris Model via Strategy I.

Figure 4.16. Strategy I for Constructing Sliding Geometry Transfers in the Ephemeris Model. Red and Blue Arcs Represent Thrust and Coast Segments in the CR3BP-LT model; Magenta and Cyan correspond to Thrust and Coast Segments in the Ephemeris Model

Strategy II: using the sliding algorithm, populate the initial guess for the minimum number of intermediate orbits necessary to slide through the family from the departure to the destination orbit; transform the position and velocity states for each intermediate periodic orbit into inertial coordinates; specify the thrust orientation vector control law with inertial pointing; correct —and possibly optimize— in the ephemeris model. Figure 4.17(a) is a visual representation of the initial guess that is generated by the sliding algorithm, describing the minimum number of intermediate orbits to accomplish the transfer. Transitioning these individual periodic orbits into the ephemeris model and, then, using a corrections algorithm to compute a converged trajectory, is the procedure from Strategy II that produces the path in Figure 4.17(b).

The ephemeris trajectory in Figure 4.16(b) preserves the geometry of the CR3BP-LT transfer utilized as initial guess in Strategy I; whereas, the ephemeris path in Figure 4.17(b), includes multiple revolutions of each intermediate CR3BP orbit member, as generated by the

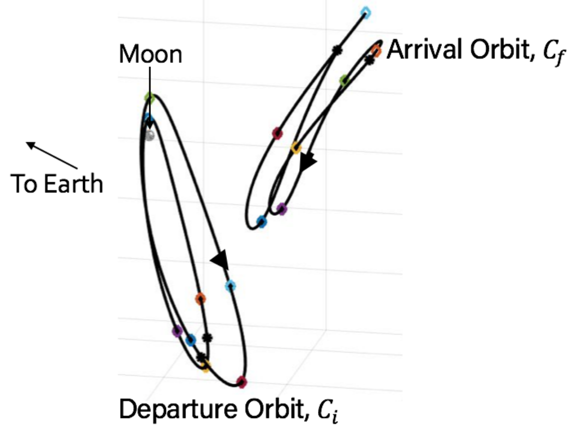

(a) L_2 S NRHO to L_2 N Halo Initial Guess in the CRTBP-LT from Sliding Algorithm.

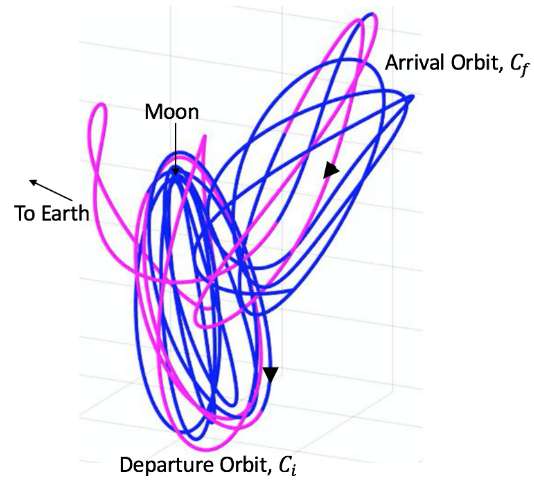

(b) L_2 S NRHO to L_2 N Halo Transfer in the Ephemeris Model via Strategy II.

Figure 4.17. Strategy II for Constructing Sliding Geometry Transfers in the Ephemeris Model. Magenta and Cyan correspond to Thrust and Coast Segments in the Ephemeris Model

sliding algorithm in the construction of the initial guess for Strategy II. Thus, the time-of-flight required for the spacecraft to travel from the departure to the arrival orbit in Strategy II, 164.7831 days, is larger than the travel time required in Strategy I, of 50.3245 days.

Regardless of the strategy, converging a trajectory in the ephemeris model is an epoch dependent problem. Depending on the position of the Sun as well as the other perturbing bodies added to the model at a specific epoch, the sensitivity of the problem might change, causing the corrections algorithm to increase the number of iterations to produce a converged solution. To alleviate convergence issues based on epoch dependencies, the concept of a roughness parameter is implemented to increase the probability of convergence for a particular epoch.

4.4.1 Roughness Parameter Technique

One of the main challenges in the design of spacecraft transfer trajectories in the ephemeris model, is the selection of the initial epoch. Since the ephemeris model is a time-dependent system, in which the position of the celestial bodies is no longer assumed to be static (as it is the case for simplified force models), the epoch plays an important role as it dictates the correct phasing of the gravitational bodies in the dynamical model; Thus, selecting the correct epoch may aid in the convergence of a transfer solution; however, the efficiency of the corrections algorithm can decrease by selecting an epoch with the wrong phasing.

To reduce the sensitivity of the trajectory convergence in the ephemeris model to the initial epoch, the concept of a Roughness Parameter (RP) is introduced. In its pure mathematical definition, the roughness parameter is a quantity used to assess the smoothness of a curve [106]. The smoothness is quantified by measuring the discontinuities along the path. A fully continuous path should yield a null RP and, as the path evolves into a piecewise continuous function, the RP value should increase. Thus, as discontinuities emerge, the RP value grows larger than zero.

In astrodynamics applications, the roughness parameter calculation is utilized in the generation of spacecraft trajectories in the ephemeris model [107]. There are multiple ways to compute the RP value and the method selected depends on the type of variations, or the characteristics of the path, to be assessed. Assume that position is potted as a function of time. If the vertical characteristics of the profile are desired, then amplitude roughness parameters are employed. If instead, the horizontal characteristics of the profile are sought, spacing roughness parameters are more useful. Lastly, a combination of vertical and horizontal characteristics of a profile can be evaluated by computing a hybrid roughness parameter.

In this investigation, the Root Mean Square (RMS) value of the profile for the magnitude of the position vector of the spacecraft relative to the central body, is employed as the roughness parameter measure. The process for leveraging this RP concept within the ephemeris model is accomplished as follows:

1. Stack a specified number of revolutions on the initial and final orbits in the CR3BP-LT model

2. For a selected initial epoch, transform the converged CR3BP-LT position, velocity and thrust orientation vector states into inertial coordinates, to generate an inertial initial guess

3. Propagate the trajectory initial guess in the ephemeris model, and discretize it into a finite number of points

4. Compute the magnitude of the ephemeris position vector of the spacecraft relative to the central body as illustrated in Figure 4.18

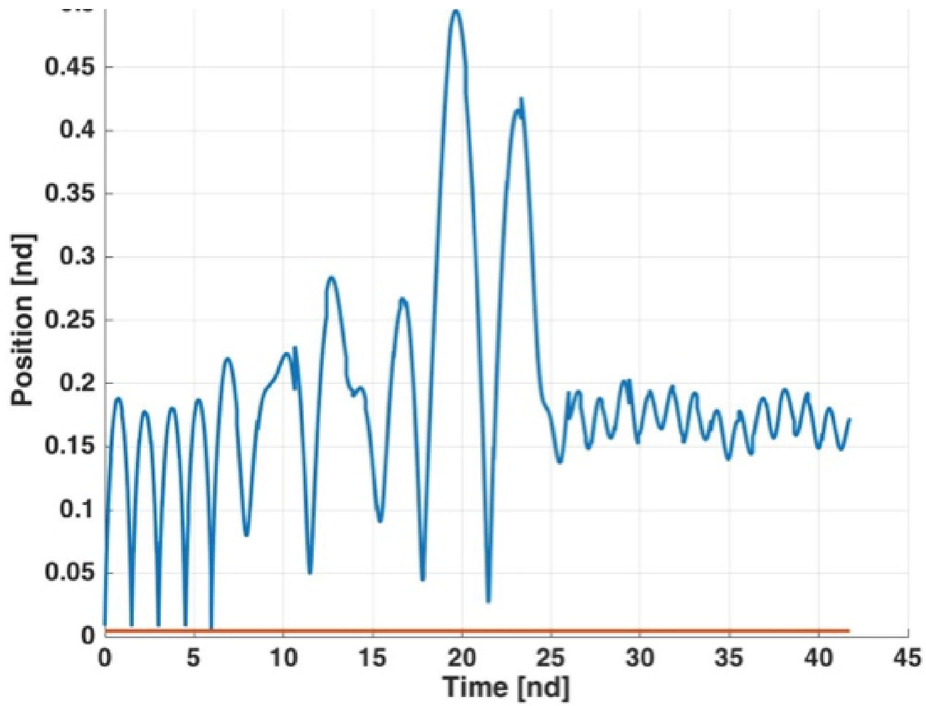

Figure 4.18. Sample profile for the magnitude of the position vector of a spacecraft relative to the Moon, in a higher-fidelity ephemeris model, for a selected initial epoch. The red line represents the lunar radius

5. Compute the roughness parameter value (RMS) corresponding to that particular trajectory and epoch; store each value

6. Repeat steps 1 through 5 for a variety of different epochs, and for various numbers of stacked revolutions, to generate the map in Figure 4.19 denoted the Roughness Parameter Map (RPM)

7. Use the RPM to select the combination of epoch and number of stacked revolutions with the lowest RMS value; use a corrections algorithm to converge this initial guess for the selected variables in the ephemeris model

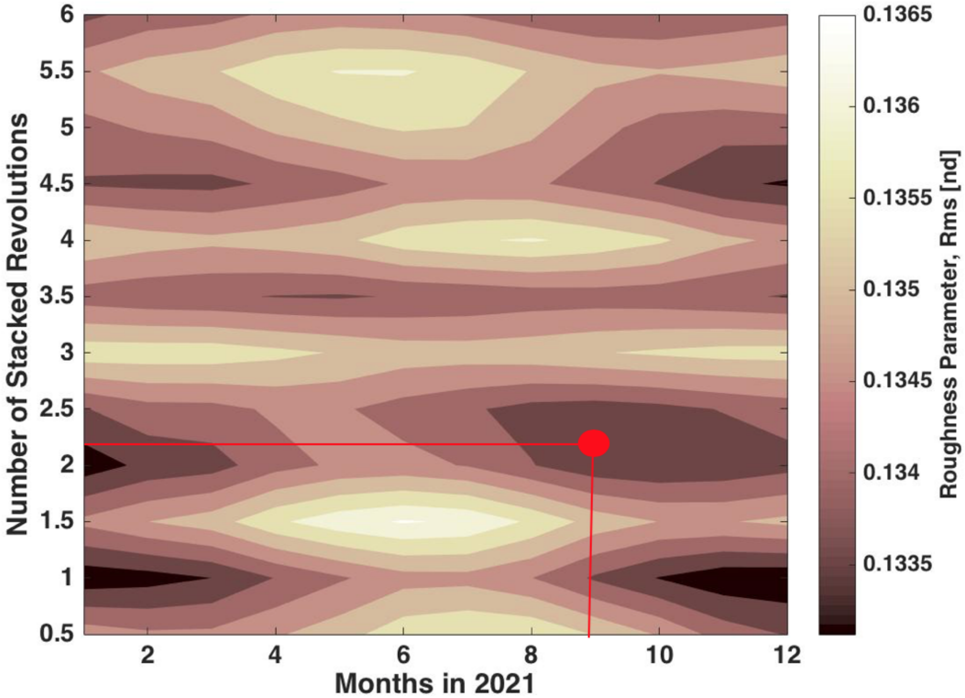

Figure 4.19. Sample RPM map for epoch selection when transitioning from the CR3BP-LT to the ephemeris model

8. If a specific epoch is desired for the ephemeris trajectory, apply a natural parameter continuation process on the epoch converged in Step 7; re-converge the solution until the specified epoch is achieved

Figure 4.18 depicts a sample representation for the magnitude of the position of a spacecraft in the vicinity of the Moon. The RMS value for this position profile is simply computed as:

$$R_{ms} = \sqrt{\frac{1}{k}\sum_{\mathrm{i}=1}^{k} p_{\mathrm{i}}^2} \tag{4.15}$$

where k represents the number of discretization points in the profile, and $p_{\mathrm{i}}, (\mathrm{i} = 1, ..., k)$ corresponds to the parameter of interest at point i. The RMS value is straightforward to evaluate.

While the RMS quantity is one of the most popular amplitude roughness parameter measures, there exist other options for amplitude parameters, for example, the maximum height of the profile, the amplitude density function, or the power spectral density function. Some of the most popular spacing roughness parameters include the measure of the number of peaks in the profile, and the number of inflection points.

5. APPLICATIONS

A near-term goal for the expansion of activities in the Earth-Moon neighborhood is the capability to maintain a facility near the Moon that serves as a staging node for excursions to other cislunar destinations. Support for low-thrust vehicles in this dynamically sensitive region include functional requirements that depend upon the scientific mission constraints and on the limitations introduced by the physical capabilities of the spacecraft. The applications described in this investigation offer an adaptive strategy for generating locally optimal solutions for low-thrust spacecraft in the lunar vicinity, by exploiting the energy parametrization of multi-body families of orbits. Results are validated in a higher-fidelity ephemeris model and are demonstrated for a variety of transfers with a wide range of thrust acceleration levels. The methodology proves successful for achieving large orbital plane changes evolving entirely within the lunar vicinity, as well as for generating suitable initial guesses for long spiral transfers approaching low lunar orbits.

5.1 Cislunar Low-Thrust Transfers Between Libration Point Orbits

The adaptive sliding algorithm in the CR3BP-LT model is employed to generate a variety of transfers in the cislunar region that, combined with the roughness parameter procedure, generates higher-fidelity interior and exterior geometry solutions. The acceleration levels considered in this investigation are consistent with those flown in previous missions, as represented in Table 5.1. An interesting fact is the realization that larger spacecraft initial mass do not necessarily signify larger a thrust acceleration level. On the contrary, the magnitude of the thrust acceleration is dictated by the thrust force to mass ratio given by Equation 2.63.

Table 5.1. Low-Thrust Parameters for Previously Flown Missions

Mission	$a_{T_{max}} [m/s^2]$	**Initial Mass** $[kg]$
Deep Space 1	1.91×10^{-4}	486.3
Dawn	7.47×10^{-5}	1217.8
Hayabusa 2	4.44×10^{-5}	608.6

It has been demonstrated by previous authors that the smaller the acceleration level of the low-thrust engine, the more challenging it is to design transfers for those spacecraft, since the time required to modify the energy level of the current path of the vehicle is larger for smaller engines. To overcome some of these challenges, a natural parameter continuation method is employed on the thrust acceleration magnitude of the spacecraft, such that, a low-thrust transfer is first computed for a high value of the thrust magnitude; this converged solution is then utilized as an initial guess for a second low-thrust transfer for which the maximum allowed thrust acceleration magnitude is reduced. The process continues until the constraint on the desired value of the thrust acceleration level is achieved.

5.1.1 Mass-Optimal Interior Transfer from a L_2 Lyapunov to a L_2 Vertical Orbit

To illustrate the performance of the sliding algorithm consider the design of a low-thrust transfer with a sliding-type geometry for a 500 kg spacecraft from a L_2 Lyapunov orbit with the energy level $JC = 3.0001$ to an L_2 vertical orbit with energy $JC = 2.7172$ in the Earth-Moon CR3BP system, with a maximum thrust acceleration level of $4 \times 10^{-4} m/s^2$. The biggest challenge when designing this transfer is the large change in the inclination between the two families; thus, it is beneficial to leverage one or more orbits from an intermediate family to gradually alter the inclination of each intermediate orbit and, thus, accomplish the sliding type transfer. The inputs to the sliding algorithm are then the departure and arrival orbits, the maximum thrust acceleration level allowed by the spacecraft, and the inclusion of an intermediate family of orbits.

As apparent in Figures 5.1 the algorithm proceeds to generate the energy parametrization for each of the individual families, as this parametrization is the key factor for later selection of the individual orbits to incorporate as the intermediate arcs along the transfer. Figures 5.1(a) and 5.1(b) correspond to the spatial configuration of each orbit member of the Lyapunov and vertical families respectively; Figures 5.1(c) and 5.1(d) are a parametrization of the Jacobi constant value versus the orbital period for each orbit member; Figures 5.1(e) and 5.1(f) are the energy surfaces generated by the sliding algorithm for each family of interest.

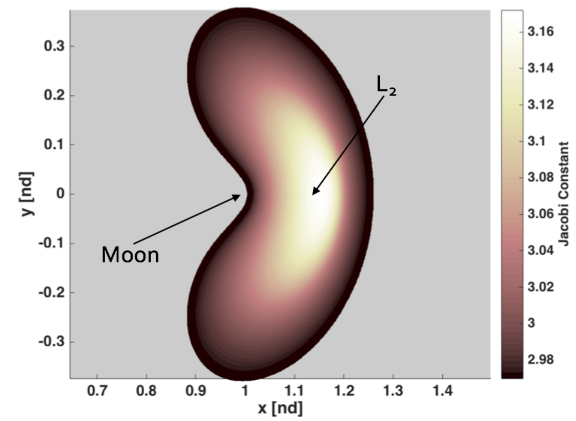

(a) L_2 Lyapunov Configuration Space.

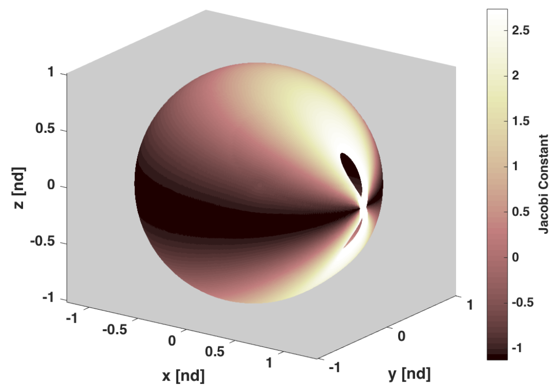

(b) L_2 Vertical Configuration Space.

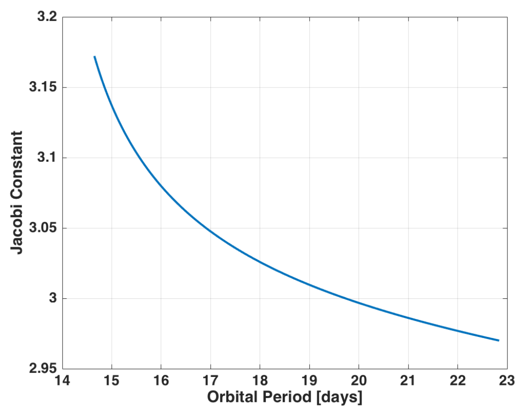

(c) L_2 Lyapunov Energy Evolution.

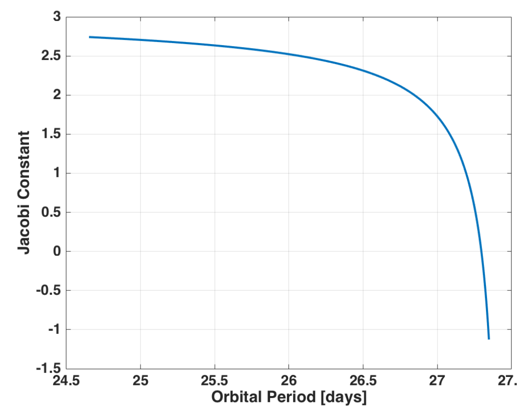

(d) L_2 Vertical Energy Evolution.

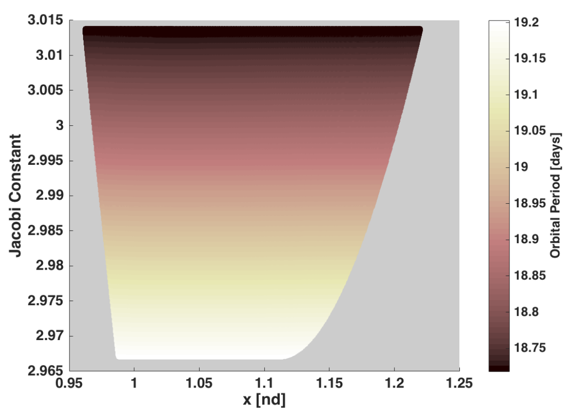

(e) L_2 Lyapunov Energy Surface.

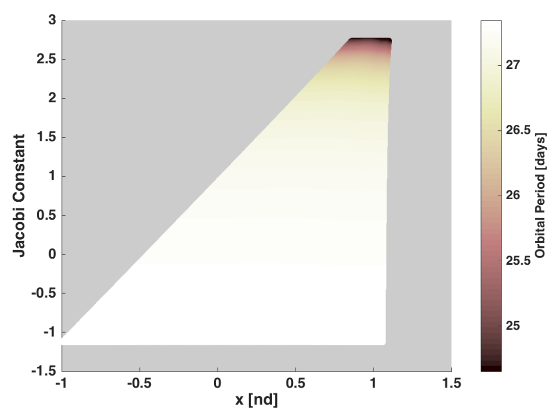

(f) L_2 Vertical Energy Surface.

Figure 5.1. Energy Parametrization for the L_2 Lyapunov and L_2 Vertical Families of Orbits

Both of these families exert monotonic behaviour on the energy parametrization, which suggest that there exist only one energy level —one value of Jacobi constant— for each individual member in each family. The monotonic growth of the energy surfaces does make the selection of the intermediate arcs a straightforward process on the sliding algorithm, that, based on the reach of the maximum thrust acceleration magnitude of the spacecraft, performs a grid search in one direction to gradually increase the energy level from the Lyapunov orbit to that of the arrival vertical orbit. Furthermore, based on the evolution of each member of the L_2 axial family depicted in Figure 5.2, its energy span, and its 'reach' in z-amplitude, this additional family is selected for inclusion. Note that the selection of an intermediate family is arbitrary. However, an informed choice is beneficial.

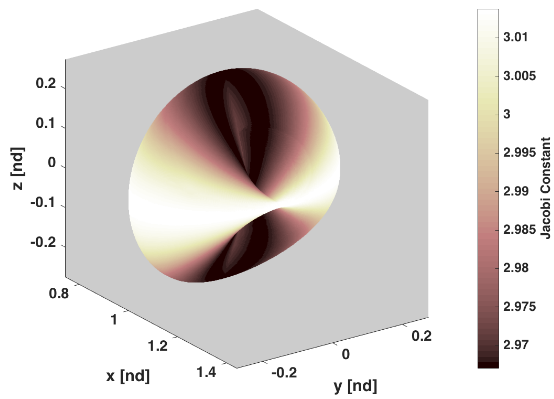

(a) L_2 Axial Configuration Space.

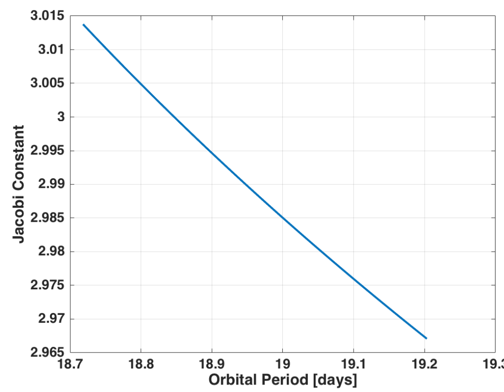

(b) L_2 Axial Energy Evolution.

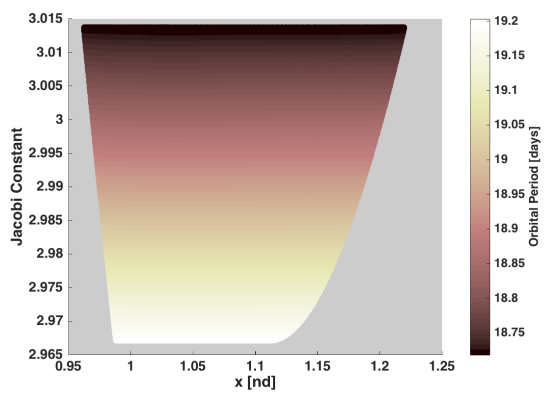

(c) L_2 Axial Energy Surface.

Figure 5.2. Energy Parametrization for the L_2 Axial Family of Orbits

After the energy parametrization of each family of interest is completed, the adaptive sliding algorithm proceeds to generate the initial guess plotted in Figure 5.3(a); the algorithm selects one orbit from the Lyapunov family —the departure orbit—, one orbit form the vertical family —the arrival orbit—, and six orbits from the axial family. The initial guess is subjected to the corrections algorithm and energy-informed minimization problem detailed in Section 4.2, from which the converged mass-optimal solution in the CR3BP-LT model depicted in Figure 5.3(b) is obtained. As expected, the final transfer resembles the geometry of the initial guess, where blue and red arcs represent coast and thrust arcs in the CR3BP-LT model;

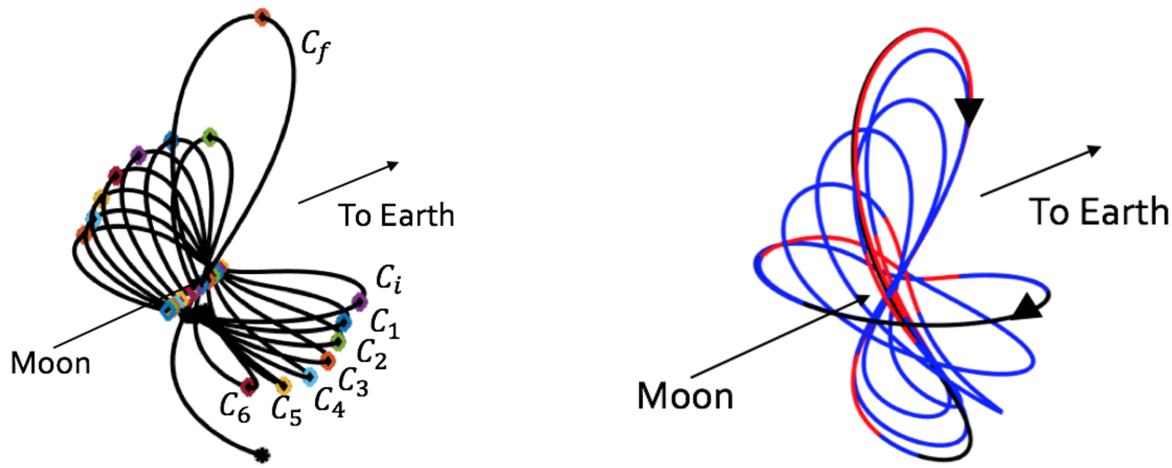

(a) CR3BP-LT Initial Guess

(b) CR3BP-LT Converged Transfer.

Figure 5.3. Performance for a Mass Optimal Interior LT Transfer from a L_2 Lyapunov to a L_2 Vertical via L_2 Axial in the CR3BP-LT Model

The energy evolution and the thrust acceleration levels in the converged solution in the CR3BP-LT model are detailed in Figure 5.4. In this model, the spacecraft requires 132.9845 days from the time of departure from the initial orbit (represented in Figure 5.3 as the first thrusting arc) until the time it arrives on the destination orbit (i.e., the last thrusting arc). The spacecraft arrives at its final destination with 99.1754% of its initial mass, thus, only 0.8246kg of the 500kg initial mass was expended for the transfer. Converting this performance to an equivalent ΔV results in $324.7892 m/s$ of propellant consumption, which is within the range of the theoretical minimum ΔV required for motion from the departure to the destination orbits represented in Figure 5.5.

Following the strategy in Section 4.4, the converged solution from the CR3BP-LT model is utilized as the initial guess for the corrections algorithm in the Sun-Earth-Moon (SEM)

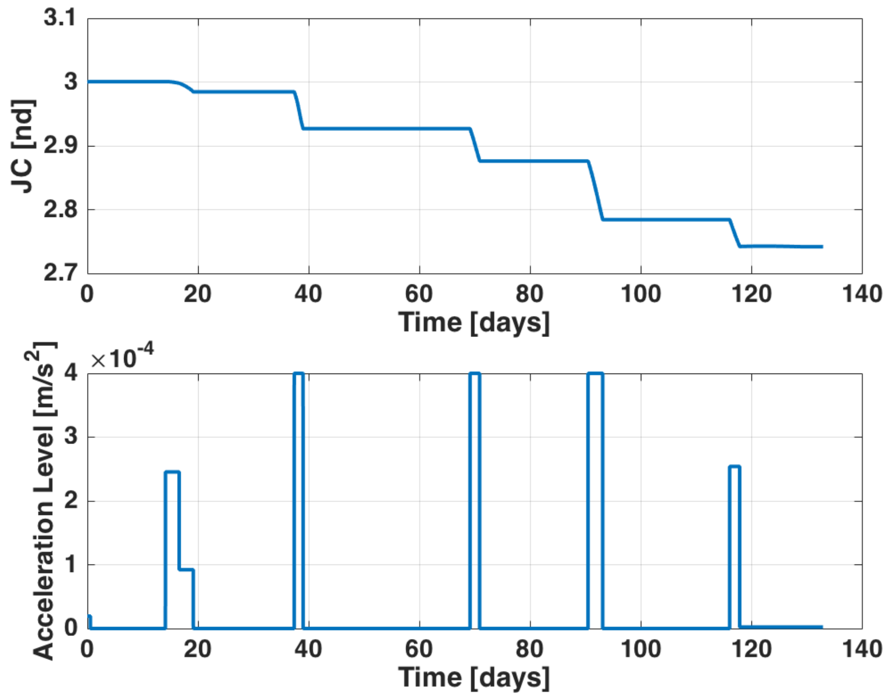

Figure 5.4. CR3BP-LT Energy and Acceleration Evolution

ephemeris model to generate the mass-optimal trajectories illustrated in Figure 5.6, where cyan and magenta segments correspond to coast and thrust arcs, respectively. In this model, only the point mass gravitational perturbations of the Sun, the Earth and the Moon, are included. The transition process follows Strategy I from Section 4.4, for which the converged solution in the CR3BP-LT model is augmented by multiple revolutions of the departure and arrival orbits.

Figure 5.6(a) represents the converged mass-optimal trajectory as viewed in a J2000 inertial frame centered at the Moon; Figure 5.6(b) is an inertial view from an observer centered at the Earth; Figure 5.6(c) is the view in the ecliptic frame from an observer centered at the Moon. The departure epoch is selected based on the roughness parameter map illustrated in Figure 5.7, for which March 1, 2021 is selected.

For this particular epoch in the SEM ephemeris model, the equivalent ΔV consumption is reduced to $292.6643 m/s$, that corresponds to 0.9981% of the 500kg initial mass, while the total time-of-flight required is 117.7946 days. Recall, since the ephemeris model is a time-

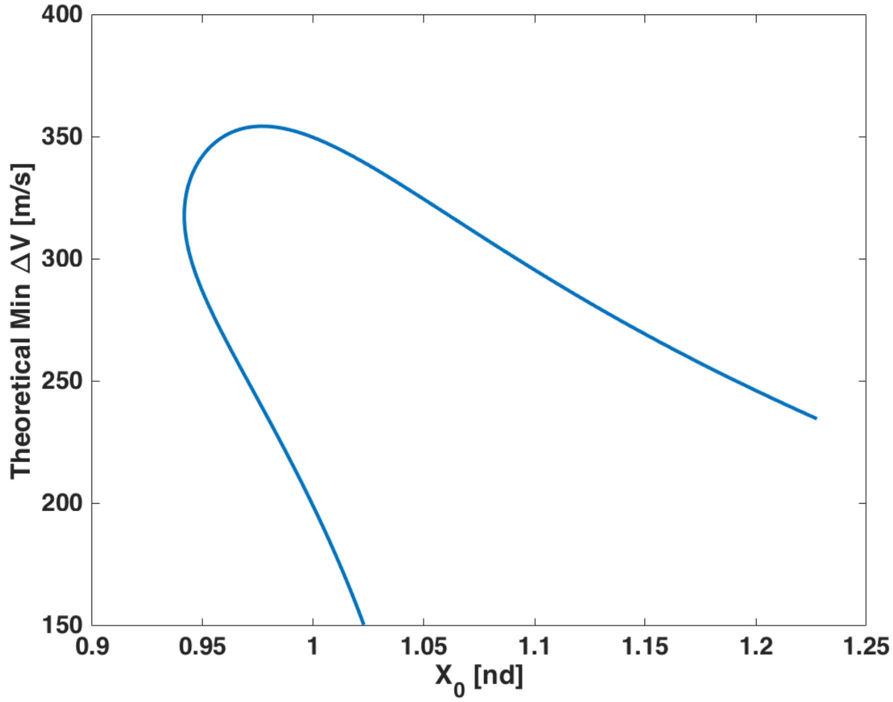

Figure 5.5. Theoretical Minimum ΔV.

dependent system, the propellant consumption does vary with the epoch selected, suggesting that, the performances reported in this investigation might increase or decrease depending on the position of the celestial bodies at each instant of time.

5.1.2 Time-Optimal Transfer from a L_2 Lyapunov to a L_2 Vertical Orbit

To illustrate the effects of the maximum thrust acceleration magnitude on the trajectory design framework, consider re-designing the low-thrust transfer for a 500 kg spacecraft with a maximum thrust acceleration level of $4 \times 10^{-4} m/s^2$, from a $JC = 3.0001$ L_2 Lyapunov orbit to a $JC = 2.7172$ L_2 vertical orbit in the Earth-Moon CR3BP system, as a time-optimal solution. The adaptive sliding algorithm proceeds to modify the weights on the objective function in Equation (4.2), such that priority is shifted to the time-of-flight minimization term.

To initiate the design, the process utilizes the initial guess illustrated in Figure 5.10. The converged time-optimal solution produced by the adaptive sliding algorithm is plotted

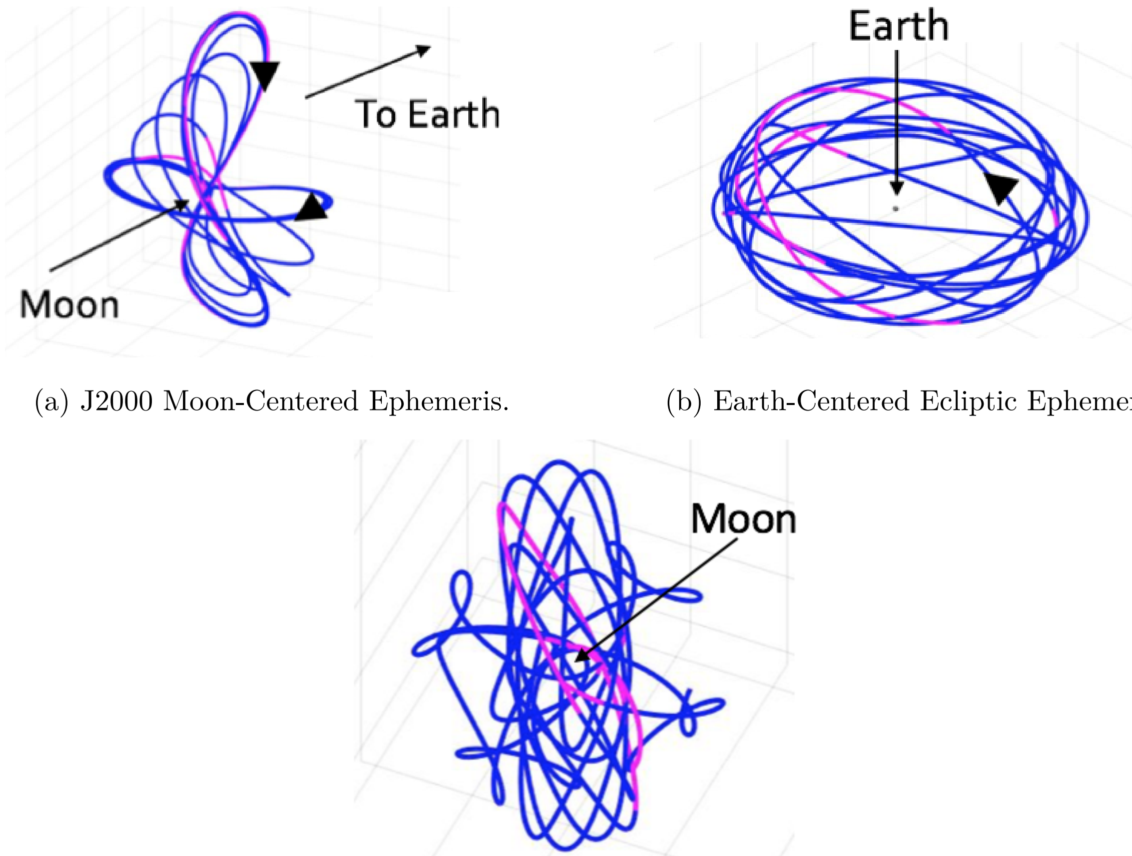

(a) J2000 Moon-Centered Ephemeris. (b) Earth-Centered Ecliptic Ephemeris.

(c) Moon-Centered Ecliptic Ephemeris.

Figure 5.6. Performance for a Mass Optimal Interior LT Transfer from a L_2 Lyapunov to a L_2 Vertical via L_2 Axial in the SEM Ephemeris Model

in Figure 5.10, while the energy and time-of-flight evolution are represented in Figure 5.11. Comparing these two locally optimal solutions (i.e., the mass-optimal solution in Figures 5.3 and the time-optimal solution in Figures 5.10), the time-of-flight required for the spacecraft from departure to destination is reduced from 132.9845 days to 11.6653 days from the mass-optimal to the time-optimal solution; the propellant consumption, however, increases from 0.9981% to 1.0277% of the 500kg initial mass, that, in terms of equivalent ΔV, indicates that the mass consumption increases from 324.7892m/s in the mass-optimal case to 405.2372m/s in the time-optimal solution. These performances suggest that for this particular application, the time-optimal solution offers a suitable trade-off between transfer time and propellant cost

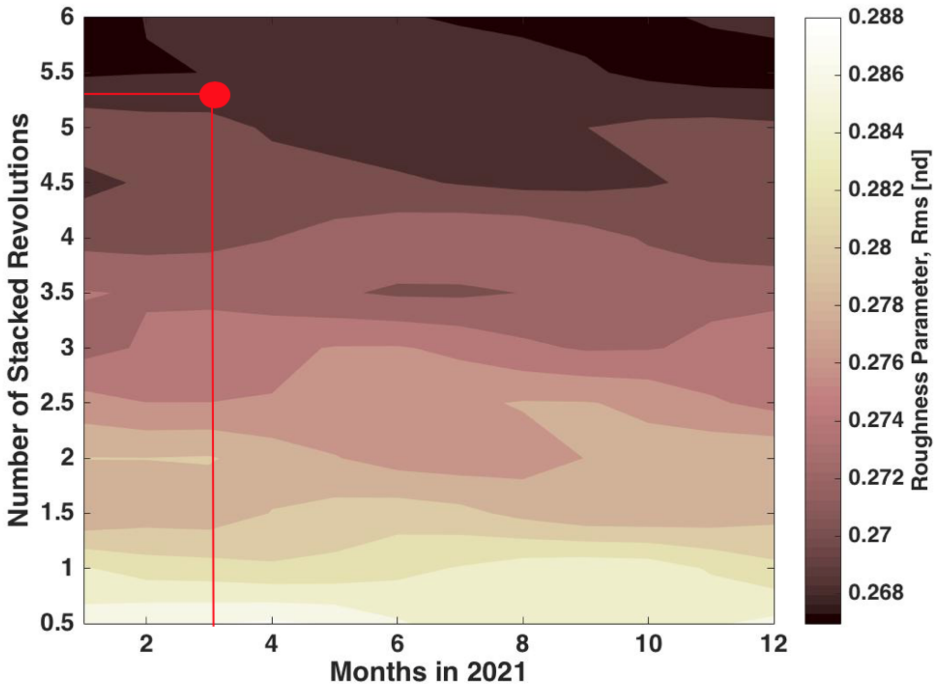

Figure 5.7. Roughness Parameter Map

benefits, as the penalty in increasing the cost is largely overshadowed by the reduction in travel time.

As a result of maintaining active thrusters over the entire duration of the trajectory, the energy evolution for the time-optimal transfer in Figure 5.11 is a smooth curve; alternatively, the energy evolution of the mass-optimal trajectory in Figure 5.5 exerts a staircase-like behaviour, reflecting the spacecraft passage through each intermediate orbit, to gradually accomplish the large change in inclination required to transition from a planar to a spatial orbit, while ensuring the least locally possible propellant consumption.

These time-optimal results are further examined via a natural parameter continuation procedure on the maximum thrust acceleration level experienced by the spacecraft, to produce a family of minimum time-of-flight solutions from departure to arrival orbit, as illustrated in Figure 5.10. As the maximum thrust acceleration level is gradually decreased from $4\times10^{-4}m/s^2$ to $2\times10^{-4}m/s^2$, an acceleration level consistent with that of the DAWN spacecraft, a new path is constructed by the adaptive sliding algorithm, and its representation in

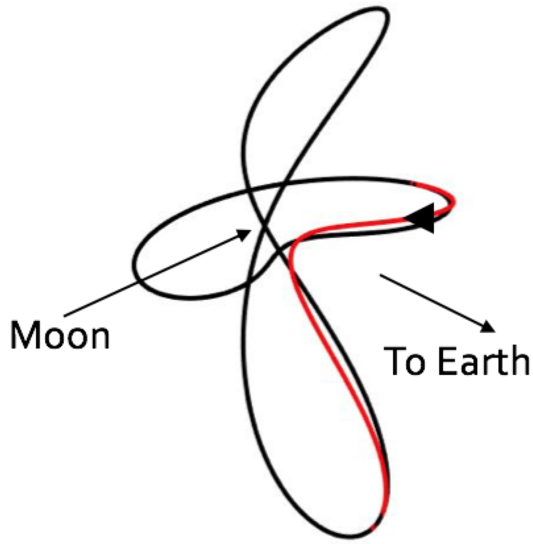

Figure 5.8. CR3BP-LT Converged Transfer

configuration space in plotted as a new lighter shade of the darker red trajectory in Figure 5.10.

Moreover, the time-of-flight and the equivalent ΔV performance for each trajectory are depicted in Figure 5.11, where it is apparent that as the thrust acceleration level decreases, the time-of-flight of the time-optimal solution generally increases, as well as the equivalent ΔV.

The results from the time-optimal solutions in Figures 5.10 and 5.11 are coherent within the context of the expected behaviour of the low-thrust spacecraft. If all other parameters remain fixed (e.g., departure and destination orbit, and engine specific impulse), the smaller the thrust acceleration level, the greater the time interval required for the vehicle to navigate the same region in space, and the more propellant-expensive the transfer.

5.1.3 Mass-Optimal Exterior Transfer from a L_2 Lyapunov to a L_2 Vertical Orbit

To illustrate the performance of the adaptive sliding algorithm in generating exterior-type trajectories, consider the design of a low-thrust transfer for a 500 kg spacecraft with a maximum thrust acceleration level of $4 \times 10^{-4} m/s^2$, from a L_2 Lyapunov orbit with energy $JC = 3.0001$ to a L_2 Vertical orbit with energy $JC = 2.7172$; it is assumed that an escape-

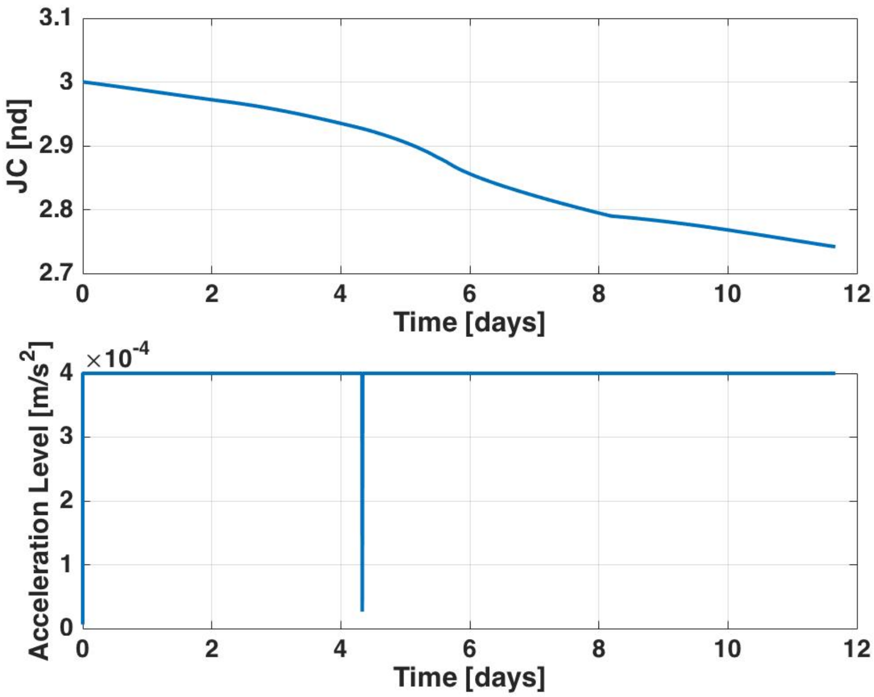

Figure 5.9. CR3BP-LT Energy and Acceleration Evolution. Performance for a Time Optimal LT Transfer from a L_2 Lyapunov to a L_2 Vertical via L_2 Axial in the CR3BP-LT Model

type geometry is sought to move the vehicle between these two particular orbits. Following the steps outlined in the algorithm in Figure 4.4, it is noted that both the L_2 Lyapunov and the L_2 Vertical families are unstable in the linear sense; therefore, an initial guess for this escape-type geometry is constructed by leveraging invariant manifolds from each of the periodic orbits. The branches from the stable and unstable manifolds are depicted in Figure 5.12, where the blue and cyan trajectories correspond to branches of the stable manifolds, while red and magenta represent flow from the unstable branches, respectively. A hyperplane is selected according to the procedure described in Section 4.1.1, such that, the crossings from each of the manifold branches are recorded in a Poincaré map as illustrated in Figure 5.13.

From the Poincaré map analysis, the algorithm proceeds to generate the initial guess for the transfer depicted in Figure 5.14(a), while the converged solution appears in Figure 5.14(b). The final transfer resembles the expected exterior geometry of the initial guess. Blue arcs represent coast arcs, while the red segments correspond to the times for which

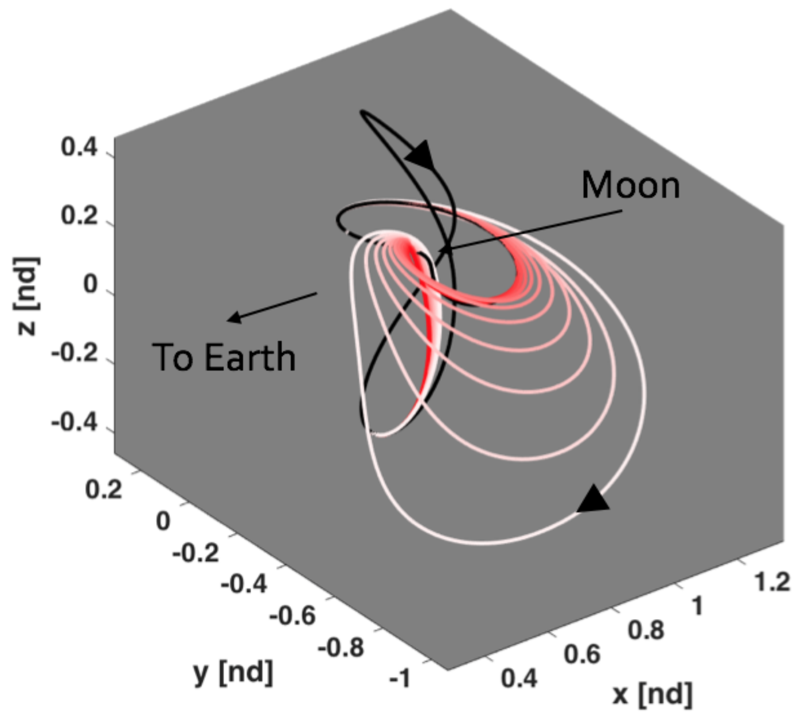

Figure 5.10. CR3BP-LT Time-Optimal Family of Solutions

the low-thrust engine is turned on. The energy evolution and thrust acceleration of the converged solution are represented in Figure 5.14(d). The spacecraft requires 124.0840 days to travel from departure (represented in Figure 5.14 as the first thrusting arc) to arrival on the destination orbit. The transfer expends 0.6904kg of the 500kg initial mass, which corresponds to an equivalent ΔV of 271.7434m/s. Comparing this propellant performance to the theoretical minimum ΔV required to travel from the departure to the destination orbit in Figure 5.14(c), suggest that this trajectory corresponds to a mass-optimal solution.

5.1.4 Mass-Optimal Interior Transfer from a L_2 Southern (S) NRHO to a L_2 Northern (N) NRHO

To illustrate the performance of the sliding algorithm, consider a sliding-type low-thrust transfer for a 14 kg spacecraft with a maximum acceleration level of $8 \times 10^{-5} m/s^2$, from a L_2 Southern Near Rectilinear Halo Orbit (NRHO) with energy $JC = 3.0553$ to a L_2 Northern NRHO with energy $JC = 3.0441$ in the Earth-Moon CR3BP-LT system. The energy parametrization for both families of interest appears in Figures 5.15 and 5.16, respectively.

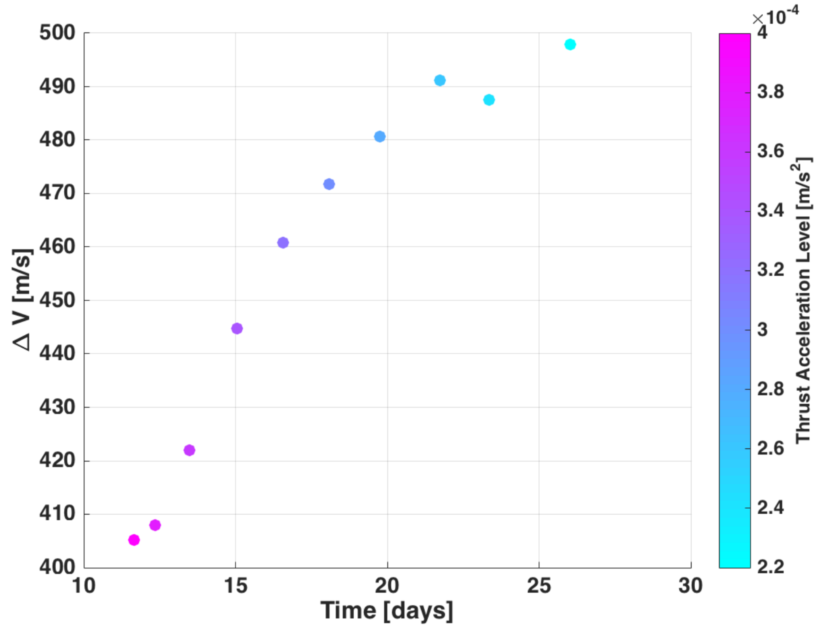

Figure 5.11. CR3BP-LT Cost and ToF Performance. Performance for a Time Optimal Family LT Transfer from a L_2 Lyapunov to a L_2 Vertical via L_2 Axial in the CR3BP-LT Model

Figures 5.15(a) and 5.16(a) represent the corresponding halo family of orbits in configuration space. Figures 5.15(b) and 5.16(b) are a representation of the Jacobi constant value of each orbit member of the family versus its orbital period; in both cases, i.e., for the northern and southern families, this energy parametrization depicts non-monotonic growth, such that, the value of the Jacobi constant for each orbit is not unique. The non-uniqueness of the energy of each individual orbit member of the Halo families is also assessed in the parametrization illustrated in Figures 5.15(c) and 5.16(c), in which, the energy surface for each individual family is represented.

Once the energy parametization is computed, the algorithm proceeds to perform a grid search to identify the individual intermediate orbits from each family to include in the initial guess of the transfer. The initial guess generated from the sliding algorithm in the CR3BP-LT model is plotted in Figure 5.17(a). The converged mass-optimal solution —that is, the output of the adaptive sliding algorithm— in the CR3BP-LT model, appears in Figure 5.17(b); blue and red arcs correspond to coast and thrust arcs in the CR3BP-LT model. The evolution of the energy and thrust acceleration level for the converged solution are

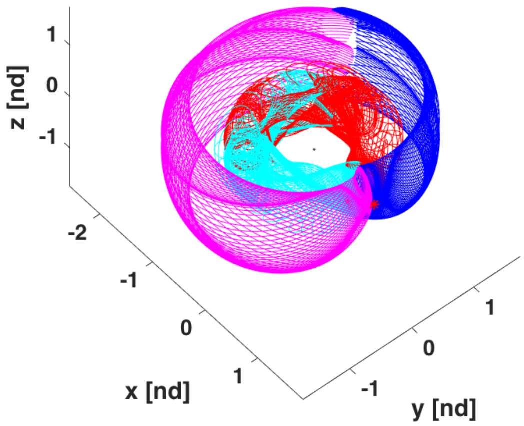

Figure 5.12. Manifold Branches of the L_2 Vertical Orbit

represented in Figure 5.17(d). Each horizontal segment in the Jacobi constant versus time plot represents the spacecraft coasting along one of the intermediate orbits; the acceleration level versus time plot demonstrates that the constraint on the maximum thrust magnitude that the spacecraft can achieve is never violated.

Utilizing the roughness parameter map illustrated in 5.18(a), the trajectory is transitioned to the ephemeris model for the selected epoch of September 1, 2021. The corresponding trajectories in different views of the Sun-Earth-Moon (SEM) ephemeris model are depicted in Figures 5.18(b)-5.18(d); cyan and magenta arcs represent coast and thrust segments in the ephemeris model, respectively.

In the CR3BP-LT model, the spacecraft requires 72.9701 days from the time it departs the original orbit (represented in Figure 5.17 as the first thrusting arc) until arrival on the destination orbit (i.e., the last thrusting arc). The transfer path requires about 0.0461kg (0.3335%) of the 14kg initial mass, which corresponds to an equivalent ΔV of 81.8931m/s. In the ephemeris model, for this particular epoch, the equivalent ΔV consumption increases to 103.1541m/s or 0.0588kg of the initial spacecraft mass, while the time-of-flight is reduced to 72.6896 days. Note that, since the performance in the ephemeris model is epoch dependent,

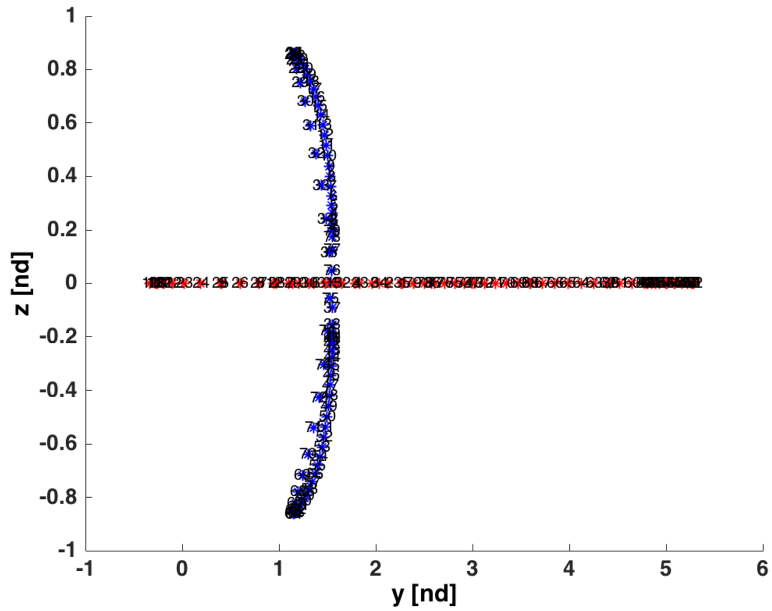

Figure 5.13. Poincaré Map for Stable and Unstable Manifold Branches of the L_2 Lyapunov and L_2 Vertical Orbits of Interest

the ΔV consumption is modified by re-converging this locally mass-optimal solution for a different time epoch.

To assess the performance of the solution, the propellant consumption is compared with the theoretical minimum ΔV estimated for this transfer, as illustrated in Figure 5.17(c). In terms of propellant consumption, note that the sliding algorithm produces a path more costly than the theoretical minimum. However, there exists a trade-off between reducing propellant cost, and producing a trajectory that, despite the highly dynamically sensitive region of space —such as the cislunar region— the spacecraft remains within the vicinity of the Moon over the entire duration of the transfer. Moreover, the sliding algorithm produces transfers leveraging the dynamical environment, even though the departure and arrival orbits are stable in the Lyapunov sense, i.e., they do not possess arcs that naturally depart and/or approach the periodic orbit.

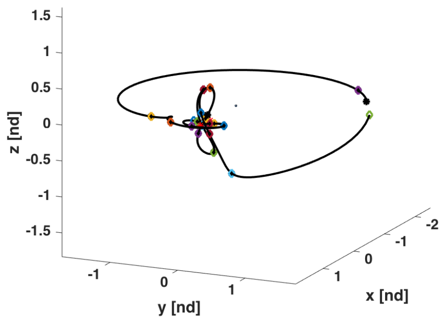

(a) CR3BP-LT Initial Guess

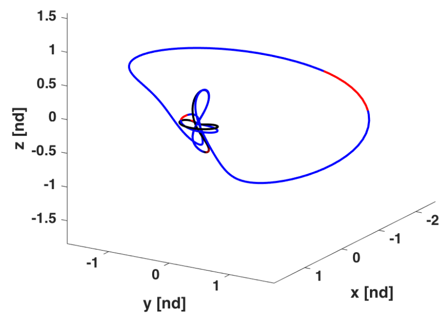

(b) CR3BP-LT Converged Transfer.

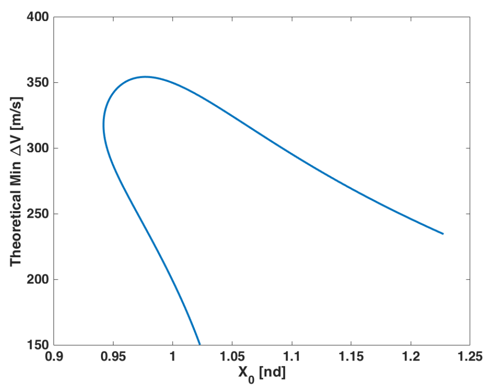

(c) Theoretical Minimum ΔV.

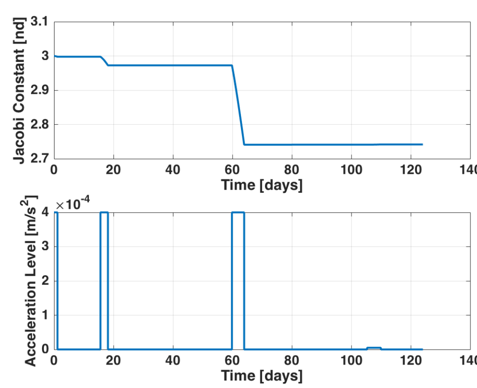

(d) CR3BP-LT Energy and Acceleration Evolution.

Figure 5.14. Performance for a Mass Optimal Exterior LT Transfer from a L_2 Lyapunov to a L_2 Vertical in the CR3BP-LT Model

5.2 Lunar IceCube Potential Mission Options

Upon deployment as a secondary payload from the Artemis-1 spacecraft, Lunar IceCube (LIC), a 6U CubeSat equipped with a 1.24mN maximum thrust engine [62], will transfer to an orbit in the lunar vicinity from which it will complete its primary science and technology demonstration objectives. The efficiency of LIC's low-thrust engine enables the spacecraft to pursue extended mission objectives; however, the low acceleration level available to LIC offers significant challenges for the design of orbits and transfers. This investigation suggests a framework for the construction of low-thrust transfers between multi-body orbits in the lunar vicinity for applications with the LIC acceleration level. Low-thrust transfers are computed

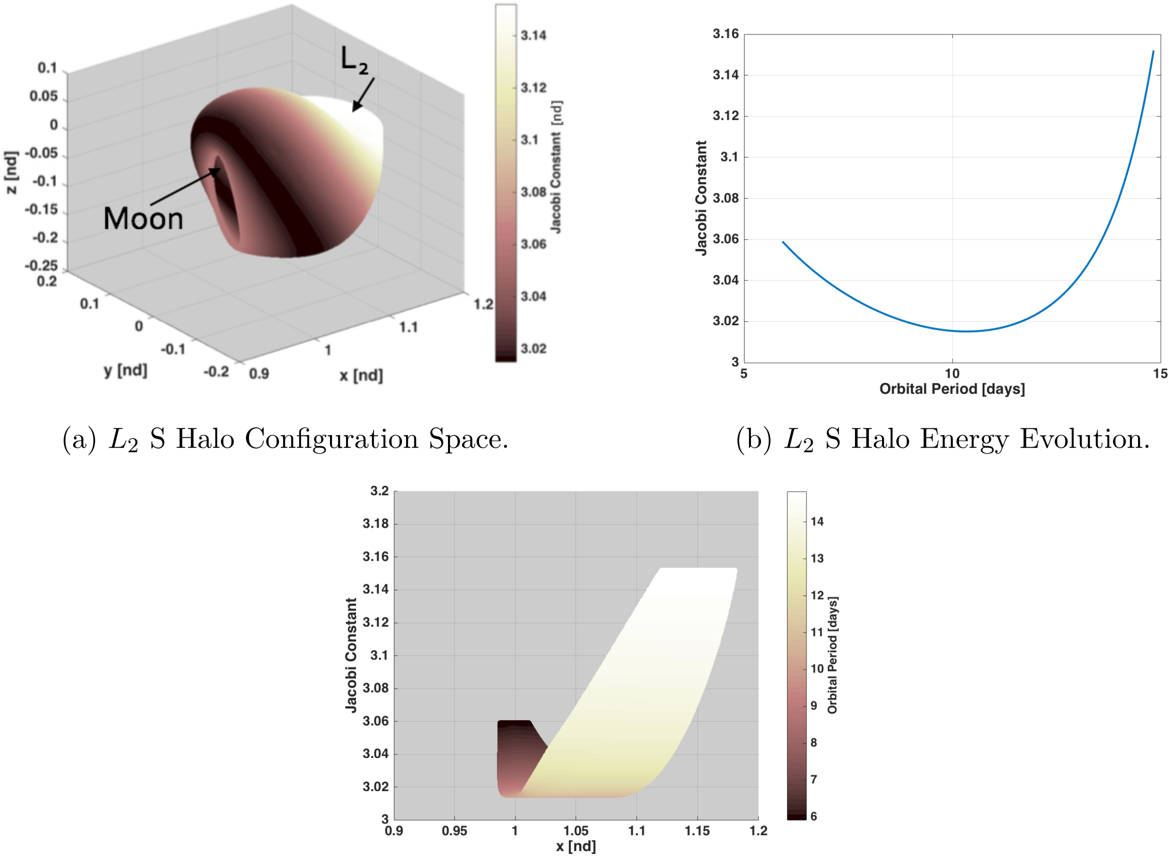

(a) L_2 S Halo Configuration Space.

(b) L_2 S Halo Energy Evolution.

(c) L_2 S Halo Energy Surface.

Figure 5.15. Energy Parametrization for the L_2 S Halo Families of Orbits

to and from a variety of multi-body orbits that exist in the vicinity of the Moon, e.g., Lyapunov, distant retrograde, and halo orbits. The proposed methodology offers a strategy applicable not only to the LIC mission but extendable to other low-thrust missions in the lunar vicinity, whether the acceleration capabilities are greater or less than LIC, particularly when science objectives, line of sight constraints, or orbital determination requirements, necessitate the use of multi- body orbits. Cost-time efficiency transfer performance is assessed that demonstrates the flexibility of the framework and delivers a new variety of mission options for the LIC spacecraft.

To develop a general framework for trajectory design for the Lunar IceCube (LIC) spacecraft, the process is divided into three phases; this division does not only facilitate the accommodation for modified Earth deployment state epochs in the primary mission, but

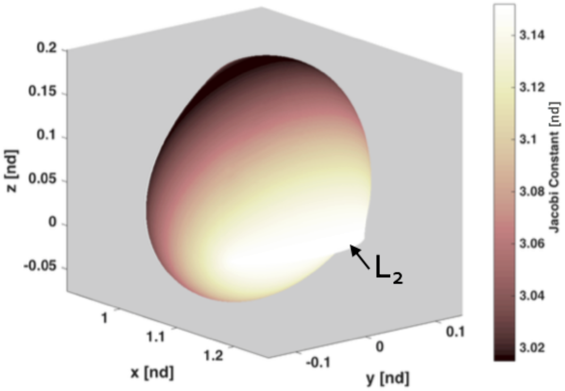

(a) L_2 N Halo Configuration Space.

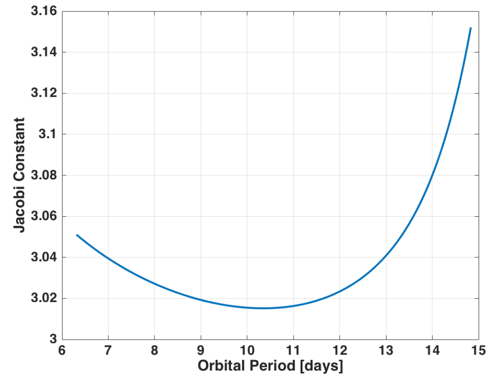

(b) L_2 N Halo Energy Evolution.

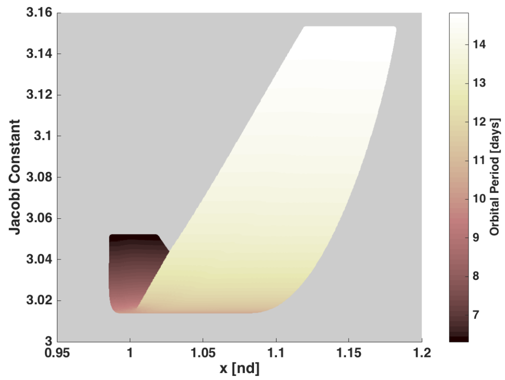

(c) L_2 N Halo Energy Surface.

Figure 5.16. Energy Parametrization for the L_2 N Halo Families of Orbits

also generalizes the search for extended mission applications that are independent of the arrival epoch of the LIC into its primary science mission orbit. The LIC's primary mission is comprised of phases I and II [105], while the potential extended applications are investigated in phase III [107].

After arriving on the science orbit dictated by the primary mission, the LIC is expected to remain in an L_2 S 9:2 NRHO performing its science and technology demonstrations. The examples and ephemeris epochs examined in this investigation assume that the spacecraft's propellant reserve to perform any potential extended mission application is of 13.6 kg at best.

By leveraging the natural structures that exist within the CR3BP model, and, utilizing an energy-informed adaptive algorithm to generate interior-type trajectories, a variety of

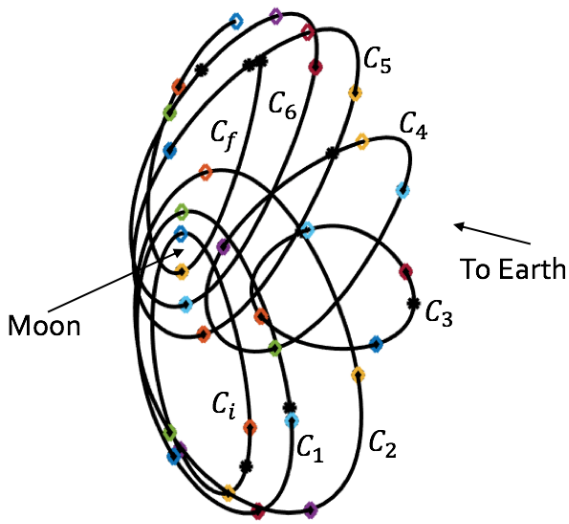

(a) CR3BP-LT Initial Guess

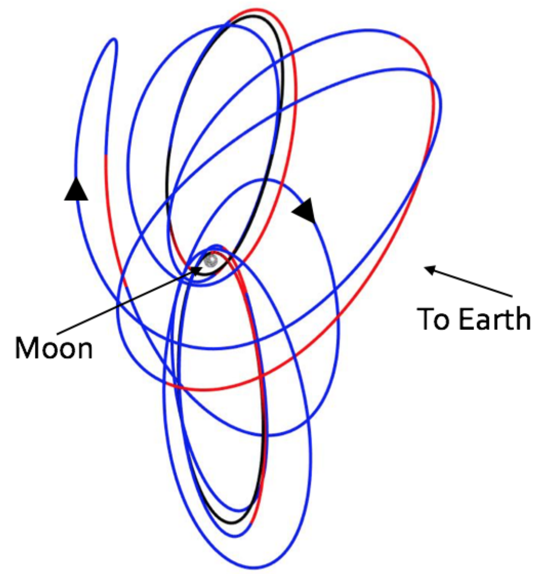

(b) CR3BP-LT Converged Transfer.

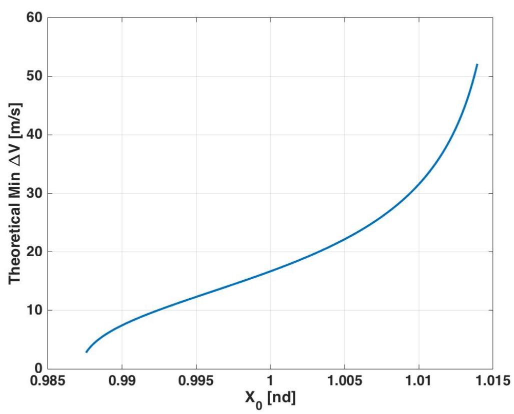

(c) Theoretical Minimum ΔV.

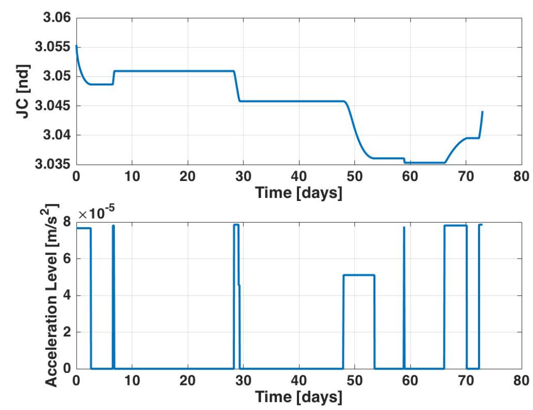

(d) CR3BP-LT Energy and Acceleration Evolution.

Figure 5.17. Performance for a Mass Optimal Interior LT Transfer from a L_2 S NRHO to a L_2 N NRHO in the CR3BP-LT Model

different transfer from the L_2 S 9:2 NRHO to other multi-body orbits in the lunar vicinity are explored as possible candidates for LIC extended mission options. The initial guess for all transfers is generated within the context of CR3PB system, and later corrected in a higher-fidelity ephemeris model that includes the gravitational perturbations of the Sun, the Earth and the Moon. All transfers are locally optimal solutions generated via a Sequential Quadratic Programming (SQP) direct optimization scheme.

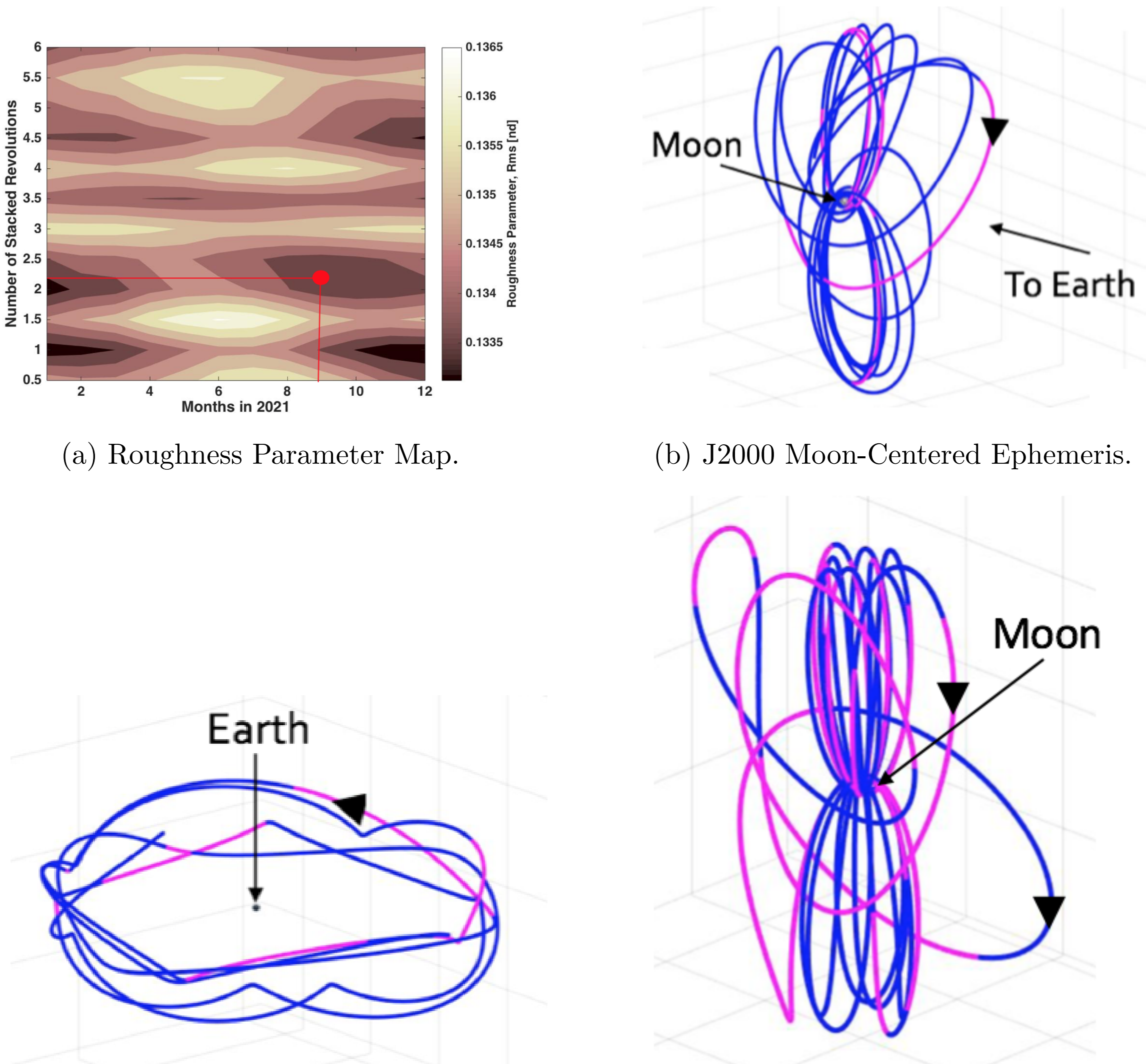

(a) Roughness Parameter Map.

(b) J2000 Moon-Centered Ephemeris.

(c) Earth-Centered Ecliptic Ephemeris.

(d) Moon-Centered Ecliptic Ephemeris.

Figure 5.18. Performance for a Mass Optimal LT Interior Transfer from a L_2 S NRHO to a L_2 N NRHO in the SEM Ephemeris Model

5.2.1 Transfer from a NRHO to a Lunar Distant Retrograde Orbit (DRO)

Consider the design of a low-thrust spacecraft trajectory from a L_2 S 9:2 NRHO to a 70,000km-altitude Distant Retrograde Orbit (DRO) around the Moon. The design of this trajectory is particularly challenging, as both the departure and the arrival orbits are considered to be stable orbits in the Lyapunov sense. This stability characteristic suggests that there are no structures that depart or arrive into the orbits naturally, such as invariant manifold structures; hence, a creative strategy for generating informed initial guesses is required.

The orbit chaining framework within the context of the energy-informed adaptive algorithm provides such strategy. It creates an informed initial guess for an interior transfer in the CR3BP model by selecting orbits from the L_2 S halo and the P_2 DRO families of orbits as illustrated in Figure 5.19(a) , and delivers the mass-optimal solution in Figure 5.19(b), that utilizes the minimum possible number of intermediate arcs. Figure 5.19(d) represents the evolution of the Jacobi constant as well as the thrust acceleration level of the spacecraft throughout the trajectory.

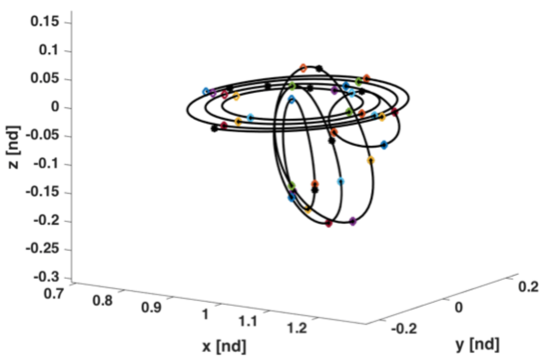

(a) CR3BP-LT Initial Guess

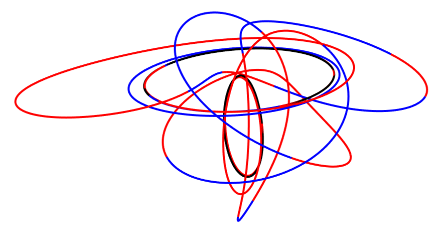

(b) CR3BP-LT Converged Transfer.

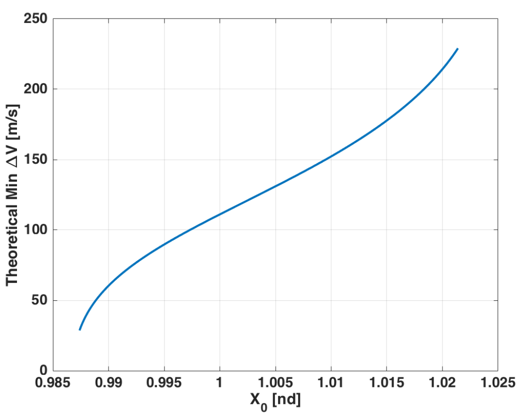

(c) Theoretical Minimum ΔV.

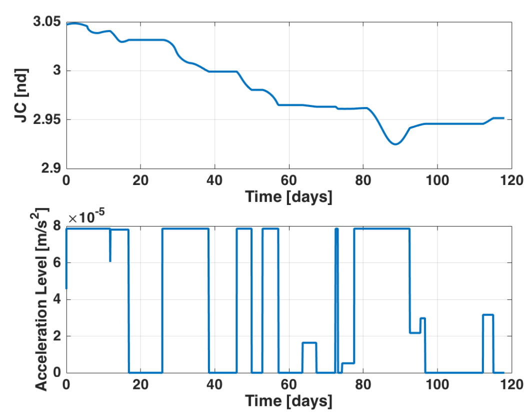

(d) CR3BP-LT Energy and Acceleration Evolution.

Figure 5.19. Performance for a Mass Optimal Interior LT Transfer from a L_2 S NRHO to a P_2 DRO in the CR3BP-LT Model

The CR3BP solution is fed as the initial guess for converging the interior trajectory in the higher-fidelity ephemeris model. The mass-optimal interior solution in the ephemeris model is depicted in Figures 5.20(b)-(d) for representations in three different frames, with varying central bodies. Red arcs in the figures correspond to thrusting segments, while the arcs represent the times at which LIC is coasting. Figure 5.20(a) correspond to the RPM utilized to select the departure epoch. For the case of the interior transferin the ephemeris model, the spacecraft requires 118.7911 days to travel from the departure to the arrival orbit, while consuming 0.2647 kg of the 13.6 kg of the assuming remaining spacecraft mass from phases I and II. A second strategy in the trajectory design framework of LIC's phase III explores the generation of exterior-type transfers, by utilizing nearby structures that depart the vicinity of the Earth-Moon system. Such is the case of some of the exterior resonant orbits that exist within the context of the CR3BP force model.

A 3:4 resonant arc is then utilized to generate an informed initial guess for constructing an exterior trajectory from the L_2 S 9:2 NRHO science orbit to the 70,000km-altitude DRO. Even though many resonant families do exist within the CR3BP force model, the 3:4 family is chosen due to its wide range of energy span, as well as its three-dimensional reach in configuration space, which is advantageous when constructing initial guesses for transfers between highly inclined (i.e., out-of-plane) orbits.

The initial guess is converged and optimized in the lower-fidelity CR3BP force model, and that solution is later utilized to generate the exterior ephemeris mas-optimal trajectories in Figures 5.21(a)-(c), where its representation as seen by different observers is depicted. As expected, LIC departs the vicinity of the Moon to accomplish the required plane and energy changes, to later re-enter the system and arrive on its destination orbit. Majority of the thrusting happens away from the lunar region. For the case of the exterior-type transfers, LIC requires 110.1077 days to travel from the science orbit to the DRO, and, it consumes about 0.1481 kg of the remaining 13.6 kg mass.

5.2.2 Transfer from a NRHO to a 'Flat' Halo Orbit

As a second extended option for the LIC spacecraft, this investigation studies the design of a low-thrust spacecraft trajectory from a L_2 S 9:2 NRHO to a Northern (N) 'flat' halo

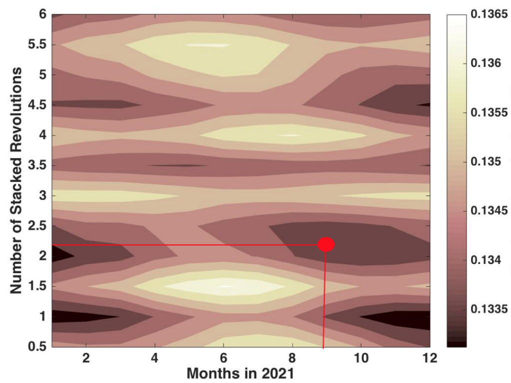

(a) Roughness Parameter Map.

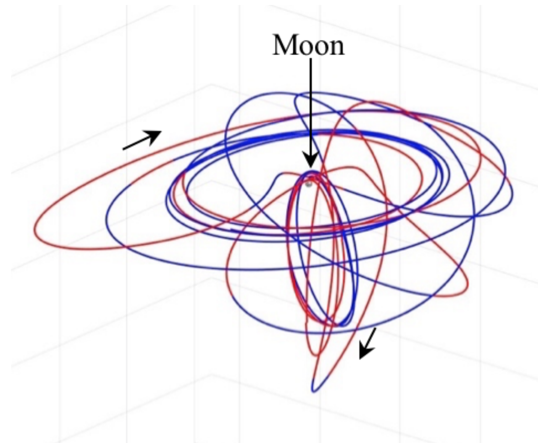

(b) J2000 Moon-Centered Ephemeris.

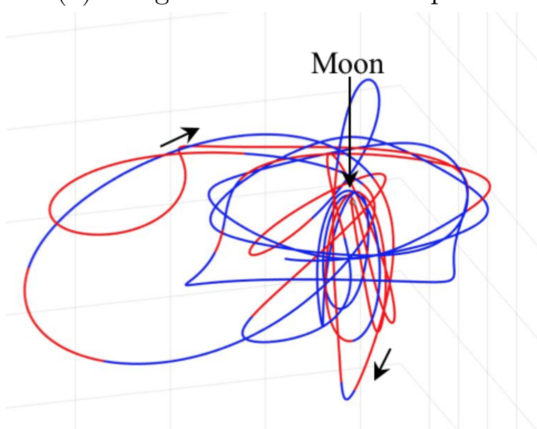

(c) Earth-Centered Ecliptic Ephemeris.

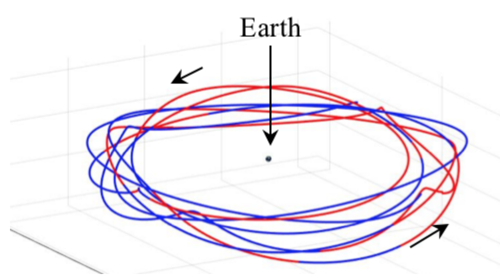

(d) Moon-Centered Ecliptic Ephemeris.

Figure 5.20. Performance for a Mass Optimal Interior LT Transfer from a L_2 S NRHO to a P_2 DRO in the SEM Ephemeris Model

orbit in the vicinity of the $_2$ libration point. Even though the arrival halo orbit is unstable in the Lyapunov sense, which suggest the existence of manifold structures leaving to and from the periodic orbit, the energy-informed adaptive algorithm is once again leveraged to construct an interior-type initial guess in Figure 5.22(a), that is corrected in the lower-fidelity CR3BP model as illustrated in 5.22(b), utilizing the minimum number of intermediate orbits required to travel from departure to destination.

The CR3BP mass-optimal solution is re-converged in the ephemeris model for a November 1st, 2022 selected epoch. This epoch is chosen from the roughness parameter technique shown in Figure 5.23(a), to enable LIC to complete its primary mission around the L_2 S 9:2 NRHO science orbit. Figures 5.23(b)-(d) represent the mass-optimal solution corrected in

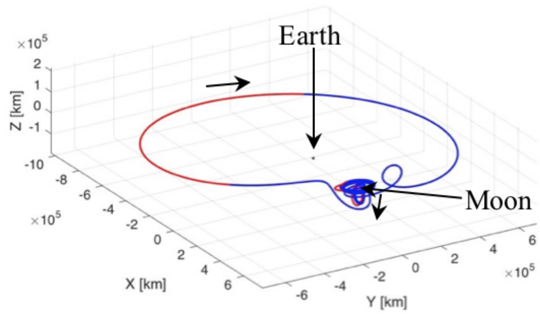

(a) J2000 Moon-Centered Ephemeris.

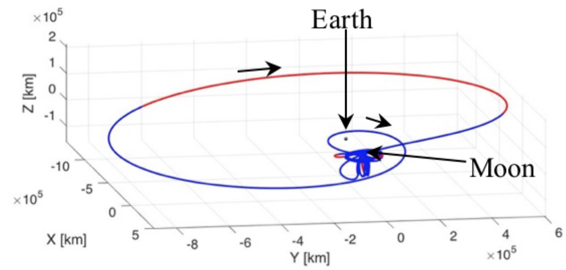

(b) Earth-Centered Ecliptic Ephemeris.

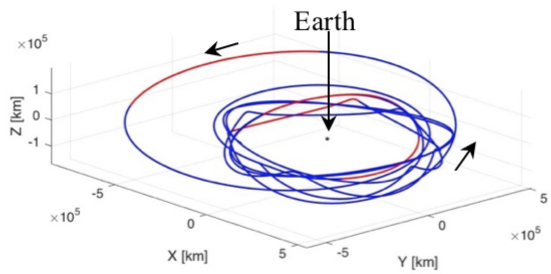

(c) Moon-Centered Ecliptic Ephemeris.

Figure 5.21. Performance for a Mass Optimal Exterior LT Transfer from a L_2 S NRHO to a P_2 DRO in the SEM Ephemeris Model

a higher-fidelity ephemeris model, for an observer fixed in three different reference frames. The trajectory design framework selects the use of the sliding algorithm over the use of manifold structures, to guarantee that the spacecraft does not exhibit long transits around the Earth-Moon system.

For all three observers, it is seen that the spacecraft does not depart the vicinity of the Moon, behavior that is consistent with that of interior-type transfer trajectories. For each of the plots in Figure 5.23, the red portions of the transfer represent segments where the thrust is active, while the blue arcs correspond to segments where the spacecraft's engine is turned off. LIC performance for this potential extended mission interior transfer requires 164.1934 days of transit from the departure to the arrival orbits, and it consumes 0.3046 kg of propellant.

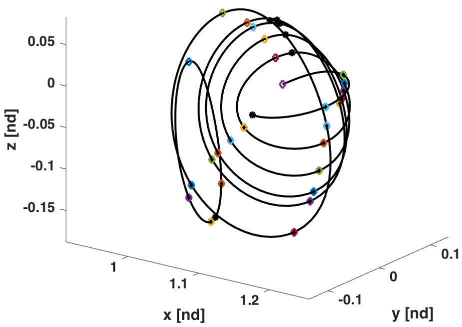

(a) CR3BP-LT Initial Guess

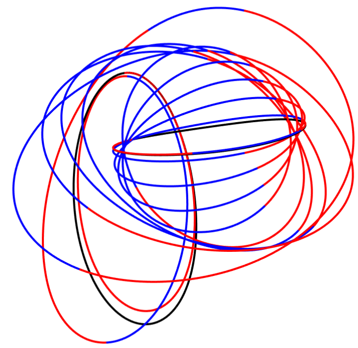

(b) CR3BP-LT Converged Transfer.

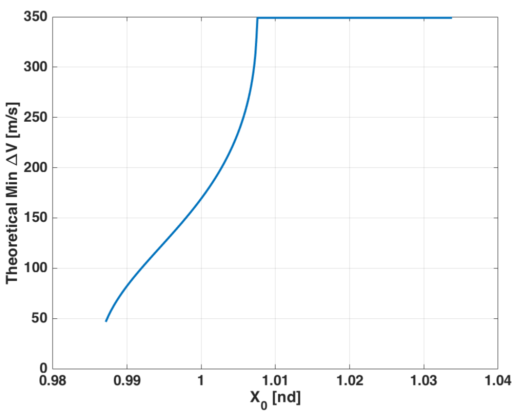

(c) Theoretical Minimum ΔV.

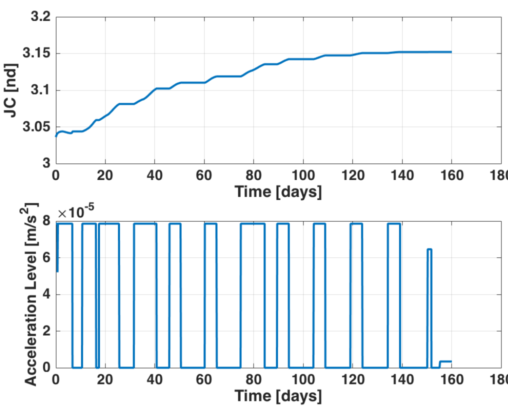

(d) CR3BP-LT Energy and Acceleration Evolution.

Figure 5.22. Performance for a Mass Optimal Interior LT Transfer from a L_2 S NRHO to a L_2 'Flat' Halo in the CR3BP-LT Model

An exterior-type transfer is also generated for the case of LIC traveling from the L_2 S 9:2 NRHO science orbit to a L_2 'flat' halo orbit as shown in Figures 5.24(a)-(c).
In this scenario, it is noted that the arrival orbit is unstable in the Lyapunov sense, hence, it does possess natural structures that depart and arrive into the orbit in a ballistic fashion. These structures are computed via invariant manifold theory, and along with a Poincaré mapping technique, are utilized to construct initial guesses for the exterior transfers in the CR3BP force model. Once the initial guess is converged as a mass-optimal continuous solution in the lower-fidelity model, this result is fed into the higher-fidelity ephemeris dynamics as initial guess, producing the exterior-type transfers in Figure 5.24, where the motion is visualized as seen from an observer placed in three different reference frames. In this case,

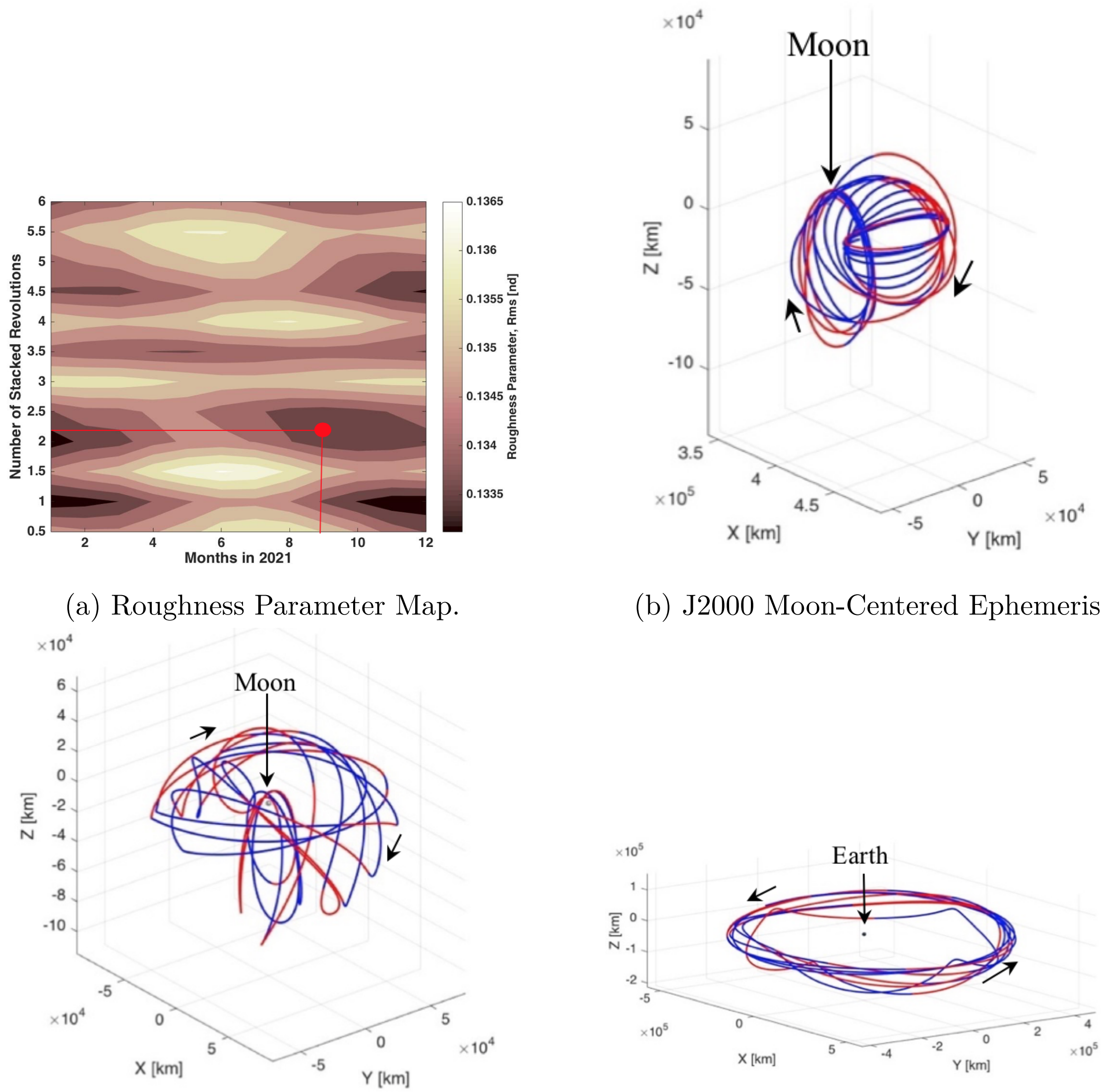

(a) Roughness Parameter Map.

(b) J2000 Moon-Centered Ephemeris.

(c) Earth-Centered Ecliptic Ephemeris.

(d) Moon-Centered Ecliptic Ephemeris.

Figure 5.23. Performance for a Mass Optimal Interior LT Transfer from a L_2 S NRHO to a L_2 'Flat' Halo in the SEM Ephemeris Model

LIC requires 106.4887 days to travel from the departure primary mission science orbit to the arrival orbit near the L_2 libration point. The propellant consumption is such that 0.1745 kg of the phase II 13.6 kg remaining are consumed.

5.2.3 Transfer from a NRHO to a Low Lunar Elliptical Orbit (LLO)

The last potential extended mission scenario studied in this investigation, considers transferring LIC from the L_2 S 9:2 NRHO science orbit to a low lunar elliptical orbit with a 100km

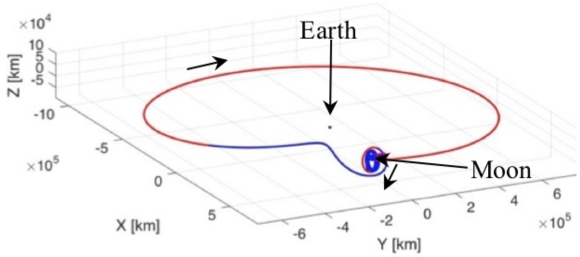

(a) J2000 Moon-Centered Ephemeris.

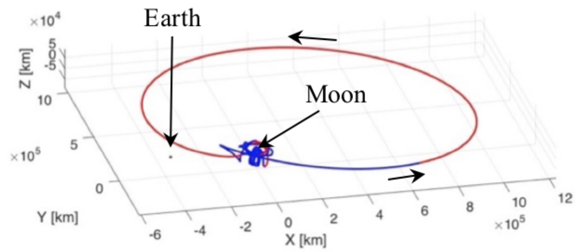

(b) Earth-Centered Ecliptic Ephemeris.

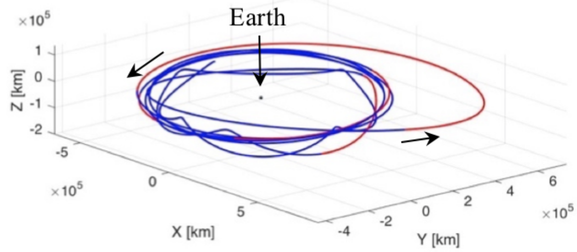

(c) Moon-Centered Ecliptic Ephemeris.

Figure 5.24. Performance for a Mass Optimal Exterior LT Transfer from a L_2 S NRHO to a 'Flat' Halo in the SEM Ephemeris Model

periapsis altitude and a 5,000 km apoapsis altitude. The full set of Keplerian orbital elements that defined the arrival orbit are summarized in Table 5.2. An interior-type transfer is sought from the generalized trajectory design framework.

Table 5.2. Summary of Keplerian orbital elements defined in a Moon-centered inertial frame for the selected arrival low lunar elliptical orbit

Orbital Elements	**Value**
Semi-Major Axis, a	4,287.4 km
Eccentricity, e	0.5714
Inclination, i	56 deg
RAAN, Ω	65 deg
Argument of Periapsis, ω	355 deg

The orbital inclination is measured relative to the Moon's equator and the right ascension of the ascending node (RAAN) is defined with respect to the vernal equinox vector. The main challenge encountered on the design of this trajectory is derived from the large energy gap between the departure and arrival orbits. Furthermore, the energy-informed adaptive sliding algorithm needs to accommodate that the two orbits exist in different dynamical models, as the departure orbit resides within the context of the CR3BP force model, while the arrival orbit is a Keplerian conic defined in the context of the Two-Body Problem (2BP). The first step in the trajectory design framework is then to transform the Keplerian orbit to its correspondent trajectory in the CR3BP force model, as illustrated in Figure 5.25, where it is seen that the LLO is no longer a conic section nor it is a periodic orbit. The path is propagated for 160 revolutions of the original Keplerian orbit, whose orbital period is of about seven hours.

Once the arrival orbit is transformed into CR3BP coordinates, the trajectory design is split into two steps:

1. Backwards propagation with a suboptimal thrust spiral from the LLO until the trajectory crosses a selected surface of section in the lunar region

2. Slide through a number of intermediate members of the L_2 S halo family, until the energy of the intermediate orbit matches the energy of the thrust spiral trajectory on the surface of section

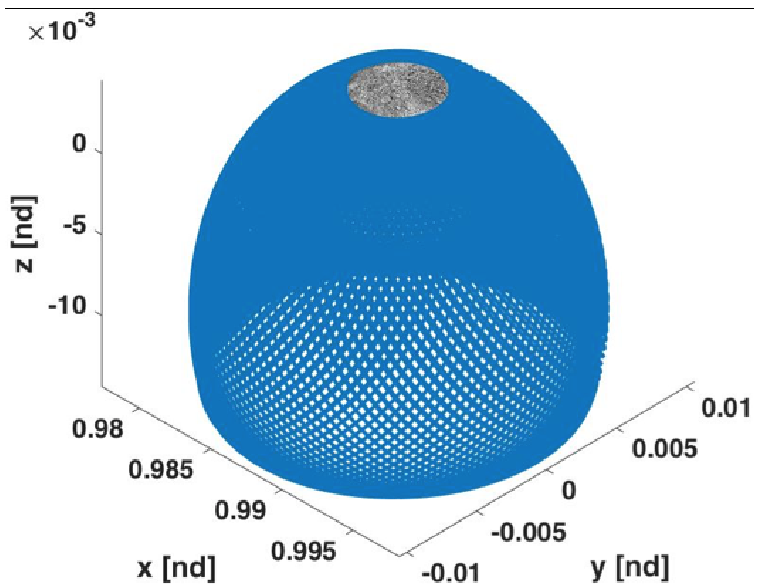

Figure 5.25. Low lunar elliptical orbit transformed into the CR3BP dynamical model

The initial guess constructed from this design methodology in the CR3PB is depicted in Figure 5.26. The energy-informed adaptive sliding algorithm suggests that three members of the southern halo family of orbits near the L_2 libration point, be incorporated from the orbit chaining framework.

To fully generate a converge solution, it is necessary to link steps 1. and 2. from the trajectory design process, by means of a differential corrections scheme, that delivers an interior-type path continuous in position, velocity and mass states. Such solution is represented in Figure 5.27 for the CR3BP force model, where the red and blue arcs correspond to thrust and coast segments, respectively. The spacecraft requires 72.9701 days to travel from the departure to the destination orbit, and it consumes about 0.4671 kg of the remaining propellant mass from LIC's phases I and II primary mission. The solution in Figure 5.27 is a mass-optimal trajectory. By utilizing the roughness parameter technique, a departure epoch of September 1st, 2022 is selected to transition the CR3BP solution into a higher-fidelity trajectory, depicted in Figures 5.28(a)-(c), for an observer fixed in three different reference frames.

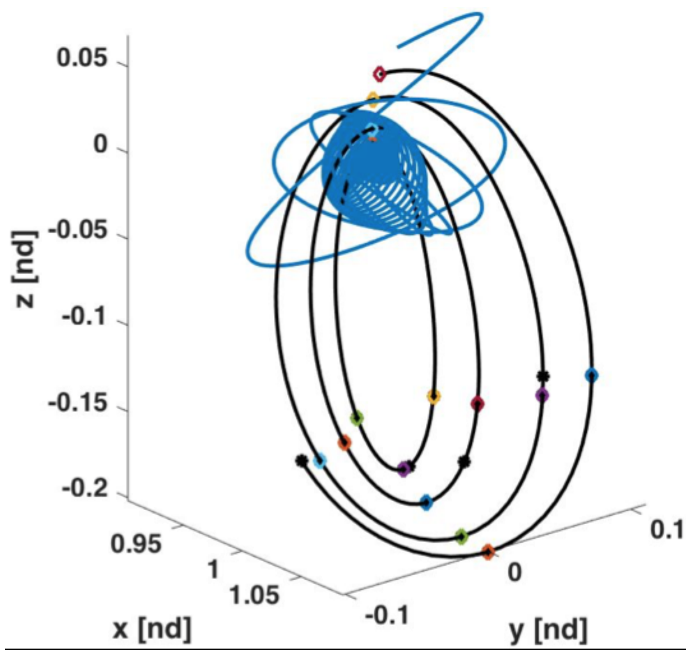

Figure 5.26. Initial guess for the interior trajectory from a L_2 S NRHO to an Elliptical LLO in the CR3BP-LT

In all three ephemeris plots for the different central bodies and reference frames in Figure 5.28, the J2000 inertial frame centered at the Earth, the ecliptic frame center at the Moon, and the barycentric rotating frame, it is observed that the energy-informed adaptive sliding algorithm is successful in producing a mass-optimal solution in the higher-fidelity ephemeris model that does not need to depart the Earth-Moon system to accomplish the required change in energy. The LIC spacecraft requires 66.0889 days to travel from the $_2$ S 9:2 NRHO science orbit to the low lunar elliptical arrival orbit, and it consumes 0.5356 kg of propellant from the 13.6kg remaining from phases I and II.

As expected, the transfer geometry when observed from the barycentric rotating frame in the ephemeris model resembles that of the mass-optimal solution converged in the CR3BP-LT.

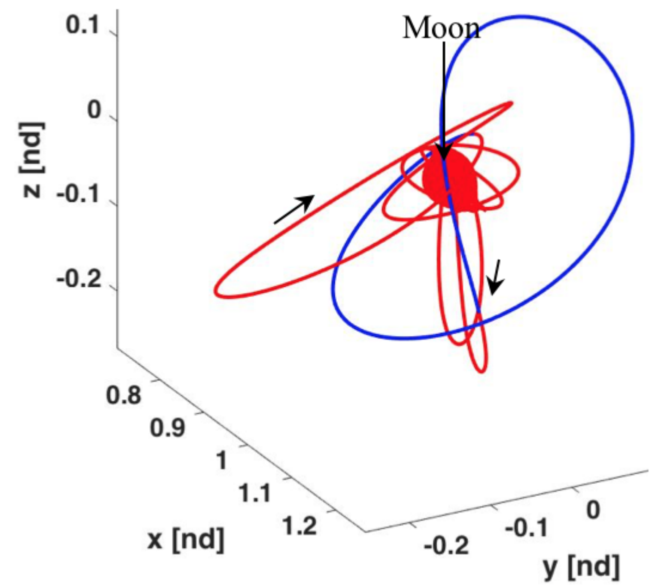

Figure 5.27. Converged solution for the interior trajectory from a L_2 S NRHO to an Elliptical LLO in the CR3BP-LT

5.2.4 Summary of Potential Extended Mission Options

Table 5.3 depicts a summary of the results obtained in this investigation, for a variety of sample candidate transfer options for the Lunar IceCube spacecraft, after the completion of its primary science and technology demonstration mission objectives. All interior and exterior transfers are generated utilizing an energy-informed adaptive sliding algorithm and optimized for propellant consumption in a higher-fidelity ephemeris model that includes the point mass gravitational acceleration of the Sun, the Earth and the Moon. Furthermore, all interior and exterior trajectories are evaluated for a range of different epochs starting in March 1st, 2022, epoch after which LIC would have already arrived in its primary science mission orbit. By leveraging the roughness parameter technique, via measurement of the RMS value of the position profile of each initial guess trajectory for every epoch in consideration, a departure epoch from the L_2 S 9:2 NRHO science orbit was selected for each transfer scenario. All transfers constructed with this trajectory design framework meet the propellant and time-of-flight requirement for possible extended mission options for the Lunar IceCube spacecraft.

Table 5.3. Summary of results for Phases III of LIC potential extended mission options trajectories from the primary science mission orbit

Orbit	**Type**	$\Delta m[kg]$	**ToF [days]**
DRO	Interior	0.2647	118.7911
	Exterior	0.1481	110.1077
'Flat' halo	Interior	0.3046	164.1934
	Exterior	0.1745	106.4887
LLO	Interior	0.5356	66.0889

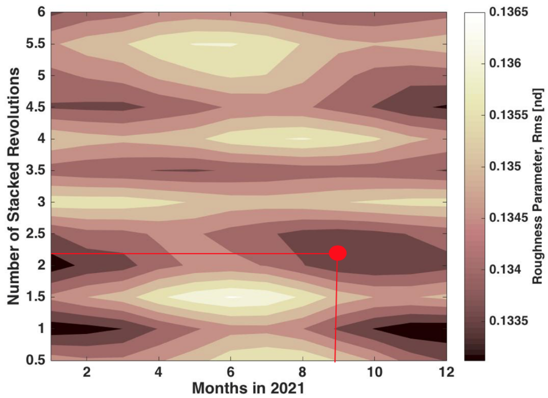

(a) Roughness Parameter Map.

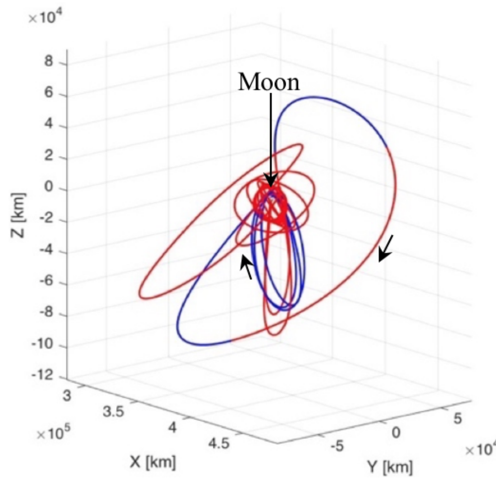

(b) J2000 Moon-Centered Ephemeris.

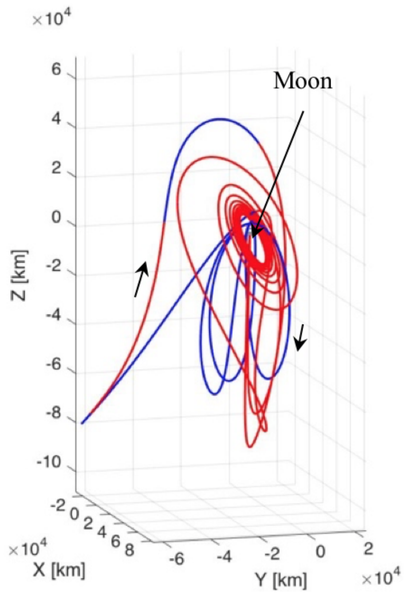

(c) Earth-Centered Ecliptic Ephemeris.

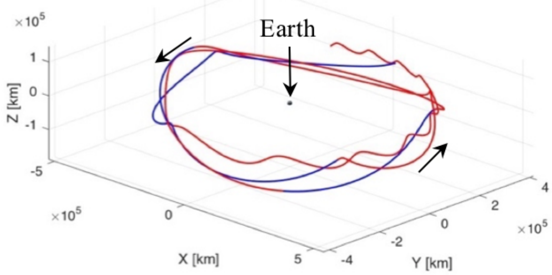

(d) Moon-Centered Ecliptic Ephemeris.

Figure 5.28. Performance for a Mass Optimal Interior LT Transfer from a L_2 S NRHO to an Elliptical LLO in the SEM Ephemeris Model

6. CONCLUDING REMARKS

Low-thrust spacecraft trajectory design in the cislunar region is highly driven by the dynamical regime utilized to describe the equations of motion. To accurately represent this dynamical environment, different levels of fidelity —the circular restricted three-body problem system and the higher-fidelity ephemeris model—, are considered in this investigation, and presented for applications of vehicles travelling between libration point orbits in the Earth-Moon system. Strategies for rapid and accurate generation of initial guesses for low-thrust spacecraft trajectory design is evolving in such a way, that the filed of numerical methods continue to be both a driving factor and a constraint when finding converged solutions that satisfy all of the mission requirements. A number of numerical approaches are presented in this investigation, including multiple shooting and direct optimization schemes, that are used to perform an extensive analysis of the motion of vehicles powered by low-thrust engines, travelling in the vicinity of the Moon within the context of the circular restricted three-body problem.

6.1 Investigation Summary

A new method for constructing initial guesses, for transfers between libration point orbits in the Earth-Moon CR3BP-LT system, has been explored, via exploitation of the energy parametrization of the periodic orbit families. This method yields to a type of transfer geometry, which in this investigation is denoted the sliding-type geometry; the spacecraft slides through a set of intermediate members of specific periodic orbit families, to transfer from a departure orbit to a target destination.

The time-of-flight versus the propellant consumption trade-off, experienced in the sliding-type trajectories, is compared side by side with the most popular escape-type geometries; the spacecraft leaves the system to gain sufficient energy to perform plane changes, and reduce propellant cost. It has been discovered in this investigation, that with the sliding-type geometry, similar trajectory performances are achieved. The sliding method is valid in any CR3BP-LT model, employs members of different families as intermediate orbits —orbit chaining method—.

6.1.1 Adaptive Orbit Chaining Approach

The adaptive sliding algorithm successfully produces transfers over a range of low-thrust problems of varying complexity. While manifold arcs aid in constructing interior and exterior transfer geometries, the energy-informed adaptive sliding algorithm offers the capability for identifying interior transfer geometries when manifolds arcs are not available, e.g., when moving between stable periodic orbits. Furthermore, the sliding methodology is valid for any CR3BP-LT model, and employs members of different families as intermediate orbits, consistent with an orbit chaining method. Since the geometry of the converged solution relies heavily on the initial guess, there are an infinite number of options for sliding through a bounded region of space and transferring between departure and arrival orbits.

Trajectories resulting from this algorithm are successfully transitioned into a higher-fidelity ephemeris model with solar and lunar gravitational perturbations. Sliding geometry transfers are transitioned into the higher-fidelity ephemeris model from either a converged solution in the CR3BP-LT model, or, from a set of periodic orbits generated as the initial guess by the sliding algorithm. The roughness parameter maps aid in generalizing this transition, by offering a range of possible epochs that reduce the sensitivity of the problem, and guarantees a smooth performance of the multiple shooting corrections process. The weighting parameters in the objective function in the adaptive sliding algorithm are easily modified to accommodate either mass-optimal or time-optimal solutions. Regardless of the prioritization for this minimization function, the algorithm delivers a locally optimal solution with the minimum number of intermediate orbits from departure to destination.

Understanding the effects of the changes in the thrust magnitude, on the final transfer geometry of the solution, is the main query of the third fundamental question proposed in this investigation. One possibility to closely examine this impact, is by applying a continuation strategy on the thrust magnitude of locally optimal solutions that exhibit no coast arcs, i.e., solutions that are optimized for a minimum time-of-flight:

$$\min J = ToF.$$

It is known that transfers converged with lower acceleration levels, will automatically modify the transfer geometry –will deviate from the precomputed reference path–; thus, understanding the impact of the acceleration level when transitioning to the ephemeris model, aids in evaluating the validity of the methods and solutions developed in this investigation.

6.1.2 Lunar IceCube Mission

In this investigation presents a trajectory design framework for generating lunar IceCube (LIC) traansfers from its primary science mission orbit to other extended potential candidate periodic orbits in the lunar vicinity is explored, in an aim to exploit the efficiency of the low-thrust engine. Candidate periodic orbits that exist within the context of the CR3BP dynamical model are selected and optimized via both indirect and direct optimization techniques, to produce locally optimal solutions that satisfy the physical constraints introduced by the lunar IceCube spacecraft.

The adaptive sliding algorithm strategy developed in this work is utilized to construct initial guesses for CubeSat-type spacecraft transfers, under the assumptions of the Two-Body Problem (2BP) and the Circular Restricted Three-Body Problem (CR3BP) lower fidelity force models, that are later transitioned into a higher fidelity ephemeris model. Low-thrust trajectories for spacecraft traveling in cislunar space are generated via a modified version of the traditional orbit chaining framework. This strategy is employed regardless of the force model in which the departure and arrival orbits exits, and, a step-by-step approach is provided for the construction of informed initial guesses for the trajectory design problem.

6.2 Recommendations for Future Work

The type of low-thrust engine examined in this investigation is consistent with the electric propulsion technology, whose efficiency and capabilities are continuously evolving. Therefore, the flexibility of the trajectory design framework must also evolve to be consistent with the new technological advances. This feature signifies for the low-thrust trajectory design framework to be flexible enough such that it does not depend on the type of vehicle utilized, nor on the dynamical model employed to construct the initial estimate. Some of the directions for future work recommendations concerning the initial guess generation of low-thrust spacecraft trajectories between libration point orbits are outlined below:

6.2.1 A Modified Adaptive Orbit Chaining Framework

A modified orbit chaining strategy consist of dividing the problem of transferring a low-thrust spacecraft from a departure to an arrival orbit into multiple subproblems. The process is outlined as follows: from the target arrival orbit, a family of destination orbits is constructed via a continuation method, such that, the first member of said family is the target arrival orbit, and, the last member of the family of destination orbits is the last orbit computed via the continuation method. The goal of the first subproblem in the modified orbit chaining strategy is then to deliver the spacecraft from the departure orbit to the last member of the family of arrival orbits, and each subsequent subproblem utilizes the previously generated converged solution, to deliver the spacecraft from the departure orbit to the next member of the family of destinations orbits. The problem is divided into as many subproblems as the number of destination orbits generated in the family of arrival orbits.

A natural parameter continuation method can then be successfully introduced into the implementation of a generalized modified orbit chaining technique, that leverages an energy-informed adaptive sliding algorithm to navigate the cislunar space in the construction of informed initial guesses, and delivers optimal trajectories for low-thrust spacecraft moving in the vicinity of the Moon, that are easily transition from lower fidelity force models into a higher fidelity model that includes the gravitational attraction of the Sun, the Earth and the Moon.

6.2.2 Applications to Orbit Maintenance Methods

When trying to maintain a low-thrust spacecraft in a particular orbit in the vicinity of the Moon, it is necessary to understand the effects of changes in the control variables, on the stability of the trajectory. This implies the ability for a particular corrections or targeting algorithm to provide precise information for the thrust acceleration level and orientation of the thrust vector, required to follow a particular reference path. Since only low-thrust maneuvers are being analyzed in this investigation, the capability to control the duration for which the vehicle remains within a specified region in space, under the effects of the thrust acceleration vector, is of great interest in this analysis. The development of linear and nonlinear control strategies to further refine the a priori construction of the control history to achieve the desired ordered motion of the spacecraft, will aid in maintaining the spacecraft in a specified orbit for a longer duration of time.

It is then necessary to explore the effects of the perturbations acting on the baseline trajectories generated by the adaptive sliding algorithm —errors in position/velocity,burn errors—, and perform an analysis on the response of the control effort required to satisfy the mission constraints under the new dynamical regime. Furthermore, a critical value of the thrust acceleration magnitude can be determined by performing a global sensitivity analysis, for which the transfer geometry no longer resembles that of the reference path.

REFERENCES

[1] F. Diacu, “The solution of the n-body problem,” *The Mathematical Intelligencer*, vol. 18, pp. 66–70, 3 1996.

[2] E. Lorenz, “Deterministic nonperiodic flow,” *Journal of the Atmospheric Sciences*, vol. 20, pp. 130–141, 2 1963.

[3] M. Hénon and C. Heiles, “The applicability of the third integral of motion: Some numerical experiments,” *The Astronomical Journal*, vol. 69, pp. 73–79, 1 1964.

[4] H. Keller, “Numerical solution of two point boundary value problems,” *Society for Industrial and Applied Mathematics*, 1976.

[5] J. Stoer and R. Burlirsch, “Introduction to numerical analysis,” *Society for Industrial and Applied Mathematics*, 1983.

[6] G. Gómez, J. Masdemont, and C. Simó, “Quasihalo orbits associated with libration points,” *Journal of the Astronautical Sciences*, vol. 46, pp. 135–176, 1998.

[7] J. Mondelo, “Contribution to the study of fourier methods for quasi-periodic functions and the vicinity of the collinear libration points,” Ph.D. Thesis, Departament de Matematica Aplicada i Analisa, Universitat de Barcelona, 2001.

[8] K. Howell and H. Pernicka, “Numerical determination of lissajous trajectories in the restricted three-body problem,” *Celestial Mechanics*, vol. 41, pp. 107–124, 1987.

[9] T. Pavlak, “Mission design applications in the earth-moon system: Trans- fer trajectories and stationkeeping.,” M.S. Thesis, School of Aeronautics and Astronautics, Purdue University. West Lafayette, Indiana, May, 2010.

[10] E. Y. Choueiri, “A critical history of electric propulsion: The first 50 years (1906-1956),” *Journal of Propulsion and Power*, vol. 20, pp. 193–203, 2008.

[11] J. Sovey, V. Rawlin, and M. Patterson, “A synopsis of ion propulsion develop- ment projects in the united states - sert i to deep space 1,” *5th Joint Propulsion Conference and Exhibit. Los Angeles, CA*, 1999.

[12] M. D. Rayman, “The successful conclusion of the deep space 1 mission: Important results without a flashy title,” *53rd International Astronautical Congress. Houston, TX*, pp. 1–13, 2002.

[13] C. Russell and C. Raymond, *The Dawn Mission to Minor Planets 4 Vesta and 1 Ceres*. New York: Springer-Verlag, 2012.

[14] J. Kawaguchi, A. Fujiwara, and T. Uesugi, “Hayabusa-1 its technology and science accomplishment summary and hayabusa-2,” *Acta Astronautica*, vol. 62, pp. 639–647, 2008.

[15] K. C. Howell, B. T. Barden, and M. W. Lo, “Application of dynamical systems theory to trajectory design for a libration point mission,” *The Journal of the Astronautical Sciences*, vol. 45, pp. 161–178, 1997.

[16] M. Lo, B. Williams, W. Bollman, D. Hahn, J. Bell, E. Hirst, R. Corwin, P. Hong, K. Howell, B. Barden, and R. Wilsons, “Genesis mission design,” *19th AIAA/AAS Astrodynamics Specialist Conference*, 1998.

[17] W. S. Koon, M. W. Lo, J. E. Marsden, and S. D. Ross, “Heteroclinic connections between periodic orbits and resonance transitions in celestial mechanics,” *Chaos: An Interdisciplinary Journal of Nonlinear Science*, vol. 10, pp. 427–469, 2000.

[18] G. Gómez, W. S. Koon, M. W. Lo, J. E. Marsden, J. J. Masdemont, and S. D. Ross, “Connecting orbits and invariant manifolds in the spatial restricted three-body problem,” *Nonlinearity*, vol. 17, pp. 1571–1606, 2004.

[19] S. Ross and M. Lo, “The lunar l1 gateway-portal to the stars and beyond,” *AIAA Space 2001 Conference and Exposition. Albuquerque, New Mexico*, pp. 47–68, 2001.

[20] M. W. Lo and J. S. Parker, “Chaining simple periodic three body orbits,” *AAS/AIAA Astrodynamics Specialist Conference. Lake Tahoe, California*, 2005.

[21] J. S. Parker, K. E. Davis, and G. H. Born, “Chaining periodic three-body orbits in the earth-moon system,” *Acta Astronautica*, vol. 67, pp. 623–638, 2010.

[22] M. Vaquero and K. C. Howell, “Leveraging resonant-orbit manifolds to design transfers between libration-point orbits,” *Journal of Guidance, Control, and Dynamics*, vol. 37, pp. 1143–1157, 2014.

[23] A. F. Haapala and K. C. Howell, “A framework for constructing transfers linking periodic libration point orbits in the spatial circular restricted three-body problem,” *International Journal of Bifurcation and Chaos*, vol. 26, 2016.

[24] R. L. Restrepo and R. P. Russell, “A database of planar axi-symmetric periodic orbits for the solar system,” *AAS/AIAA Astrodynamics Specialist Conference. Stevenson, Washington*, 2017.

[25] A. Das-Stuart, “Artificial intelligence aided rapid trajectory design in complex dynamical environments,” Ph.D. Thesis, School of Aeronautics and Astronautics, Purdue University. West Lafayette, Indiana, May, 2019.

[26] R. E. Pritchett, K. C. Howell, and D. J. Grebow, "Low-thrust transfer design based on collocation techniques: Applications in the restricted three-body problem," *AAS/AIAA Astrodynamics Specialist Conference. Stevenson, Washington*, 2017.

[27] I. Newton, *The Principia: Mathematical Principles of Natural Philosophy*. Berkely California: University of California Press, 1999.

[28] H. Poincaré, "Les méthods de la méchanique céleste," *History of Modern Physics and Astronomy, American Institute of Physics*, vol. 13, 1993.

[29] F. Moulton, *Periodic Orbits*. Carnegie Institution of Washington. Washington, D.C., 1920.

[30] M. Henon, "Exploration numérique du probleme restreint. ii. masses égales," *Annales d'Astrophysique*, vol. 28, pp. 992–1007, 1965.

[31] E. Goodrich, "Numerical determination of short-period trojan orbits in the restricted three-body problem," *The Astronomical Journal*, vol. 71, pp. 88–93, 1996.

[32] V. Szebehely, *Theory of Orbits: The Restricted Problem of Three Bodies.* Academic Press Inc., New York, 1967.

[33] R. Broucke, *Periodic Orbits in the Restricted Three-Body Problem with Earth-Moon Masses*. Technical Report 32-1168, Jet Propulsion Laboratory. Pasadena California, 1968.

[34] J. Breakwell and J. Brown, "The 'halo' family in 3-dimensional periodic orbits in the earth-moon restricted 3-body problem," *Celestial Mechanics*, vol. 20, pp. 389–404, 1979.

[35] C. Zagouras and P. Kazantzis, "Three-dimensional periodic oscillations generating from plane periodic ones around the collinear lagrangian points," *Astrophysics and Space Science*, vol. 61, pp. 389–409, 1979.

[36] K. Howell, "Three-dimensional, periodic, 'halo' orbits," *Celestial Mechanics*, vol. 32, pp. 53–71, 1984.

[37] K. Howell and E. Campbell, "Three-dimensional periodic solutions that bifurcate from halo families in the circular restricted three-body problem," *AAS/AIAA Paper No. 1999-161, AAS/AIAA Space Flight Mechanics Metting. Breckenridge, Colorado, Febraury 7-10*, 1999.

[38] D. Grebow, "Generating periodic orbits in the circular restricted three-body problem with applications to lunar south pole coverage.," M.S. Thesis, School of Aeronautics and Astronautics, Purdue University. West Lafayette, Indiana, May, 2016.

[39] R. Anderson and M. Lo, “The role of invariant manifold theory in low-thrust trajectory design,” *Journal of Guidance, Control, and Dynamics*, vol. 32, pp. 1921–1930, 2009.

[40] A. Cox, “A dynamical systems perspective for preliminary low-thrust trajectory design in multi-body regimes,” Ph.D. Thesis, School of Aeronautics and Astronautics, Purdue University. West Lafayette, Indiana, May, 2020.

[41] N. Bosanac, A. D. Cox, K. C. Howell, and D. C. Folta, “Trajectory design for a cislunar cubesat leveraging dynamical systems techniques: The lunar icecube mission,” *Acta Astronautica*, vol. 144, pp. 283–296, 2018.

[42] M. L. McGuire, L. M. Burke, S. L. McCarty, K. J. Hack, D. C. D. R. J. Whitley, and C. Ocampo, “Low-thrust cis-lunar transfers using a 40 kw-class solar electric propulsion spacecraft,” *AAS/AIAA Astrodynamics Specialist Conference. Stevenson, Washington, August*, 2017.

[43] A. V. Ilin, L. D. Cassady, T. W. Glover, M. D. Carter, and F. R. C. Díaz, *A Survey of Missions using VASIMR for Flexible Space Exploration*. Prepared by the Ad Astra Rocket Company in fulfillment of Task Number 004 of NASA PO Number NNJ10HB38P. April, 2010.

[44] J. S. Parker and R. L. Anderson, *Low Energy Lunar Trajectory Design*. John Wiley and Sons. New Jersey, USA, 2014.

[45] G. Mingotti and F. Topputo, “Ways to the moon: A survey,” *Spaceflight Mechanics: Proceedings of the AAS/AIAA Spaceflight Mechanics Meeting*, vol. 140, pp. 2531–2547, 2011.

[46] J. Schoenmaekers, “Post-launch optimisation of the smart-1 low-thrust trajectory to the moon. email: Johan.schoenmaekers@esa.int,” 2004.

[47] D. Grebow, M. Ozimek, and K. Howell, “Advanced modeling of optimal low-thrust lunar pole-sitter trajectories,” *60th International Astronautical Congress. Daejon, Republic of Korea, October 12-16*, 2009.

[48] D. Grebow, M. Ozimek, and K. Howell, “Design of optimal low-thrust lunar pole-sitter missions,” *19th AIAA/AAS Space Flight Mechanics Meeting*, 2009.

[49] G. Radice and G. Radice, “Ant colony algorithms for two-impulse interplanetary trajectory optimization,” *Journal of Guidance, Control and Dynamics*, vol. 29, pp. 1440–1444, 2006.

[50] M. Ceriotti and M. Vasile, “Mga trajectory planning with an aco-inspired algorithm,” *Acta Astronautica*, vol. 67, pp. 1202–1217, 2010.

[51] J. Stuart, K. C. Howell, and R. Wilson, "Design of end-to-end trojan asteroid rendezvous tours incorporating potential scientific value," *Journal of Spacecraft and Rockets*, vol. 53, pp. 278–288, 2016.

[52] R. Furfaro and R. Linares, "Waypoint-based generalized zem/zev feedback guidance for planetary landing via a reinforcement learning approach," *3rd IAA Conference on Dynamics and Control of Space Systems*, 2017.

[53] P. Witsberger and J. Longuski, "Interplanetary trajectory design using a recurrent neural network and genetic algorithm," *AAS/AIAA Astrodynamics Specialist Conference*, 2018.

[54] S. D. Smet, D. J. Scheeres, and J. S. Parker, "Systematic exploration of solar gravity driven orbital transfers in the martian system using artificial neural networks," *AAS/AIAA Astrodynamics Specialist Conference*, 2018.

[55] D. Miller and R. Linares, "Low-thrust optimal control via reinforcement learning," *29th AAS/AIAA Space Flight Mechanics Meeting*, 2019.

[56] A. Das-Stuart, K. C. Howell, and D. Folta, "Rapid trajectory design in complex environments enabled via supervised and reinforcement learning strategies," *69th International Astronautical Congress*, 2018.

[57] M. D. Rayman, P. A. Chadbourne, J. S. Culwell, and S. N. Williams, "Mission design for deep space 1: A low-thrust technology validation mission," *Acta Astronautica*, vol. 45, pp. 381–388, 1999.

[58] M. Rayman, T. Fraschetti, C. Raymond, and C. Russel, "Dawn: A mission in development for exploration of main belt asteroids vesta and ceres," *Acta Astronautica*, vol. 58, pp. 605–616, 2006.

[59] Y. Tsuda, M. Yoshikawa, M. Abe, H. Minamino, and S. Nakazawa, "System design of the hyabusa 2 - asteroid sample return mission to 1999 ju3," *Acta Astronautica*, vol. 91, pp. 356–362, 2013.

[60] D. Hull, *Optimal Control Theory for Applications*. Springer Science Business Media, 2013.

[61] J. Longuski, J. Guzman, and J. Prussing, *Optimal Control with Aerospace Applications*. Springer New York, 2014.

[62] K. Hambleton. (2017). "Deep space gateway to open opportunities for distant destinations," [Online]. Available: https://www.nasa.gov/feature/deep-space-gateway-to-open-opportunities-for-distant-destinations.

[63] J. Senent, C. Ocampo, and A. Capella, “Low-thrust variable-specific-impulse transfers and guidance to unstable periodic orbits,” *Journal of Guidance, Control, and Dynamics*, vol. 28, pp. 280–290, 2005.

[64] J. Barrow-Green, “Poincaré and the three body problem,” *History of Mathematics, American Mathematical Society, Providence, Rhode Island*, vol. 11, 1997.

[65] A. Verdun, “Leonhard euler’s early lunar theories 1725-1752,” *Archive for History of Exact Sciences*, vol. 67, pp. 477–551, 5 2013.

[66] C. Saltzer, R. Craig, and C. Fetherof, “Comparison of chemical and electric propulsion systems for interplanetary travel,” *Proceedings of the IRE*, vol. 48, pp. 465–476, 4 1960.

[67] F. R. C. Díaz, “An overview of the vasimr engine: High power space propulsion with rf plasma generation and heating,” *AIP Conference Proceedings*, vol. 595, 2001.

[68] J. Guckenheimer and P. Holmes, *Nonlinear Oscillations, Dynamical Systems, and Bifurcations of Vector Fields*. Springer-Verlag, New York, USA, 1983.

[69] K. Howell, *AAE 632 Notes*. Purdue University, 2013.

[70] T. M. V. Escribano, “Poincaré sections and resonant orbits in the restricted three-body problem,” Ph.D. Thesis, School of Aeronautics and Astronautics, Purdue University. West Lafayette, Indiana, 2010.

[71] A. F. Haapala, “Trajectory design in the spatial circular restricted three-body problem exploiting higher-dimensional poincare maps,” Ph.D. Thesis, School of Aeronautics and Astronautics, Purdue University. West Lafayette, Indiana, 2014.

[72] L. Perko, *Differential Equations and Dynamical Systems*. Springer-Verlag, New York, USA, 1991.

[73] L. Capdevila, “A transfer network linking earth, moon, and the triangular libration point regions in the earth-moon system,” Ph.D. Thesis, School of Aeronautics and Astronautics, Purdue University. West Lafayette, Indiana, 2016.

[74] E. M. Zimovan, K. C. Howell, and D. C. Davis, “Near rectilinear halo orbits and their application in cis-lunar space,” *3rd International Academy of Astronautics Conference on Dynamics and Control of Space Systems, Moscow, Russia*, 2017.

[75] N. Aeronautics and S. A. (NASA). (2019). “Nasa space science data coordinated archive,” [Online]. Available: `https://nssdc.gsfc.nasa.gov/nmc/spacecraft/display.action?id=1978-079A`.

[76] D. Burnett, B. Barraclough, R. Bennet, M. Neugebauer, L. Oldham, C. Sasaki, D. Sevilla, N. Smith, E. Stansbery, D. Sweetnam, and R. Wiens, "The genesis discovery mission: Return of solar matter to earth," *Space Science Reviews*, vol. 105, pp. 3–4, 2003.

[77] T. A. Pavlak, "Trajectory design and orbit maintenance strategies in multi- body dynamical regimes," Ph.D. Thesis, School of Aeronautics and Astronautics, Purdue University. West Lafayette, Indiana, May, 2013.

[78] J. R. Stuart, "A hybrid systems strategy for automated spacecraft tour design and optimization," Ph.D. Thesis, School of Aeronautics and Astronautics, Purdue University. West Lafayette, Indiana, 2014.

[79] J. Betts, "Practical methods for optimal control using nonlinear programming," *Society for Industrial and Applied Mathematics*, 2010.

[80] J. T. Betts and W. P. Huffman, "Mesh refinement in direct transcription methods for optimal control," *Optim. Control Appl. Meth*, vol. 19, pp. 1–21, 1998.

[81] B. A. Conway, "A survey of methods available for the numerical optimization of continuous dynamic systems," *Journal of Optimization Theory and Applications*, vol. 52, pp. 271–306, 2 2012.

[82] A. Rao, "A survey of numerical methods for optimal control," *Advances in the Astronautical Sciences*, vol. 35, pp. 497–528, 2009.

[83] F. Topputo and C. Zhang. (2014). "Survey of direct transcription for low-thrust space trajectory optimization with applications," [Online]. Available: http://dx.doi.org/10.1155/2014/851720.

[84] I. Hwang, *AAE 568 Notes*. Purdue University, 2016.

[85] A. Bryson and Y. Ho, *Applied Optimal Control*. Blaisdell, Waltham, Mass, 1969.

[86] J. Bell, "Primer vector theory in the design of optimal transfers involving libration point orbits," Ph.D. Thesis, School of Aeronautics and Astronautics, Purdue University, 1995.

[87] P. Williams, "Hermite-legendre-gauss-lobatto direct transcription in trajectory optimization," *Journal of Guidance, Control, and Dynamics*, vol. 32, pp. 1392–1395, 4 2009.

[88] C. R. Hargraves and S. W. Paris, "Direct trajectory optimization using nonlinear programming and collocation," *Journal of Guidance, Control, and Dynamics*, vol. 10, pp. 338–342, 4 1987.

[89] G. Lantoine and R. P. Russell, "A hybrid differential dynamic programming algorithm for constrained optimal control problems. part 1: Theory," *Journal of Optimization Theory and Applications*, vol. 154, pp. 382–417, 2 2012.

[90] E. Pellegrini, "Multiple-shooting differential dynamic programming with applications to spacecraft trajectory optimization," Ph.D. Thesis, The University of Texas at Austin, 2017.

[91] J. D. Aziz, J. S. Parker, D. J. Scheeres, and J. A. Englander, "Low-thrust many-revolution trajectory optimization via differential dynamic programming and a sundman transformation," *Advances in the Astronautical Sciences*, vol. 160, pp. 520–548, 2017.

[92] J. D. Aziz, D. J. Scheeres, and G. Lantoine, "Hybrid differential dynamic programming in the circular restricted three-body problem," *Journal of Guidance, Control and Dynamics*, vol. 42, pp. 963–975, 5 2019.

[93] G. Whiffen. (2002). "Static/dynamic control for optimizing a useful objective," [Online]. Available: http://www.google.com/patents/US6496741.

[94] G. Whiffen. (2006). "Mystic: Implementation of the static dynamic optimal control algorithm for high-fidelity, low-thrust trajectory design," [Online]. Available: http://trs-new.jpl.nasa.gov/dspace/handle/2014/40782.

[95] G. J. Whiffen and J. Sims, "Application of a novel optimal control algorithm to low-thrust trajectory optimization," *AAS/AIAA Space Flight Mechan- ics Meeting*, 2003.

[96] R. S. Sutton and A. G. Barto, *Reinforcement Learning: An Introduction*. MIT Press, Massachusetts, USA, second edition, 2018.

[97] J. Stuart, M. Ozimek, and K. C. Howell, "Optimal, low-thrust, path-constrained transfers between libration point orbits using invariant manifolds," *AIAA/AAS Astrodynamics Specialist Conference*, 2010.

[98] D. C. Folta, N. Bosanac, A. Cox, and K. C. Howell, "The lunar icecube mission design: Construction of feasible transfer trajectories with a constrained departure," *AAS/AIAA Space Flight Mechanics Meeting*, 2016.

[99] R. E. Pritchett, E. Zimovan, and K. C. Howell, "Impulsiveandlow-thrusttransferdesignbetween stable and nearly stable periodic orbits in the restricted problem," *18th AIAA SciTech Forum, Kissimmee, Florida, January*, 2018.

[100] B. P. Pino, K. C. Howell, and D. C. Folta, “An energy-informed adaptive algorithm for low-thrust spacecraft cislunar trajectory design,” *AAS/AIAA Astrodynamics Specialist Conference*, 2020.

[101] J. Williams, D. E. Lee, R. J. Whitley, K. A. Bokelmann, D. C. Davis, and C. F. Berry, “Targeting cislunar near rectilinear halo orbits for human space exploration,” *AAS/AIAA Spaceflight Mechanics Meeting*, 2017.

[102] M. T. Ozimek, “A low-thrust transfer strategy to earth-moon collinear libration point orbits,” M.S. Thesis, School of Aeronautics and Astronautics, Purdue University, 2006.

[103] M. Vaquero and J. Senent, “Poincaré: A multi-body, multi-system trajectory design tool,” *7th International Conference on Astrodynamics Tools and Techniques*, 2018.

[104] G. Lantoine, “Efficient nrho to dro transfers in cislunar space,” *AAS/AIAA Astrodynamics Specialist Conference*, 2017.

[105] R. Pritchett, “Strategies for low-thrust transfer design based on direct collocation techniques,” Ph.D. Thesis, School of Aeronautics and Astronautics, Purdue University, 2020.

[106] E. S. Gadelmawla, M. M. Koura, T. M. A. Maksoud, I. M. Elewa, and H. H. Soliman, “Roughness parameters,” *Journal of Materials Processing Technology*, vol. 123, pp. 133–145, 2002.

[107] B. P. Pino, K. C. Howell, D. C. Folta, and R. E. Pritchett, “Extended mission options for the lunar icecube low-thrust spacecraft by leveraging the dynamical environment,” *71st International Astronautical Congress*, 2020.

VITA

Bonnie Prado Pino received her Bachelor of Sciences in Electronics Engineering from the Pontificia Universidad Javeriana in Bogotá, Colombia. After working as a visitor scholar for the Department of Aerospace Engineering and Engineering Mechanics at The University of Texas at Austin, Bonnie started her graduate studies, and was awarded her Master of Sciences in Aerospace Engineering from the University of Texas at Austin in Austin, Texas. Bonnie is currently a PhD candidate in Astrodynamics and Space Applications at the School of Aeronautics and Astronautics at Purdue University in West Lafayette, Indiana. Her current research focuses on the trajectory design of vehicles in the Earth-Moon system, mainly exploring control strategies for low-thrust spacecraft's trajectory optimization in multi-body regimes.

Some of Bonnie's awards and recognition include the Zonta International Amelia Earhart Fellowship, the Dr. Luther S. Williams Leadership Award, the African-Colombian of the Year, and the Colciencias fellowship. Colciencias is the Colombian Administrative Department of Science, Technology and Innovation. Besides being a member of multiple student and professional organizations, including the National Society of Black Engineers, and the Society of Hispanic Professional Engineers, in which she has held various leadership positions, Bonnie is the founder of the Afro-Latino Experience Organization, ALE, a non-for-profit initiative that seeks to expose underrepresented students from disadvantaged regions in Latin America, to science, technology, engineering and mathematics.

Bonnie's professional experiences include Teaching Assistant for various Aerospace Engineering undergraduate courses, Graduate Research Assistant for the Guidance, Navigation Controls Group at The University of Texas at Austin, and for the Multi-Body Trajectory Design Group at Purdue University. Summer internships at Cummins Inc. in Columbus, Indiana, as a Controls Engineer, and Mechatronics Engineer; Trajectory Design Engineer intern at Emergent Space Technologies Inc. in Greenbelt, Maryland; and Flight Dynamics Intern for Planet Labs Inc. in San Francisco, California.

Bonnie is a native of Quibdó, Chocó, Colombia.